

MODELING THE GENERATION AND PROPAGATION OF DISPERSIVE WAVES IN
THE GIANT MAGNETOSPHERES THROUGH MASS LOADING AND TRANSPORT
USING HYBRID SIMULATION

By

Blake Stauffer, B.S.

A Dissertation Submitted in Partial Fulfillment of the Requirements

for the Degree of

Doctor of Philosophy

in

Space Physics

University of Alaska Fairbanks

May 2018

APPROVED:

Dr. Peter Delamere, Committee Chair

Dr. Antonius Otto, Committee Member

Dr. Hui Zhang, Committee Member

Dr. David Newman, Committee Member

Dr. Renate Wackerbauer, Chair

Department of Physics

Dr. Anupma Prakash, Interim Dean

College of Natural Science and Mathematics

Dr. Michael Castellini, *Dean of the Graduate School*

Abstract

The magnetodiscs of Jupiter and Saturn are characterized by turbulence in the magnetic field. Broadband spectra of precipitating electrons at Jupiter suggest that a process is underway whereby large scale perturbations undergo a turbulent cascade in the magnetodisc. The cascade couples large perturbations to dispersive scales (kinetic and inertial Alfvén waves). Plasma transport in the rapidly rotating giant magnetospheres is thought to involve a centrifugally-driven flux tube interchange instability, similar to the Rayleigh-Taylor (RT) instability. Mass loading from satellites such as Io and Enceladus also cause dispersive wave formation in the magnetosphere, which is a source for broadband aurora. This dissertation presents a set of hybrid (kinetic ion/fluid electron) plasma simulations of the RT instability and the Io flux tube using conditions appropriate for the magnetospheres of Jupiter and Saturn. Both the Io torus and the planetary magnetodisc act as resonant cavities for counter propagating waves, which creates turbulence. The transmission ratio of wave power from the Io torus is 53%, an improvement from previous models (20% transmission), which is important to the generation of the Io auroral footprint. The onset of the RT instability begins at the ion kinetic scale and cascades to larger wavelengths. Strong guide field reconnection is a mechanism for radial transport of plasma in the magnetodisc. Counter propagating waves within the RT instability is the origin of turbulence within the magnetodisc.

Table of Contents

	Page
Title Page	i
Abstract.....	iii
Table of Contents	v
List of Figures.....	vii
List of Appendices	xi
Acknowledgments	xiii
Introduction.....	1
1.1 Comparative Magnetospheres.....	1
1.2 Jupiter's Aurorae.....	4
1.3 Mass Transport in the Giant Magnetospheres.....	7
1.4 Turbulence in the Magnetodisc	10
1.5 Waves in the Io Plasma Torus.....	17
1.6 Small Scale Wave Investigation	24
1.7 Hybrid Code	27
Io Plasma Torus.....	33
2.1 Introduction.....	33
2.2 Hybrid Code Initialization.....	36
2.3 One Dimensional Model	41
2.4 Two Dimensional Model	48
2.5 2D Turbulent Wave Interaction.....	50
2.6 Conclusion	55
2D Rayleigh-Taylor Instability	61
3.1 Introduction.....	61
3.2 Hybrid Code Initialization.....	63
3.3 Growth Rates	70
3.4 Dispersion Analysis	75
3.5 Conclusion	77
3D Rayleigh-Taylor Instability	79
4.1 Introduction.....	79
4.2 Hybrid Code Initialization.....	82
4.3 Simulations with Seeded Wave Modes.....	90

4.4	Self-seeded Simulations.....	94
4.5	Conclusion	97
Conclusion		105
5.1	Power Transmission in the Io Plasma Torus	105
5.2	The Turbulent Cascade in the Magnetodisc.....	107
5.3	Radial Transport in the Magnetodisc.....	108
5.4	Future Studies	109
Appendices		113
References		143

List of Figures

	Page
Figure 1.1 Diagram of the terrestrial magnetosphere	2
Figure 1.2 Diagram of the Jovian magnetosphere.....	3
Figure 1.3 Corotation-convection models for Earth and Jupiter	5
Figure 1.4 Schematic of the Vasyliunas cycle	6
Figure 1.5 Ultraviolet auroral images of Jupiter	6
Figure 1.6 Electron energy spectrum at Jupiter	8
Figure 1.7 Mass transport and magnetic flux circulation	9
Figure 1.8 Magnetodisc in the Equatorial Plane	11
Figure 1.9 Cassini magnetometer data	11
Figure 1.10 Magnetic field perturbations.....	12
Figure 1.11 Turbulent heating of plasma around Saturn.....	13
Figure 1.12 Calculation of heating rate density.....	15
Figure 1.13 Kolmogorov turbulent cascade.....	17
Figure 1.14 Alfvén wave propagation in the Io flux tube	19
Figure 1.15 Energy-time spectrograms	20
Figure 1.16 Interaction of the Jovian magnetosphere with Io	22
Figure 1.17 Background parameters for the gyrofluid model.....	23
Figure 1.18 Spectra of the waves observed by Galileo	25
Figure 1.19 Resonant cavity inside of the magnetodisc.	27
Figure 1.20 Resolved vs. unresolved ion motion.....	30
Figure 1.21 Test wave modes launched in the hybrid simulation	32
Figure 2.1 MHD model for the propagation of dispersive Alfvén waves	34
Figure 2.2 1D mapping of the time evolution of the magnetic field.....	35
Figure 2.3 Convection of a cloud of plasma.....	37

Figure 2.4	1D density profile of the Io plasma torus	39
Figure 2.5	Waves transmitted through the Io plasma torus	42
Figure 2.6	Alfvén wave just after exiting the torus.....	43
Figure 2.7	Ion velocity distribution with time	45
Figure 2.8	Ion cyclotron waves	46
Figure 2.9	Frequency range of wave power	46
Figure 2.10	Kinetic Alfvén wave dispersion.....	47
Figure 2.11	Alfvén wave power transmission	49
Figure 2.12	2D Alfvén wave propagation.....	51
Figure 2.13	Eggbox velocity perturbation	53
Figure 2.14	Dispersion relations at the fluid and kinetic scale	54
Figure 2.15	Evidence of turbulence from the frequency analysis.....	55
Figure 2.16	Ion heating over time.....	56
Figure 2.17	Incompressible plasma flows around Io.....	57
Figure 3.1	Growth of the Rayleigh-Taylor instability	62
Figure 3.2	RT density change comparison: MHD vs. hybrid.....	62
Figure 3.3	Initial parameters for the 2D RT instability.....	66
Figure 3.4	Initialized pressure profile.....	68
Figure 3.5	Plasma- β profile of the 2D RT instability	69
Figure 3.6	Density profile of a self-seeding RT instability	70
Figure 3.7	Growth of a self-seeded RT instability.....	72
Figure 3.8	Growth of a seeded $m = 3$ RT instability.....	73
Figure 3.9	Growth rate of the RT instability.....	74
Figure 3.10	Comparison of growth rates based on wave number.....	75
Figure 3.11	Dispersion of specific wave modes	76
Figure 3.12	Wave mode coalescence	77
Figure 4.1	Illustration of Jupiter magnetosphere-ionosphere coupling.....	80

Figure 4.2	Global MHD simulation of Saturn's inner magnetosphere	81
Figure 4.3	MHD RT instability.....	82
Figure 4.4	Specific and flux tube entropy at Saturn.....	83
Figure 4.5	3D RT simulated domain with fixed field lines.....	83
Figure 4.6	Plasma- β profile of the 3D RT instability	86
Figure 4.7	Pressure evolution of the 3D RT Instability	87
Figure 4.8	Pressure comparison with temperature and density	88
Figure 4.9	3D RT simulated domain with periodicity along y	89
Figure 4.10	Plasma- β profile of the 3D RT instability with periodicity along y	90
Figure 4.11	Formation of the $m = 3$ wave mode in 3D	92
Figure 4.12	3D RT growth rate comparison	93
Figure 4.13	Growth of the RT instability in 3D	95
Figure 4.14	Phase alignment in the RT instability	96
Figure 4.15	Wave power coalescence in density over time	98
Figure 4.16	Regions of parallel electric field	99
Figure 4.17	RT 3D magnetic field profile.....	100
Figure 4.18	Fourier analysis of the perpendicular and parallel wave modes.....	102
Figure 4.19	Change in mixing ratio over time	103
Figure 5.1	Plasma transport at a viscous boundary	111
Figure A.1	Diagram of a Rayleigh-Taylor instability.....	113
Figure C.1	The time stepping algorithm	126
Figure C.2	The coordinate dual cell	129
Figure C.3	Particle-in-cell weighting.....	129

List of Appendices

	Page
Appendix A: Derivation of the Growth Rate of the Rayleigh-Taylor Instability	113
Appendix B: Derivation of the Dispersion Relationship for Alfvén Waves	119
Appendix C: Hybrid Code Algorithms	125
Appendix D: Updates to the Hybrid Code	131

Acknowledgments

I would like to give a very special thanks to my advisor Dr. Peter Delamere who helped me most with my learning and research. I am extremely grateful for his hand in teaching me advanced plasma physics topics both inside and outside the classroom. His knowledge and example provided the base for this thesis. I am also appreciative of his efforts to secure funding for our research for the last five years, as well as his encouragement and advice.

Another acknowledgment should go to the Research Computing Systems facility in the Geophysical Institute, as well as its predecessor, the Arctic Research Computing Systems, for providing the compute nodes necessary to run many of the large scale hybrid simulations. The PACMAN and CHINOOK clusters were indispensable while conducting this research. Thanks to all the staff who keep the supercomputer running.

I have a special thanks for the residents of Alaska and other large tax contributors who subsidize the costs of education and research at the University of Alaska through the mechanism of the State.

Introduction

1.1 Comparative Magnetospheres

All bodies in the solar system are subject to interaction with the solar wind. For planetary bodies that possess an intrinsic dipolar magnetic field, interaction with the solar wind results in the formation of a cavity surrounding the body, known as the magnetosphere. The planetary magnetic field acts as an obstacle to the flow for the solar wind, which is diverted around the magnetosphere. Figure 1.1 illustrates some of the main features of the terrestrial magnetosphere. Processes in the planetary interior generate a magnetic field that resembles a dipole. Plasma and the interplanetary magnetic field (IMF) in the solar wind is deflected by the planetary magnetic field. The boundary separating the solar wind from the magnetosphere is called the magnetopause. Solar wind flows are super-Alfvénic and super-sonic, which combined comprise the fast Alfvén mode. This means that the convection velocity of the solar wind relative to the magnetosphere is larger than the Alfvén speed (this is analogous to the sound speed, the maximum group velocity of waves in a plasma medium). The encounter of the solar wind plasma with a blunt obstacle, the magnetosphere, results in the formation of the bow shock, where the solar wind plasma is slowed to sub-sonic velocity and diverted around magnetosphere. Momentum transfer from solar wind to the magnetosphere stretches the midnight sector of the magnetosphere into a tail. The dynamics of the terrestrial magnetosphere is modeled using the Dungey cycle [Dungey, 1961]. Magnetic reconnection at the dayside magnetopause is the dominant process that couples the solar wind momentum to the magnetosphere and ionosphere. Thus the polar regions are open to the solar wind. The cycle also drives convection in the ionosphere, and is modeled ideally as a large scale two cell process. Finally, the cycle is closed with magnetic reconnection in the night side tail region. Shear flow-driven instabilities at the magnetopause are important drivers of mass transport in the magnetosphere [Lee *et al.*, 1981; Huba, 1996; Otto and Fairfield, 2000; Nykyri and Otto, 2001, 2004], allowing solar wind plasma into the terrestrial

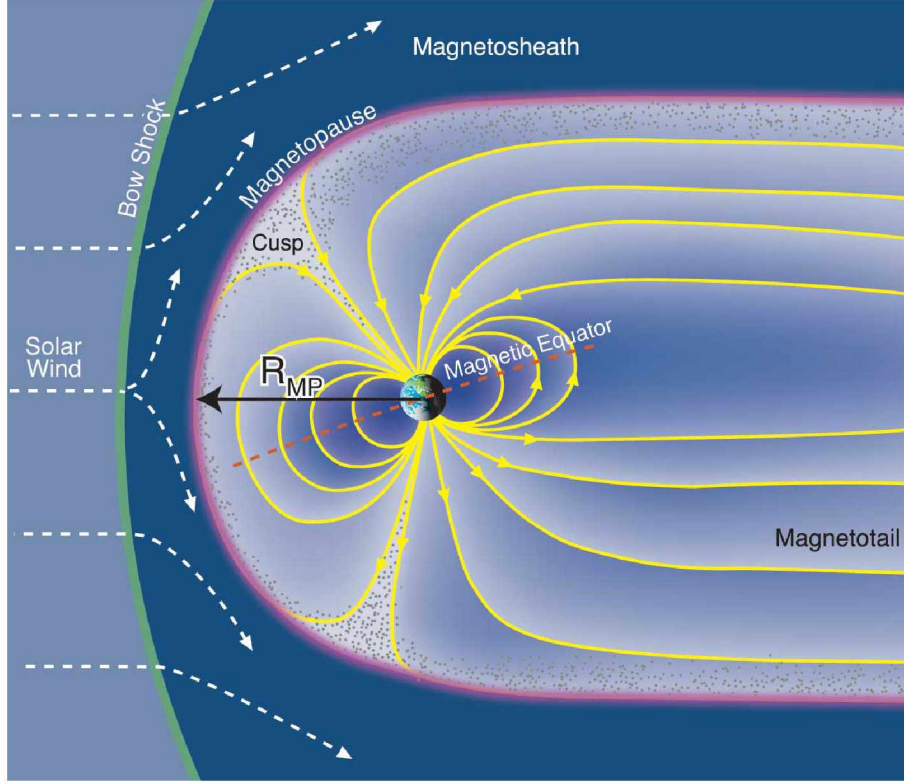


Figure 1.1: Diagram of the terrestrial magnetosphere. The magnetosphere is a cavity formed as a result of the solar wind interaction with the terrestrial magnetic field. The boundary between the magnetic fields of the solar wind and the earth is the magnetopause. Incoming solar wind is subject to a shock, known as the bow shock, as the super-Alfvénic flow transitions to a sub-Alfvénic flow and is diverted around the magnetosphere. Momentum transfer from the solar wind to the magnetosphere elongates the midnight sector into a structure called the magnetotail. Magnetospheric dynamics are driven primarily by the solar wind, as it is the main source of plasma for the magnetosphere [Bagenal and Bartlett, 2015].

magnetosphere.

Most magnetospheres, particularly those of Earth and the inner planets, are primarily driven by interactions with the solar wind. The outer planets, namely Jupiter and Saturn, are primarily driven by mechanics in the inner magnetosphere. This is due to their internal source of plasma from active satellites. The giant planet magnetospheres are mostly dominated by rapid planetary rotation. Plasma that originates from the deep interior of the magnetosphere, Io and Enceladus, is centrifugally confined. However, the centrifugal force from the rapid rotation pushes the plasma into a thin structure called the magnetodisc. The magnetic field that is frozen-in to the plasma is pushed outward, greatly inflating the size of the

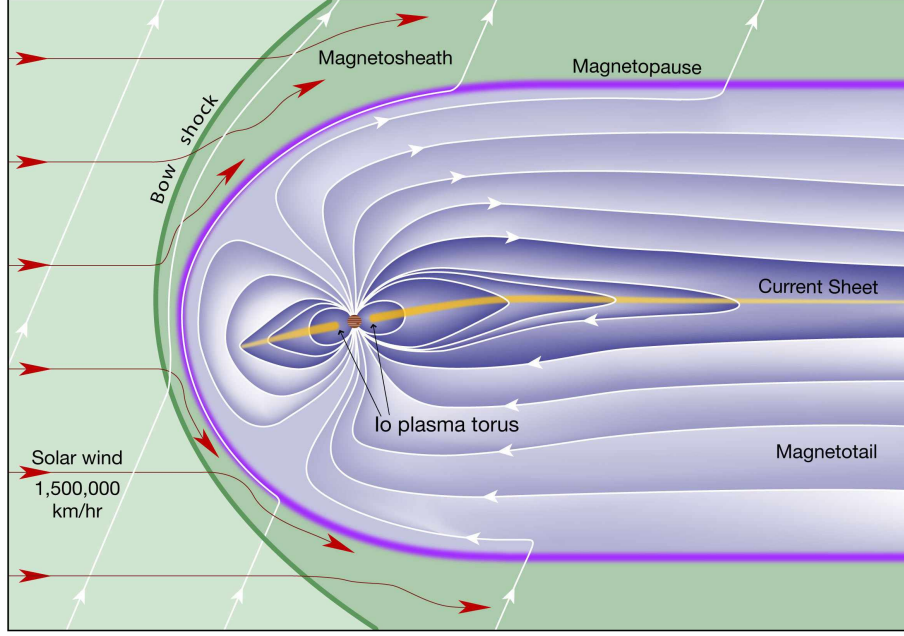


Figure 1.2: Diagram of the Jovian magnetosphere. It has similar features to the terrestrial magnetosphere, such as a magnetopause and magnetotail. A major difference is Jupiter’s internal source of plasma as a result of its active satellites deep in the magnetosphere. Jupiter’s rapid rotation acts as a centrifugal force which inflates the magnetosphere. The thin dense plasma structure is called the magnetodisc [Bagenal and Bartlett, 2015].

magnetospheres (See Figure 1.2). The giant magnetospheres have a very large range in standoff distance due to variations in the solar wind. Tangential stresses from the viscous interaction in the solar wind helps drive the transport of plasma from the magnetodisc [Axford and Hines, 1961; Delamere and Bagenal, 2010].

If we assume that an Earth-like Dungey cycle is also operating at the giant magnetospheres, magnetic reconnection must not only accomplish convection in the ionosphere, but also transfer sufficient momentum facilitate sunward convection in the magnetodisc. Brice and Ioannidis [1970] use the standard corotation-convection model to illustrate the differences in magnetospheric flows at both Earth and Jupiter (Figure 1.3). The total potential in the sun-planet rest frame is

$$\phi = \frac{\Omega B_0 R_P^2}{\rho} + \nu v_{sw} B_{sw} R_P y \quad (1.1)$$

where Ω is the planet’s angular velocity, B_0 is the planet’s surface field strength at the equator, ρ and y are the respective radial and dawn-dusk distances in units of planetary radius (R_P), v_{sw} and B_{sw} are solar wind parameters, and ν is the reconnection potential associated with the Dungey cycle. When we compare these potentials for both Earth and Jupiter, we find that the boundary of the plasmasphere at Earth lies within the magnetopause, while Jupiter’s magnetodisc lies at the magnetopause. Therefore internally generated plasma is a significant factor in radial transport at Jupiter, and we need a better model than Dungey cycle reconnection at the giant magnetospheres. *Vasyliunas* [1983] introduces a model for radial transport based on reconnection and centrifugal stresses. Rapid rotation compresses the magnetodisc and thins it in the magnetotail until reconnection occurs and plasma blobs are ejected into the tail. The location of these reconnection events comprise the X line. If dayside reconnection does occur at Jupiter as well, then the closing reconnection occurs on the dawn/tail flank and corotational flow returns magnetic flux back to the dayside [*Cowley et al.*, 2005] (See Figure 1.4). The influence of magnetic reconnection on plasma transport is still being debated. *Mozer and Hull* [2010] argued that energy transfer from reconnection is too small to have influence on magnetospheric transport, while *Delamere and Bagenal* [2010] argued that viscous shear flows at the magnetopause are important mechanisms for momentum and energy transport, necessitating reconnection at some scale [*Burkholder et al.*, 2017].

1.2 Jupiter’s Aurorae

Juno observations of Jupiter reveal that the brightest aurora at 400 kV is broadband, indicating a large range in precipitating electron energies that map back to the middle magnetosphere [*Mauk et al.*, 2017]. UV spectra of the aurora indicates complicated structure present near the poles (See Figure 1.5). The large range in frequencies are indicative of a turbulent cascade in electron energies whose acceleration processes originate in the middle magnetosphere. The more diffuse aurora poleward of the broadband arcs maps to the outer

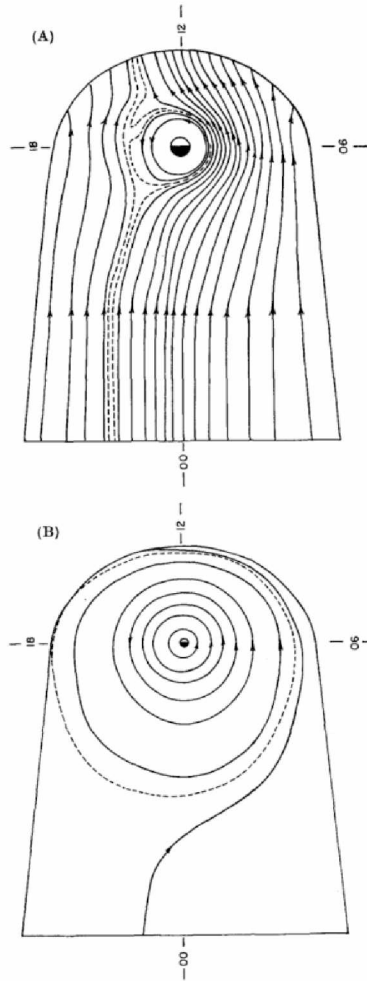


Figure 1.3: Corotation-convection models for Earth and Jupiter. It assumes sunward convection in the tail [Brice and Ioannidis, 1970]. The plasmopause boundary lies inside of the magnetopause boundary for Earth and at the magnetopause boundary for Jupiter.

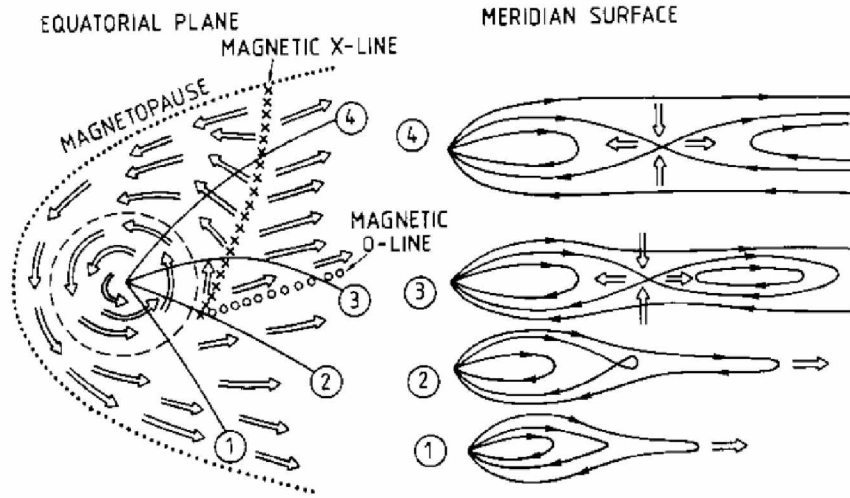


Figure 1.4: Schematic of the Vasyliunas cycle [Vasyliunas, 1983], showing the local time variation of the detachment of plasmoids. Reconnection happens at the magnetic X line.

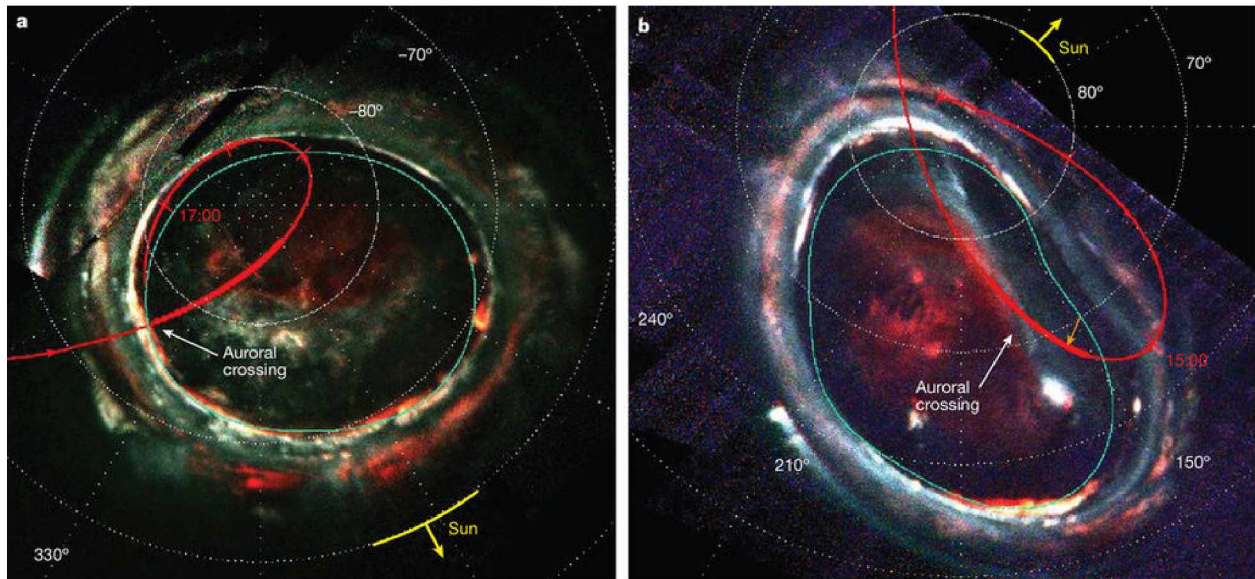


Figure 1.5: Ultraviolet auroras images of Jupiter from the Juno UVS instrument. The images contain intensities from three spectral ranges, false-colored red, green, and blue, providing qualitative information on precipitating electron energies (high, medium and low, respectively). Spacecraft trajectory relative to the magnetic field is shown in red [Mauk *et al.*, 2017]. Here we see structure in the auroral features at each of the poles. The bright emission in Figure b near 210° is a result of satellite interactions in the inner magnetosphere. The ring arcs map to the middle magnetodisc. The source of the more diffuse emission towards the center is debatable, as it is unknown if it is a result of solar wind interaction with magnetosphere, or of internal processes.

magnetosphere, and it is unknown whether solar wind interactions or other internal processes are responsible for the structures observed. Finally, the auroral spot and tail observed near 210° on the right figure is the Io auroral footprint. Observations of the footprint show broadband emission in the light spectrum, indicating that turbulence is also a factor in propagation of waves from Io to the ionosphere [Hess *et al.*, 2010].

Non-adiabatic heating of the plasma is also observed in-situ in the electron energy spectrogram [Saur *et al.*, 2004]. Inverted-V spectra indicates coupling to the ionosphere, similar to auroral features found at Earth. At Jupiter however, the electron spectra is more broadband than discrete, *indicating that auroral processes at Jupiter are substantially different from those at Earth* Mauk *et al.* [2017]. Figure 1.6 shows the electron energy spectrum from the JEDI instrument on Juno during its first perijove encounter. The majority of the electrons have low pitch angles, meaning that electron currents are field-aligned.

1.3 Mass Transport in the Giant Magnetospheres

Transport of the magnetodisc plasma cannot be considered independent of the planetary magnetic field. About 500 kg s^{-1} (Jupiter) and 50 kg kg s^{-1} (Saturn) of mass are lost to the solar wind [Delamere and Bagenal, 2013], but all magnetic flux, that was transported as a result of this, must be returned to the inner magnetosphere over the long term. Figure 1.7 shows the magnetic and mass flux as a function of radial distance at Saturn. The magnetic field data from Cassini suggests that there is net mass loss in the middle magnetodisc, but there is no net change in magnetic flux levels. Several observations have been made regarding flux transport to the magnetotail with magnetic reconnection used as evidence to support the Vasyliunas cycle [Russell *et al.*, 1999; Vogt *et al.*, 2010; Hill *et al.*, 2008; Jackman *et al.*, 2011]. However, the inferred rate of plasma loss from Jupiter’s tail is insufficient to account for all the mass that that must be lost from the magnetosphere, and that small scale processes leading to “drizzle” may be the primary loss mechanism [Bagenal, 2007]. Kivelson and Southwood [2005] proposed an alternative to the Vasyliunas cycle by showing

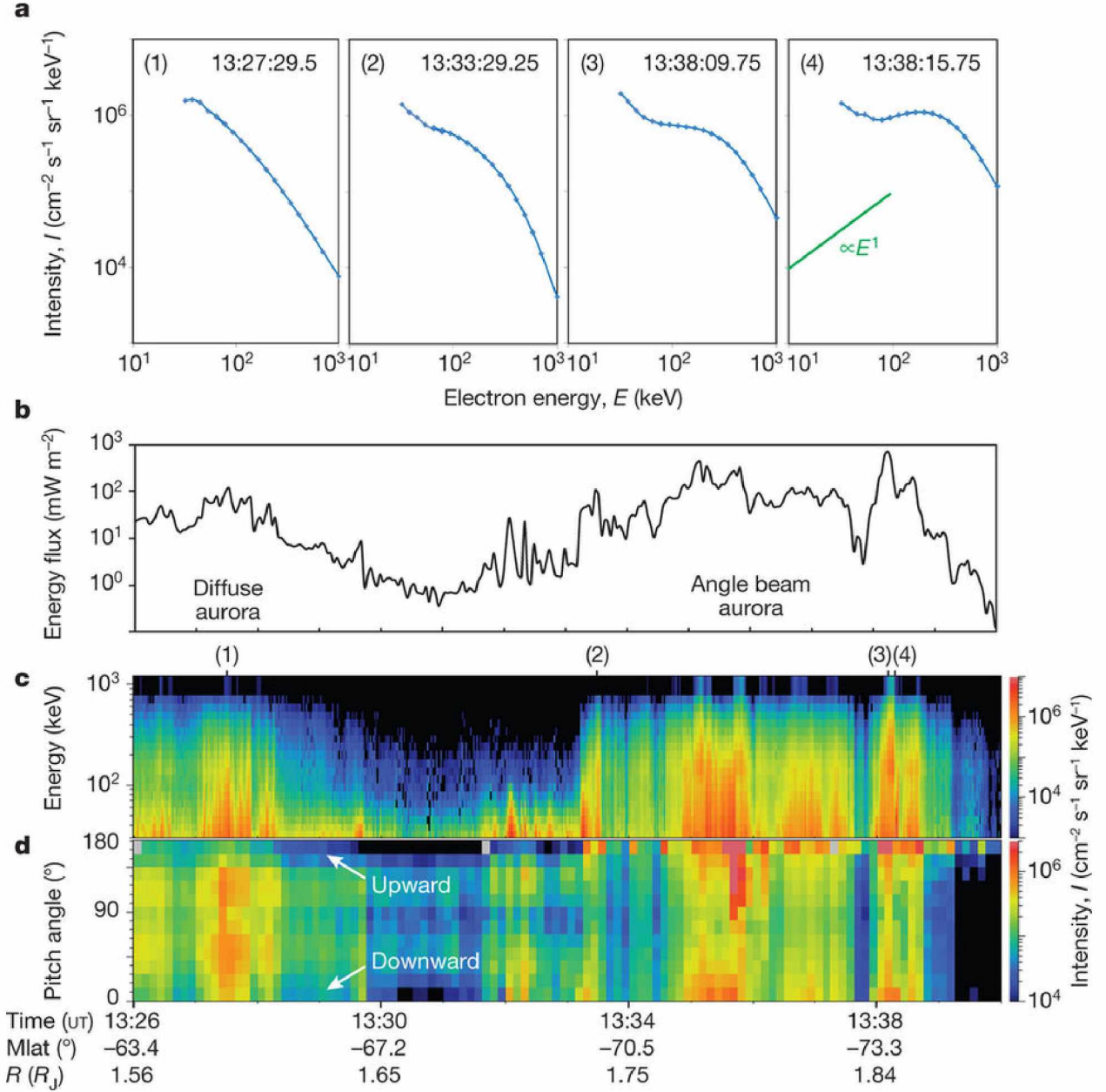


Figure 1.6: Energetic electron data at Jupiter from JEDI during Juno's first perijove encounter. **a)** Downward intensity I versus electron energy E spectra. **b)** Integrated downward electron energy flux. **c)** Intensity versus energy distributions for electrons within 20° of the downward magnetic field direction. **d)** Pitch angle distributions of intensities averaged over electron energy [Mauk *et al.*, 2017]. The downward energy flux from discrete acceleration is less at Jupiter than that caused by broadband or stochastic processes.

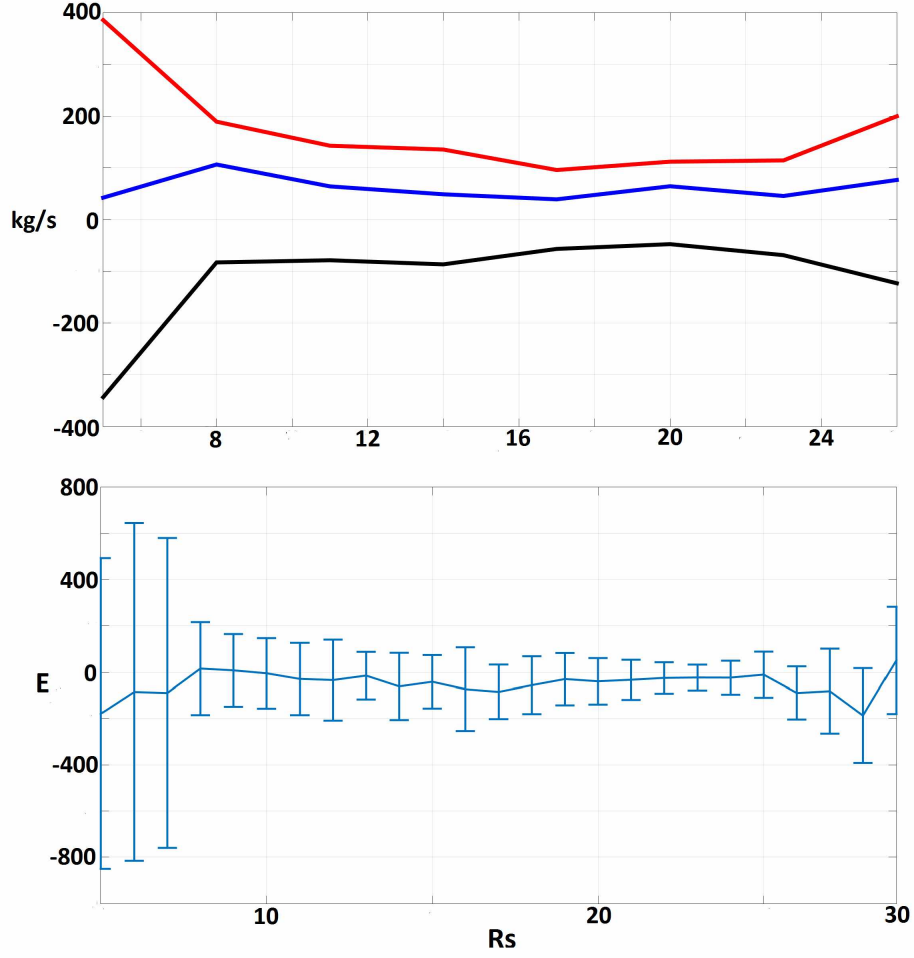


Figure 1.7: Mass transport and magnetic flux circulation rate at Saturn as a function of radial distance. The net flux transport is near zero, while there is a net loss of plasma mass of about 50 kg s^{-1} [Neupane *et al.*, 2017].

that temperature anisotropy ($T_{\parallel} > T_{\perp}$) would balloon the magnetodisc and cause it to become unstable.

At both Jupiter and Saturn, rapid planetary rotation puts the plasma in the magnetodisc in a non-inertial reference frame. In the reference frame of the plasma, there is a centrifugal force, or effective gravity, directed radially outward which induces transport. Radial transport through flux tube interchange can be accomplished in a few ways. One way is through interchange that is closed at high latitude through ion-neutral collisions in the ionosphere. As second is a ballooning instability in the outer magnetodisc where the field bulges out and stretches to form a thin current sheet. Magnetic reconnection then releases a plasmoid

that is ejected down the tail [Kivelson and Southwood, 2005]. The third way is through the interchange of partial flux tubes in the magnetodisc. These interchanges are closed by double reconnection at mid latitude [Ma *et al.*, 2016]. We will only be focusing on the last type of instability in this dissertation.

The density gradient in the magnetodisc is similar to the gravitationally driven Rayleigh-Taylor (RT) instability. Rapidly rotating cold, dense plasma is pushed radially outward, dragging magnetic flux with it. Conversely, hot, tenuous plasma is transported inward to conserve magnetic flux, and reduce the potential energy of the system [Delamere *et al.*, 2003, 2015]. Flux tubes with cold, dense plasma move radially outward, while flux tubes containing hot rarefied plasma are transported inward to conserve magnetic flux. This results in “fingers” of dense plasma that are transported outward. Figure 1.8 illustrates the formation of the RT surface waves in the equatorial plane. Appendix A describes the RT instability in greater detail.

Cassini magnetometer data of the magnetodisc at $L = 15$ provides evidence of strong magnetic field disturbance in the dusk flank (See Figure 1.9). It is also accompanied by strong non-adiabatic heating. The disturbed region shows regular interval swings for all three components of the field. The spatial scale of the surface waves can be determined from the velocity ($\sim 100 \text{ km s}^{-1}$) of the plasma convecting past Cassini [Thomsen *et al.*, 2010] (See Figure 1.8). Voyager 2 also observed very strong perturbations in the magnetic field at Jupiter every time it crossed the equatorial region (See Figure 1.10). A turbulent spectrum of waves are present in the magnetodiscs of both Jupiter and Saturn, and are related to the generation of broadband aurorae.

1.4 Turbulence in the Magnetodisc

As the plasma is radially transported, it is non-adiabatically heated, requiring an input energy of 3-16 TW at Jupiter and 75-630 GW at Saturn [Bagenal and Delamere, 2011]. At Saturn, Kaminker *et al.* [2017]; von Papen *et al.* [2014]; von Papen and Saur [2016] discuss a

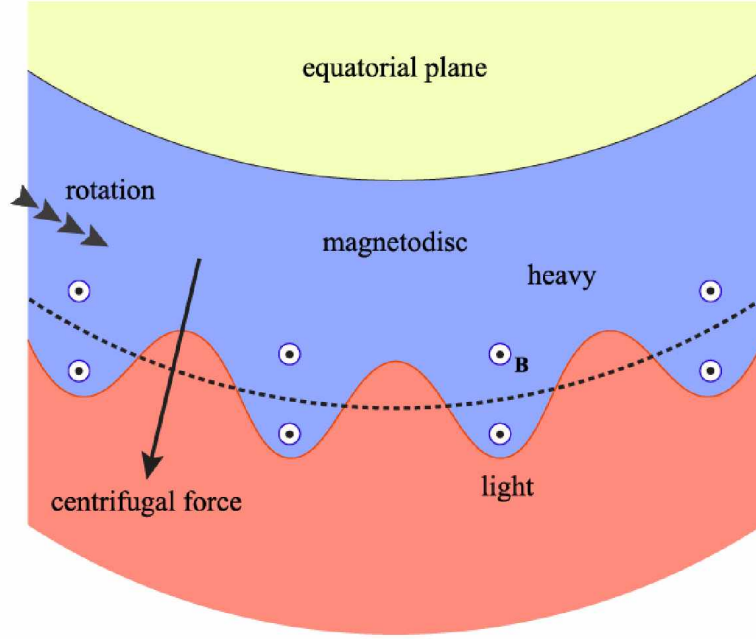


Figure 1.8: Magnetodisc in the equatorial plane. The density gradient of the magnetodisc along the radial direction sets up an unstable condition in the magnetodisc that results in surface waves that develop into RT instabilities. The effective gravity is supplied by centrifugal force from the magnetosphere's rapid rotation.

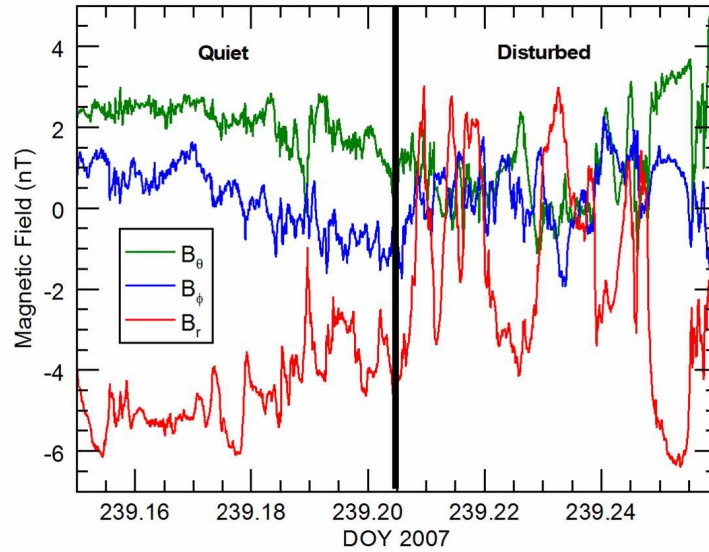


Figure 1.9: Cassini magnetometer data shows quiet and disturbed (e.g., many current sheet crossings) intervals over time (shown in Days of the terrestrial year 2007). There are wild swings in the magnetic field that could correspond to a characteristic length of the instabilities. At $L = 15$, $\lambda_i \sim 5000\text{km}$, and the plasma flow is 100 km s^{-1} , so separation of the peaks is $\sim 12\lambda_i$.

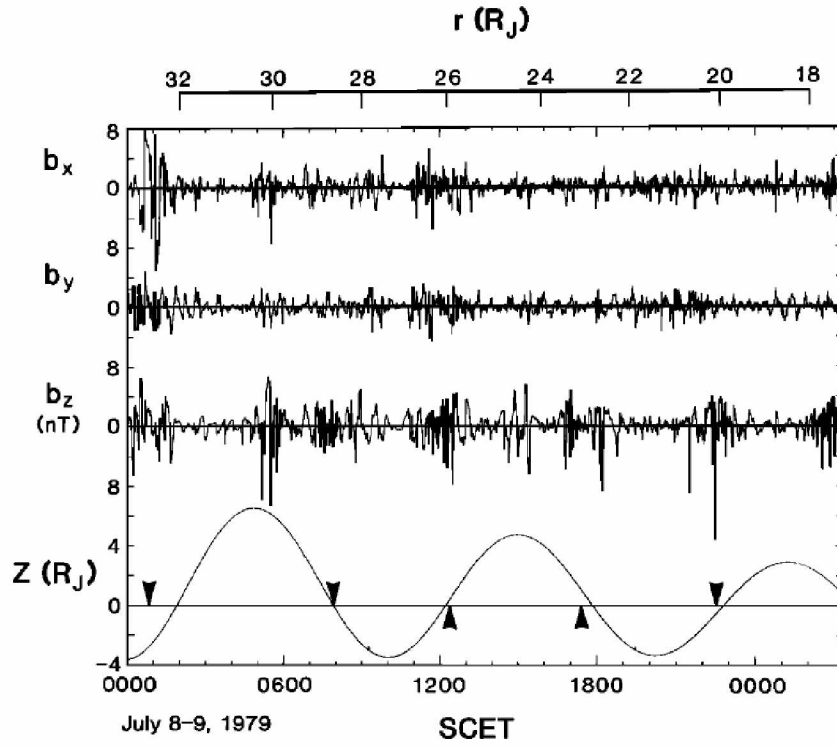


Figure 1.10: Magnetic field perturbations observed by Voyager 2. The bottom panel shows the instantaneous distance of Voyager 2 from the magnetic equator. The solid triangles denote the locations of the observed magnetic equator crossings. The large perturbations in the magnetic field at these locations indicate strong wave activity in the magnetodisc [Khurana and Kivelson, 1989].

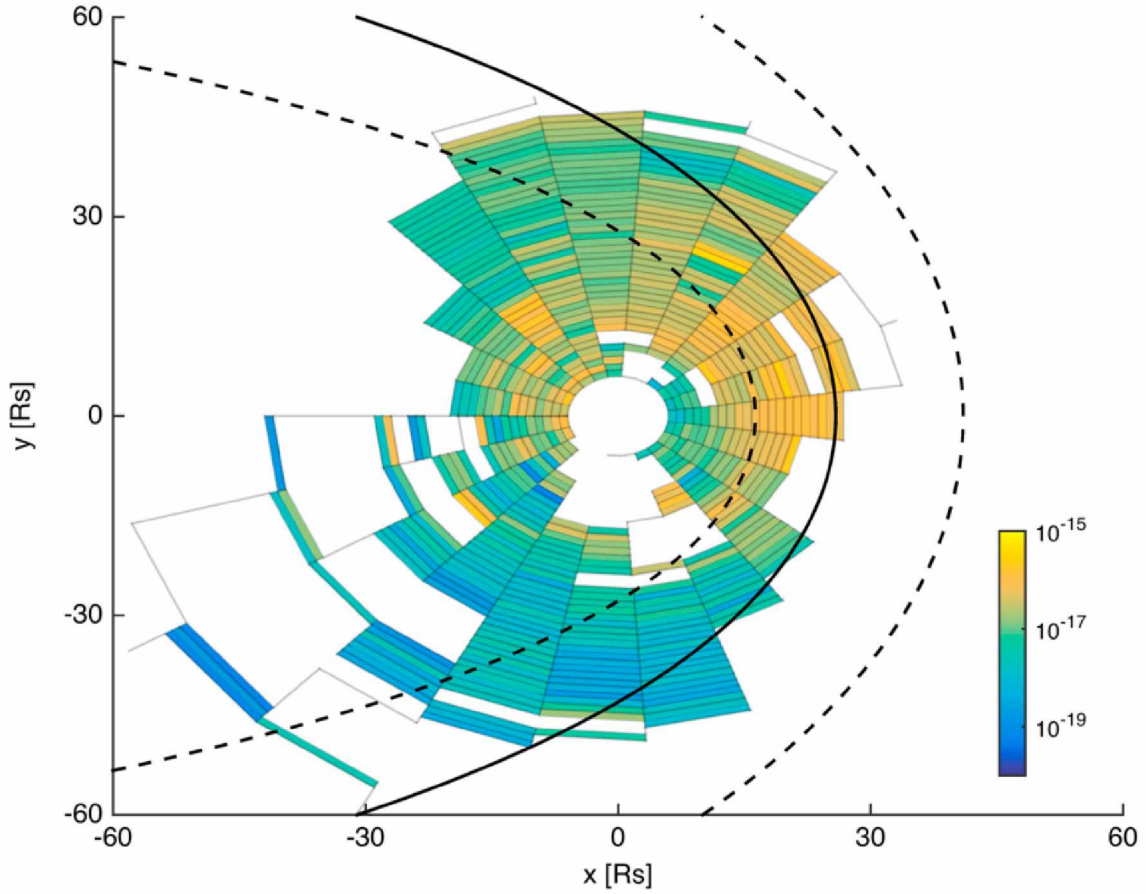


Figure 1.11: Turbulent heating of plasma around Saturn. This polar map of heating rate density indicates a local time asymmetry of turbulent processes, with an active region on the dayside to dusk sector and a quiet region in the post midnight sector. The color map is in units of W m^{-3} . Figure from *Kaminker et al.* [2017].

model for the turbulent heating of plasma that is axially asymmetric. Cassini magnetometer data suggest that turbulent heating occurs near the dusk sector of the magnetodisc, while the post midnight sector is relatively quiet (See Figure 1.11). More than just internally driven transport is taking place, and is likely influenced by solar wind interactions at the magnetopause.

Moreover, Figure 1.12 shows the Kolmogorov turbulent cascade of power density in the magnetic field in the inertial range (shown in blue). A slight bump in power density occurs near the ion gyrofrequency, suggesting that there is a power buildup at ion kinetic scales

before the power is dissipated at the kinetic range (shown in red). Furthermore, heating rate density changes depending on whether the heating rate is modeled using magnetohydrodynamic (MHD) waves in the inertial subrange of the turbulent cascade, or using dispersive, kinetic Alfvén waves (KAW) in the dissipation range. KAWs provide a larger heating rate as a result of turbulence. A possible explanation for this observation is that energy is preferentially injected at ion kinetic scales, resulting in both inverse and forward cascades.

In the inertial range we can characterize the turbulence as a set of vortical flows or eddies of different sizes and scales embedded within each other. Each eddy with a given size (d) share a characteristic velocity $u(d)$. For the derivation of the Kolmogorov turbulent cascade, we make the assumption that there is a steady rate of energy transfer from larger scales to smaller scales, that a set of eddies with the same characteristic length d have the same total energy level, and that the rate of energy supply at d_{max} is the same as the dissipation of the energy at the inertial scale.

The first parameter is ϵ , energy per unit mass per unit time. The units of ϵ are then

$$\epsilon \rightarrow \frac{ML^2T^{-2}}{MT} = L^2T^{-3} \quad (1.2)$$

where L is a unit length, M is unit mass, and T is unit time. From the above assumptions, we can model u , the velocities of the turbulent eddies as only dependent on d and ϵ .

$$u(d) = C(\epsilon d)^{1/3} \rightarrow \left[\left(\frac{L^2}{T^3} \right) \left(\frac{L}{1} \right) \right]^{1/3} = \frac{L}{T} \quad (1.3)$$

C is a unitless constant, and the $1/3$ power comes from dimensional analysis. From this we see that higher velocities are associated with larger vortical flows and contain most of the kinetic energy of the system. Smaller eddies have smaller speeds, and have less energy, so they must continue to dissipate energy down to the dissipation range.

The energy spectrum for turbulent cascade is the distribution of kinetic energy per unit mass across the many length scales, described by a wavenumber k , where $k = \pi/d$. The unit

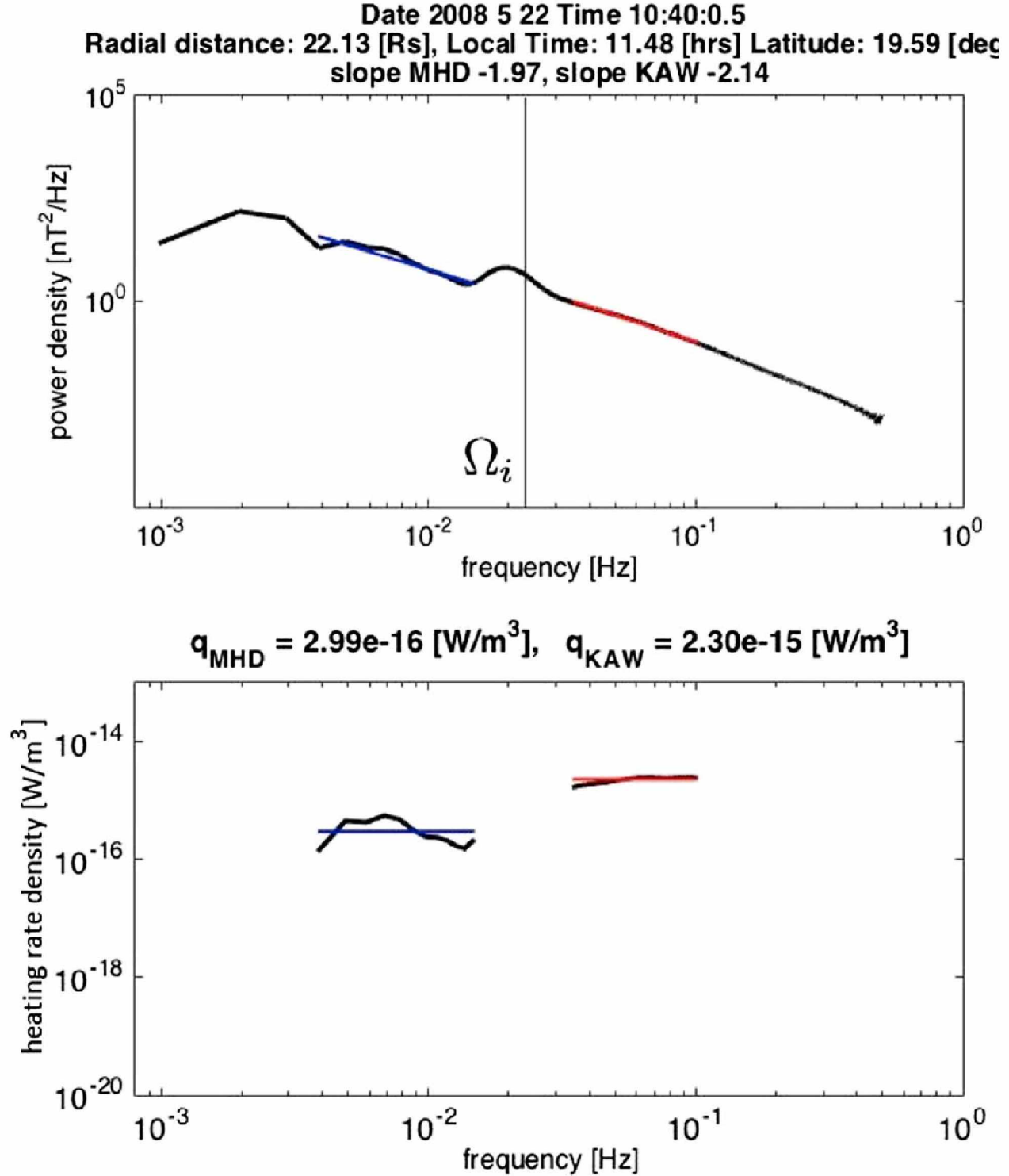


Figure 1.12: Calculation of heating rate density from the power spectrum using MHD and turbulence models. A strong MHD turbulence model is used to calculate the heating rate density in the inertial subrange of the power spectrum [3×10^{-3} Hz, $\frac{1}{1.5}\Omega_i$]. A strong kinetic Alfvén wave turbulence model is used to calculate the heating rate density in the kinetic dissipation subrange of the power spectrum [$1.5 \Omega_i$, 1×10^{-1} Hz]. Figure from *Kaminker et al.* [2017].

for k is then $1/L$. Kinetic energy per unit mass has dimensions

$$\frac{ML^2}{T^2M} = \frac{L^2}{T^2} \quad (1.4)$$

and has some distribution dependent on k :

$$dE = E_k(k)dk \quad (1.5)$$

$E_k(k)$ must then have units of L^3/T^2 . From our above assumptions, we can model E_k as a function of some powers of ϵ and k , multiplied by a dimensionless constant C_k :

$$E_k(k) = C_k \epsilon^\alpha k^\beta \quad (1.6)$$

Using dimensional analysis, we can solve for α and β .

$$\frac{L^3}{T^2} = \left(\frac{L^2}{T^3}\right)^\alpha \left(\frac{1}{L}\right)^\beta \quad (1.7)$$

$$3 = 2\alpha - \beta \quad (1.8)$$

$$2 = 3\alpha$$

$$\alpha = 2/3 \quad (1.9)$$

$$\beta = -5/3$$

From the system of equations, we discover a unique solution, and power law relationship for energy present as a function of k . In a plot of $\log E_k$ vs. k , the power -5/3 is manifest as a slope (See Figure 1.13). The slope is valid in a set of ranges, from the length scale where energy is supplied to the system, down to the length scale where viscous processes dissipate the energy. In a tenuous plasma, this occurs at the ion inertial length, λ_i . Energy from the waves is transferred to the ions and results in heating. As such, there is a change in the

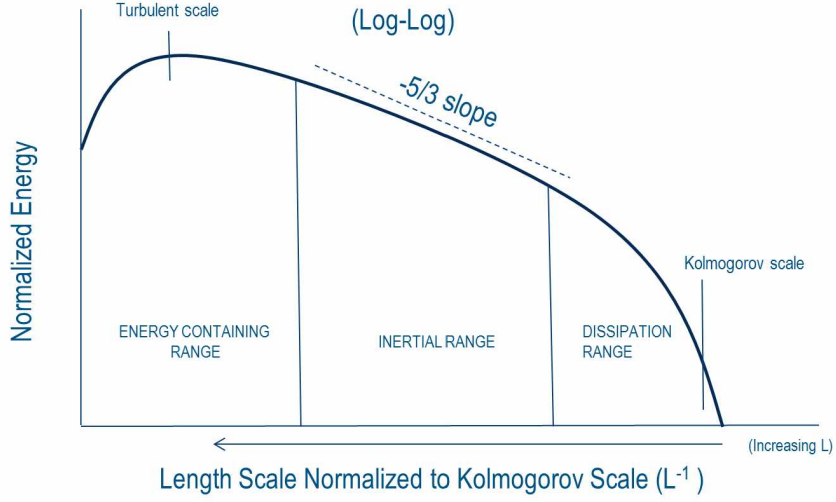


Figure 1.13: Kolmogorov turbulent cascade. Energy transfers from large scale vortices to smaller ones with a slope of $-5/3$, until the ion inertial scale is reached (marked as the dissipation range). From there, the energy is transferred to the ions in the form of heating. From Wyatt [2017].

slope of E_k at that wavelength. Any failure of the ions to dissipate the energy would lead to a buildup at the sub- λ_i scale, flattening out the curve. For turbulent processes in the magnetodisc and the Io flux tube, we expect to see the $-5/3$ power law relationship in the wave spectrum in the inertial subdomain.

1.5 Waves in the Io Plasma Torus

Figure 1.5 shows an intense spot of auroral activity from the inner magnetosphere that maps to Jupiter’s volcanically active moon Io, the main source of internal plasma. Auroral activity here is also relatively broadband, indicating that the formation of the Io footprint and following wake is due to Alfvénic disturbances [Hess et al., 2010; Mauk et al., 2017]. *The transmission of Alfvén waves between Jupiter and Io is an excellent case study because the power generated by the interaction can be reasonably estimated.* The power of the observed aurora can also be measured. We can then make an estimate of the wave power that has dissipated and focus on the mechanics of how this is done.

Mass loading at Io perturbs the surrounding magnetic field from corotational velocity (57

km s⁻¹). The motion of Io through the torus and surrounding plasma generates power, which is then transmitted along Jupiter’s field lines until it reaches the ionosphere. The estimated power input from this interaction is about 1×10^{12} W, with 5×10^{11} W transmitted to each hemisphere. However, only a few 10^{10} W of power is actually observed in intensity from Io’s auroral footprint in the visual IR, and radio wavelengths [Connerney *et al.*, 2001; Queinnec and Zarka, 1998; Hess *et al.*, 2010]. Wright [1987]; Delamere *et al.* [2003] estimate that $\sim 20\%$ of the 5×10^{11} W of wave power escapes the torus. The conversion efficiency between precipitating electrons and light in the aurora is only 10% [G  rard *et al.*, 2006]. This means that the rest of the wave energy must be transferred to the precipitating electrons to account for the power observed in the aurora, leaving no room for inefficiency in electron-wave coupling.

Figure 1.14 illustrates the Alfv  n current system in the flux tube. For the picked up plasma mass to be brought to full corotation, the current loop must close through the ionosphere to transfer momentum. At some point, however, there is “slippage” in the magnetic field before the Alfv  n wave reaches high latitude, preventing full corotation and generating a large enough parallel electric field to accelerate electrons. Electrons that escape through the loss cone of Jupiter’s magnetic mirror point precipitate and generate aurora (the leading auroral spot and secondary spots in the wake). The bent lines on the right figure result from the propagation delay of the Alfv  n waves while in the plasma torus. At the border of the torus, the wave is partially transmitted and partially reflected. Once the wave exits the torus its velocity increases to near lightspeed. The electron beams from the transmitted waves can again escape into the ionosphere to generate aurorae. Multiple reflections in the torus result in the secondary auroral spots [Bonfond *et al.*, 2008].

Evidence of superthermal electrons comes from Galileo’s plasma instrument [Frank and Paterson, 2000] as a result of ion pickup in the torus [Bagenal and Delamere, 2011] (See Figure 1.15). A continuous source of superthermal electrons is required because of losses from superthermal electron precipitation, or cooling due to interaction with thermal electrons in

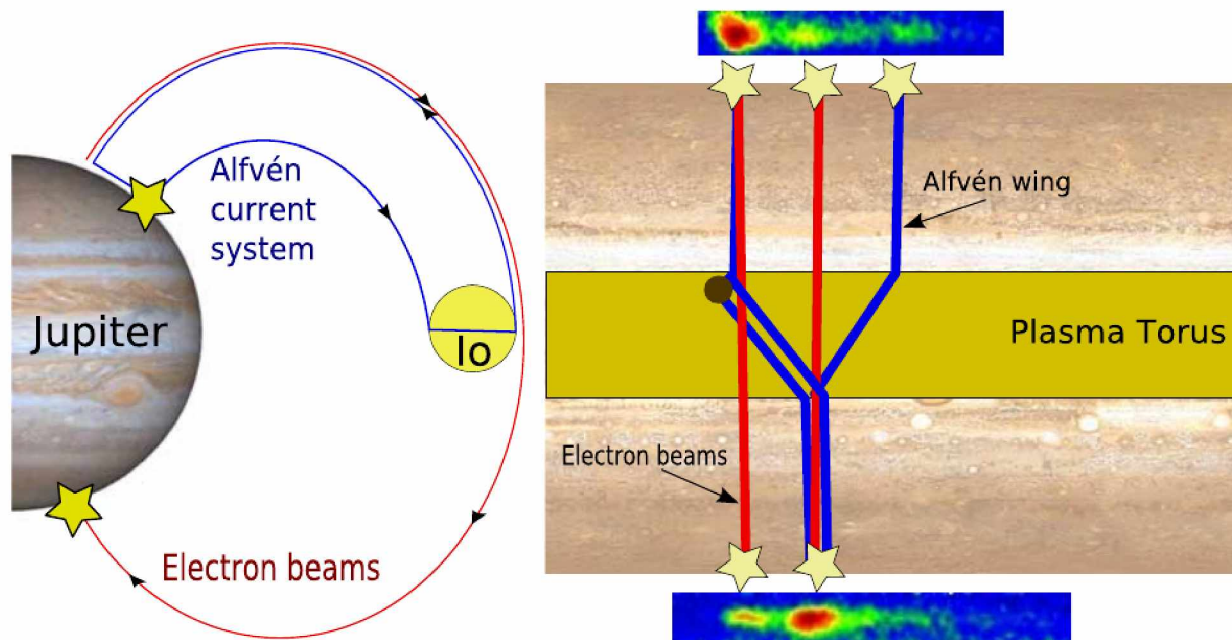


Figure 1.14: Diagram of the propagation of Alfvén waves from Io along Jupiter’s magnetic field lines [Bonfond *et al.*, 2008].

the torus. Injection of hot electrons is also present at various radial distances within the torus, and they tend to have the same energy spectrum as those generated at Io. Figure 1.15 shows the injection of hot electrons within the torus. An Io encounter occurs at ~ 1745 UT, with the same energy spectra of electrons in the torus.

In the torus itself, convecting plasma interacts with the neutral particles in Io’s atmosphere and loads neutral material into the magnetosphere at a rate of 1 ton s^{-1} , mostly sulfur and oxygen [Thomas *et al.*, 2004]. Charge exchange of a torus ion with a neutral molecule causes the new pickup ion to become influenced by the background magnetic field and start gyrating. Momentum is transferred from the magnetic field to the new ions as they are picked up into the flow. This bends the field and induces a perturbation in the magnetosphere that propagates as an Alfvén wave until it reaches the ionosphere [Neubauer, 1980; Saur *et al.*, 2004]. Bending of the field line creates a field-aligned current. The closing of the current across Io is opposite the motional electric field, so the $\mathbf{J} \cdot \mathbf{E} < 0$ becomes a source for waves (See Figure 1.16). The wave accelerates electrons along the dipole field lines

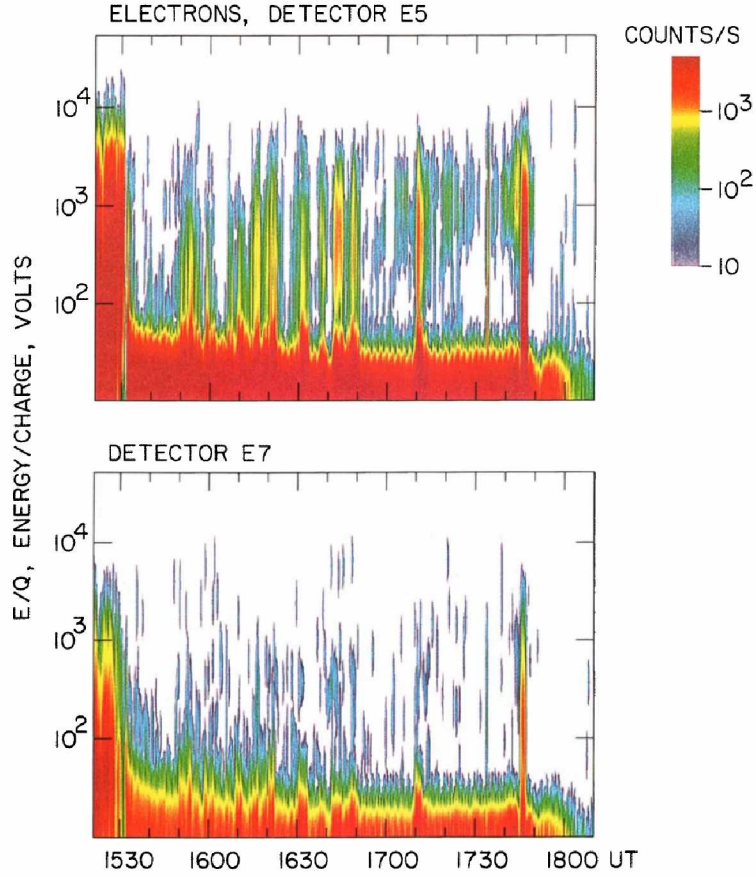


Figure 1.15: Energy-time spectrograms for the responses of two of the electron sensors of the plasma instrumentation on board the Galileo spacecraft during December 7, 1995 near the Io flux tube. The frequent spikes in electron energy are evidence of the superthermal electron injections in the torus [*Frank and Paterson, 2000*].

and generates aurora [Hess *et al.*, 2007]. In the plasma torus, high densities (modeled by Su *et al.* [2006], see Figure 1.17) and weaker magnetic fields decrease the propagation speed of the waves. Chust *et al.* [2005] showed that Io’s Alfvén wing is filamented, suggesting that there are waves forming at ion kinetic scales, possibly with broadband characteristics.

At these scales, Alfvén waves are dispersive and result in the formation of parallel electric fields, which can accelerate electrons. Within the torus, the kinetic Alfvén wave is relevant when k_{\perp} is near the ion thermal gyroradius (ρ_i). At higher latitude, filamentation of the wave reduces down to the scale of the electron skin depth, and electron inertia becomes important in the propagation of the wave (inertial Alfvén wave). The KAW is also dependent on electron temperature, and has the following dispersion relation:

$$\omega^2 = k_{\parallel}^2 v_A^2 \left[1 + k_{\perp}^2 \rho_i^2 \left(\frac{3}{4} + \frac{T_e}{T_i} \right) \right]. \quad (1.10)$$

The inertial Alfvén wave has the following dispersion relation, which only significantly modifies the non-dispersive Alfvén wave when $k_{\perp} \lambda_e \sim 1$:

$$\omega^2 = \frac{k_{\parallel}^2 v_A^2}{1 + k_{\perp}^2 \lambda_e^2}. \quad (1.11)$$

Derivations for these dispersive waves are in Appendix B. Figure 1.17 also shows k_{\perp} as a function of distance along the Io flux tube, starting from the ionosphere. Large k_{\perp} at high latitude indicates that electron inertia is significant. Near the torus, the ion thermal gyroradius contributes to the KAW.

Wave formation begins with mass loading of plasma as Io passes through the torus. A ring beam distribution of pickup ions and perturbation of the local magnetosphere by the satellite launch numerous kinds of plasma waves (e.g. shear Alfvén, ion cyclotron, whistler, and magnetosonic waves). They propagate to the edge of the torus where $\sim 20\text{-}25\%$ of the wave power is transmitted to high latitudes (where they generate aurorae if the electrons are accelerated into the loss cone of Jupiter’s magnetic mirror) [Wright, 1987; Delamere *et al.*,

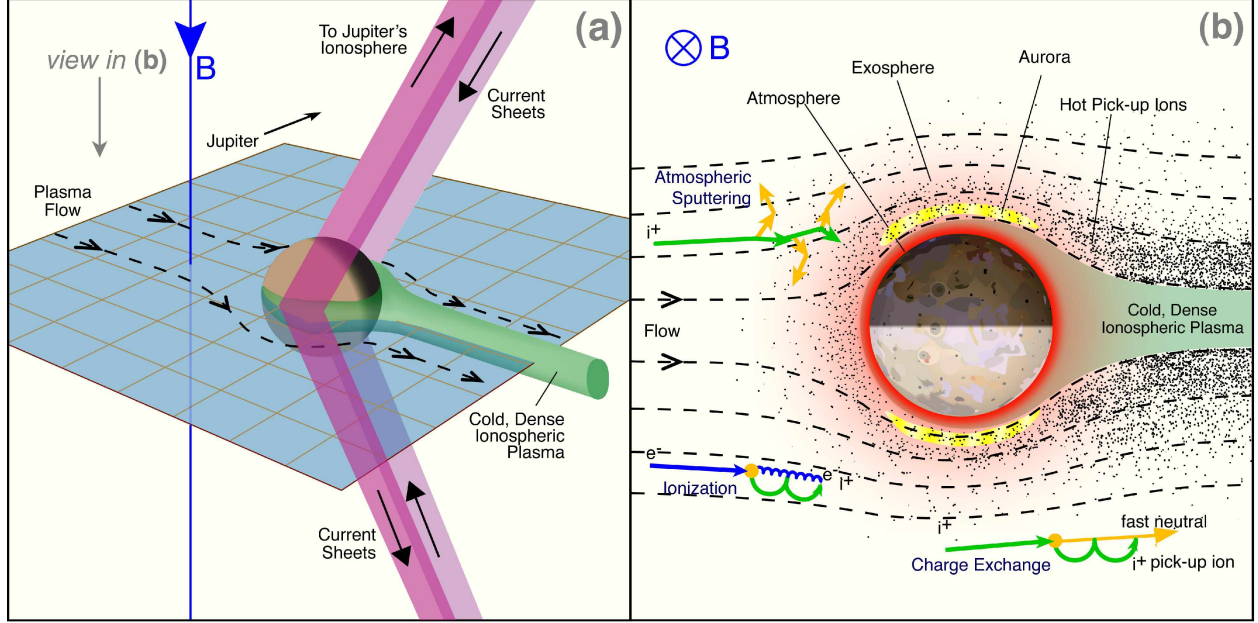


Figure 1.16: Interaction of the Jovian magnetosphere with Io. The corotating plasma of the torus interacts with Io's atmosphere, resulting in charge exchange through collisions of ions with neutral particles. The newly created ions are picked up into the plasma flow and brought to corotation due to momentum transfer from the magnetosphere [Bagenal and Bartlett, 2015].

2003]. The waves are also partially reflected back into the torus. The wave can be reflected and transmitted each time it encounters either the northern or southern boundary of the torus, generating secondary auroral spots [Bonfond *et al.*, 2008]. Reflection is dependent on the size of the incoming wave and the changing index of refraction within the torus. Large λ_{\parallel} waves tend to be reflected (i.e., with respect to the torus gradient scale length), while the small filamentary waves tend to be transmitted [Hess *et al.*, 2010]. The KAW scale dominates the interactions inside the torus, overcoming any of the inertial electron effects [Su *et al.*, 2003]. Outside the torus, k_{\parallel} has increased enough to allow IAWs to have a greater significance in the overall wave structure.

Analysis of the Io torus during encounters with the Galileo spacecraft has already confirmed the existence of ion cyclotron waves as a result of pickup of O^+ , S^+ , and SO_2^+ ions [Huddleston *et al.*, 1997; Cravay and Bagenal, 2000]. Figure 1.18 shows example spectra of the ion cyclotron waves observed by Galileo. Peak frequencies occur near the expected values of

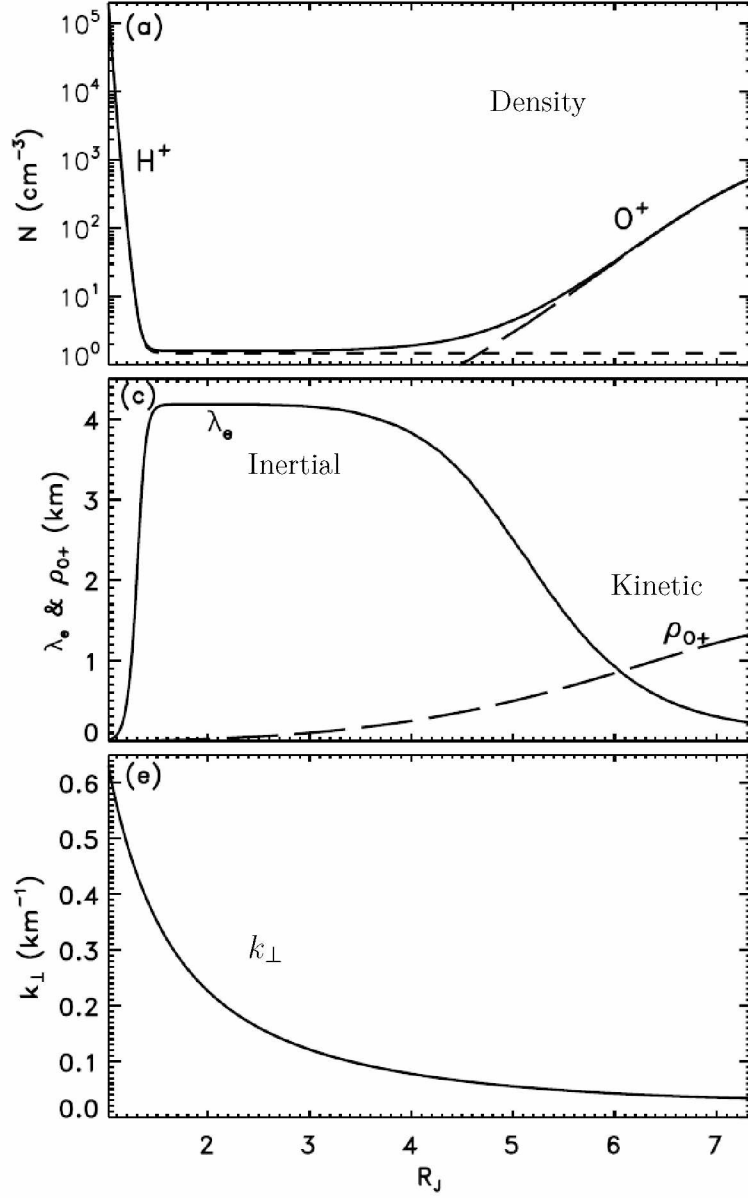


Figure 1.17: Background parameters for the gyrofluid model [Su *et al.*, 2006]. Top: Electron (solid line), H+ (dashed line), and O+ (long-dashed line) densities. Middle: Electron skin depth (solid line) and ion acoustic gyroradius (dashed line). Bottom: Perpendicular wave number.

pickup ion species [Blanco-Cano *et al.*, 2001]. Ion cyclotron waves are generated in response to the destabilizing of the ring beam velocity distribution of the pickup ions, which makes the waves a result of ion kinetic motion.

1.6 Small Scale Wave Investigation

The common theme throughout this thesis is the generation and propagation of dispersive waves in the giant magnetospheres. The source of the waves may be from the Io-Jupiter interaction, or from transport-related disturbances (e.g., Rayleigh-Taylor instability). Regardless of the source, these waves are introduced into a resonant cavity where wave reflection leads to the interaction between counter propagating waves - a key aspect for the generation of turbulence. The Io plasma torus and the middle magnetodisc are characterized by density gradients, as the majority of the plasma is centrifugally confined. The change in density acts as the resonant cavity for plasma waves. Figure 1.14 shows partial reflection and transmission within the torus as a result of the resonant cavity. Similarly, the formation of RT instabilities in the magnetodisc, which is determined by the growth rate (derived in Section 5.4):

$$\gamma^2 = gk_{\perp} \frac{\rho_2 - \rho_1}{\rho_2 + \rho_1} - \frac{2(k_{\parallel} B_y)^2}{\mu_0(\rho_1 + \rho_2)} \quad (1.12)$$

is limited by parallel wave lengths in the magnetodisc. The parallel wavelengths are also confined to a resonant cavity in the magnetodisc (See Figure 1.19). Parallel propagating modes also tend to correlate phase differences in the surface waves that form at different heights in the magnetodisc, and the interaction of those counter propagating modes can form a turbulent cascade. *The interaction of counter propagating waves in the Io torus is similar to those also found in a RT instability in the magnetodisc.* The RT instability in the magnetodisc also has a higher growth rate for large values of k_{\perp} , or very small wavelengths, where formation of the wave begins on ion kinetic scales. From the previous observation of waves and turbulence in the magnetodisc, as well as the broadband electron precipitation observed in the aurora, we can conclude that ion kinetic scale dispersive waves are important

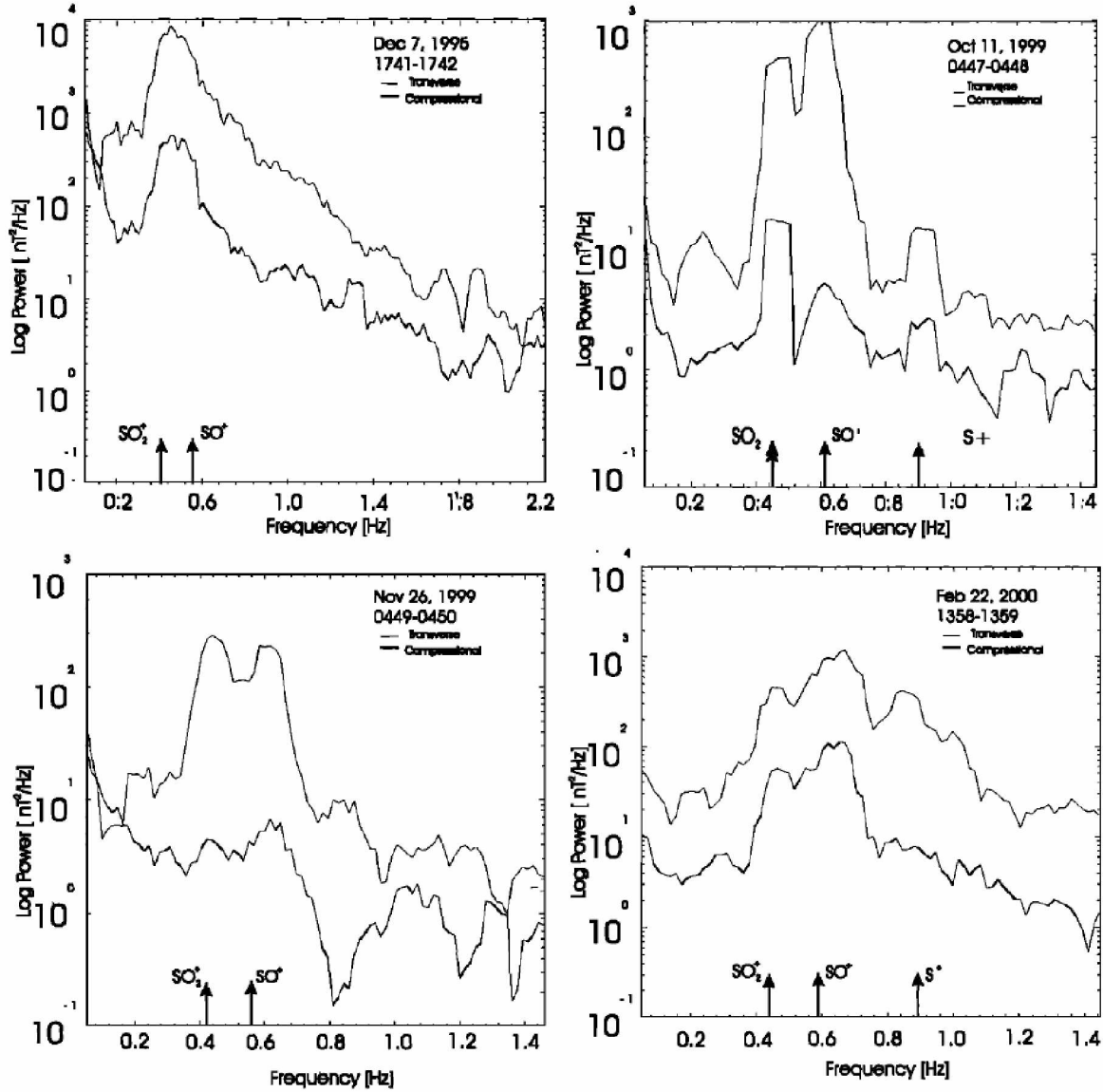


Figure 1.18: Spectra of the waves observed by Galileo during the four crossings of the Io torus. The thick line is the compressional power computed from the total magnetic field, and the thin line is the transverse power calculated from the trace of the spectral matrix minus the compressional power. Fourier estimates of the power were added together in bands of five frequencies. The arrows show the SO_2^+ , SO^+ and S^+ gyrofrequencies [Blanco-Cano *et al.*, 2001].

to energy and mass transport in the giant magnetospheres, and that turbulence is a possibility to account for some of the non-adiabatic heating in the magnetodisc. The investigation will focus on modeling the RT instability in two dimensions to study the effects of wave coalescence (or inverse turbulent cascade) on growth rates. Then we extend the model to three dimensions to capture the effect of k_{\parallel} on wave growth and turbulence. We divide our investigation into three sections: simulation of waves propagated in the Io plasma torus, 2D RT simulation of the magnetodisc, and 3D RT simulation of the magnetodisc. Our guiding questions for the each chapter include:

Io plasma torus:

- How much power from Io-induced waves is transmitted out of the torus, and what are their dispersive characteristics?
- Is there evidence of turbulence in the interaction of counter propagating waves in the torus?

2D RT instability:

- Does the RT instability exhibit coalescence of surface waves (i.e., does the dominant mode cascade to larger wavelengths)?

3D RT instability:

- Is turbulence present in the perpendicular modes of the RT instability?
- Is there evidence of a parallel electric field in the RT instability that is indicative of plasma decoupling from the magnetic field?
- Can we estimate k_{\perp} from the RT growth rate and the size of the resonant cavity and compare with observations?

We propose to investigate the radial transport of plasma through the RT instability and the propagation of waves in the Io torus using a local hybrid code. The code models individual ion motion, and is able to resolve the dissipation range of the turbulent cascade.

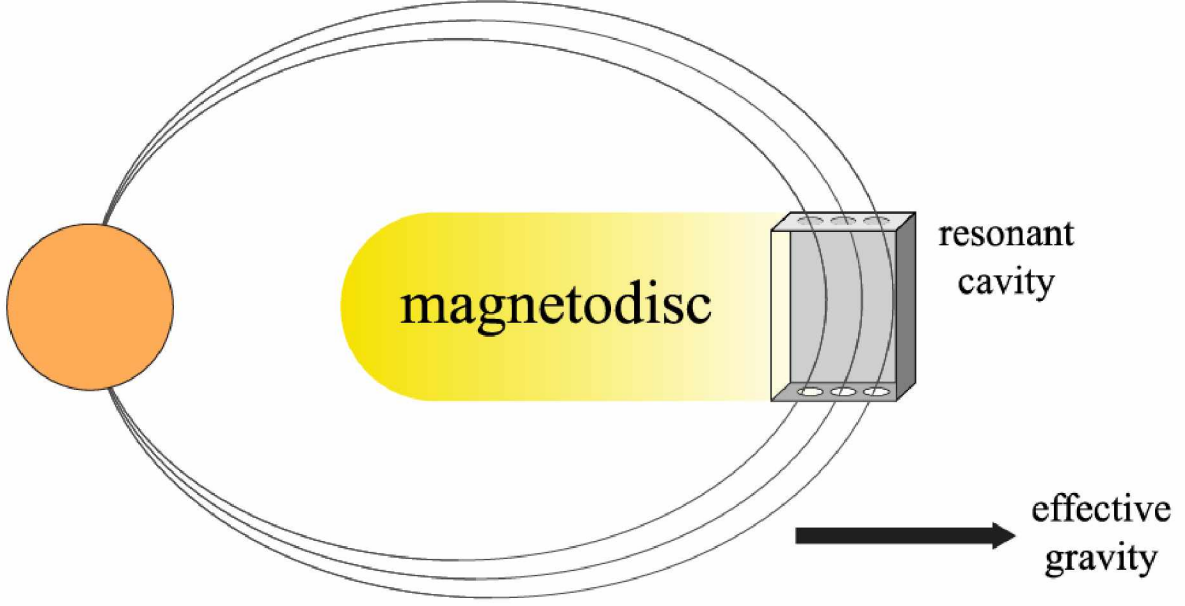


Figure 1.19: Resonant cavity inside of the magnetodisc. The density gradient in the magnetodisc acts as a resonant cavity for parallel propagating waves. Centrifugal force from the planetary rapid rotation acts as an effective gravitational force.

1.7 Hybrid Code

Previous modeling of the Io plasma torus and magnetodisc interaction were attempted using MHD models. MHD treats both the electrons and the ions in a single fluid limit and therefore lacks a mechanism to resolve wave features that result from individual particle motion at kinetic scales. It also cannot resolve the turbulent cascade beyond the inertial range. An alternative is to use a full particle-in-cell (PIC) model that treats all the plasma particles kinetically. This kind of simulation is very computationally expensive, and limits all runs to very local scales. As a compromise, we use the hybrid model of plasma simulation originally developed by *Swift* [1996] and *Delamere* [1998]; *Delamere et al.* [1999], which models the ions as individual particles and electrons as a massless fluid. The hybrid simulations are too computationally expensive to use as a global model, but are effective for localized regions of the magnetodisc. Three dimensional simulations are still limited to even smaller regions. The code maintains the assumptions that the plasma is quasi-neutral and non-radiative.

Ion motion is updated using the Lorentz force law. The electron flow is evaluated using Ampere's law for currents. Finally, Faraday's law is used to update the magnetic field to the first order. The electric field depends on the generalized Ohm's law, which is as follows:

$$\mathbf{E} = -\mathbf{u} \times \mathbf{B} + \frac{1}{nq} \mathbf{J} \times \mathbf{B} - \frac{1}{nq} \nabla p_e + \nu \mathbf{J} + \frac{m_e}{nq^2} \left[\frac{\partial \mathbf{J}}{\partial t} - \nabla \cdot (\mathbf{J} \mathbf{u} + \mathbf{u} \mathbf{J}) \right] \quad (1.13)$$

The first term in the expression is the motional field, and the second term is the Hall term, which scales with the ion inertial length ($\lambda_i = c/\omega_{pi}$). The third term is the gradient of electron pressure, which is only modeled in the hybrid code when an electron temperature is introduced. The fourth term is a resistive term based on ion-electron collision. The parameter ν can be adjusted to alter the effect of diffusion in the hybrid code. The final term is the electron inertial term, and is not represented in hybrid code, as the electrons are massless in this model. Additional details for the algorithms used in the hybrid code are in Appendix C.

We cannot hope to model every single ion in a particular volume. We just need enough to integrate particle statistics. As such, each ion has a weight w associated with it that is representative of the number of macro ions in its vicinity, so that grid cell density represents an accurate ion density:

$$w = \frac{n_{ppc}}{n_{real}} \quad (1.14)$$

where n_{ppc} is the number of particles (ions) in a grid cell and n_{real} is the modeled number density of ions. Adjusting n_{ppc} has a large impact on the runtime of the code, as a greater n_{ppc} means more particles must be simulated, but particle statistics improve. Additional particles per cell in select regions of the domain improve resolution in relevant regions. These extra particles will constitute a separate ion population that needs to be initialized.

The grid must resolve ion gyromotion to capture ion kinetic physics. A convenient parameter is the plasma- β , which represents the ratio of thermal pressure ($1/2 m_i n v_{th}^2$) to magnetic pressure ($B^2/2\mu_0$). Using the definition of β , we derive a relationship for the ratio of ion

thermal gyroradius ($\rho_i = \frac{m_i v_{th}}{qB}$) to ion inertial length:

$$\begin{aligned}
\beta &= \frac{1/2 m_i n v_{th}^2}{B^2/2\mu_0} \\
&= \frac{m_i n v_{th}^2 / \mu_0}{B^2} \\
&= \frac{m_i^2 v_{th}^2 n \mu_0 q^2}{q^2 B^2 m_i} \\
&= \frac{\rho_i^2 q^2 n \mu_0 \epsilon_0}{m_i \epsilon_0} \\
&= \frac{\rho_i^2 \omega_{pi}^2}{c^2} \\
&= \frac{\rho_i^2}{\lambda_i^2}
\end{aligned} \tag{1.15}$$

The thermal velocity of the ions are represented on the grid as gyromotion. The spacing of grid elements is on the order of λ_i , so that ion inertial effects are resolved (grid spacing is defined as a multiplier, α , acting on λ_i). As long as $\sqrt{\beta} \geq \alpha$, the grid spacing is less than ρ_i as well. In this case, the ions will cross a minimum of one grid cell boundary over the course of one gyration. If $\sqrt{\beta} < \alpha$, ion kinetic effects are below the resolution of the grid cells, and the frequency of ions moving across grid cells is lowered. In such a case, updates to the fields are not significantly influenced by individual ion gyromotion, and the simulation is reduced to modeling the plasma in the limit of Hall-MHD. The two-fluid nature of the hybrid code means that Hall physics are included regardless of grid resolution. The concern is that there is sufficient grid resolution to capture ion kinetic effects. (See Figure 1.20).

Another advantage of the hybrid code is that the ion velocity distribution function is accurately described. *Krall and Trivelpiece* [1973] describe the dispersion function for left hand circularly polarized modes (e.g., electromagnetic ion cyclotron waves) as

$$\omega^2 = k^2 c^2 + 2\pi\omega \sum_{\alpha} \omega_{p\alpha} \int \frac{\left[\frac{\partial f_{\alpha 0}}{\partial v_{\perp}^2} \left(1 - \frac{k_{\parallel} v_{\parallel}}{\omega} + \frac{k_{\parallel} v_{\parallel}}{\omega} \frac{\partial f_{\alpha 0}}{\partial v_{\parallel}^2} \right) \right] v_{\perp}^3 dv_{\perp} dv_{\parallel}}{k_{\parallel} v_{\parallel} - \omega - \Omega_{i\alpha}} = 0, \tag{1.16}$$

where α represents each present plasma species. This relationship is dependent on the

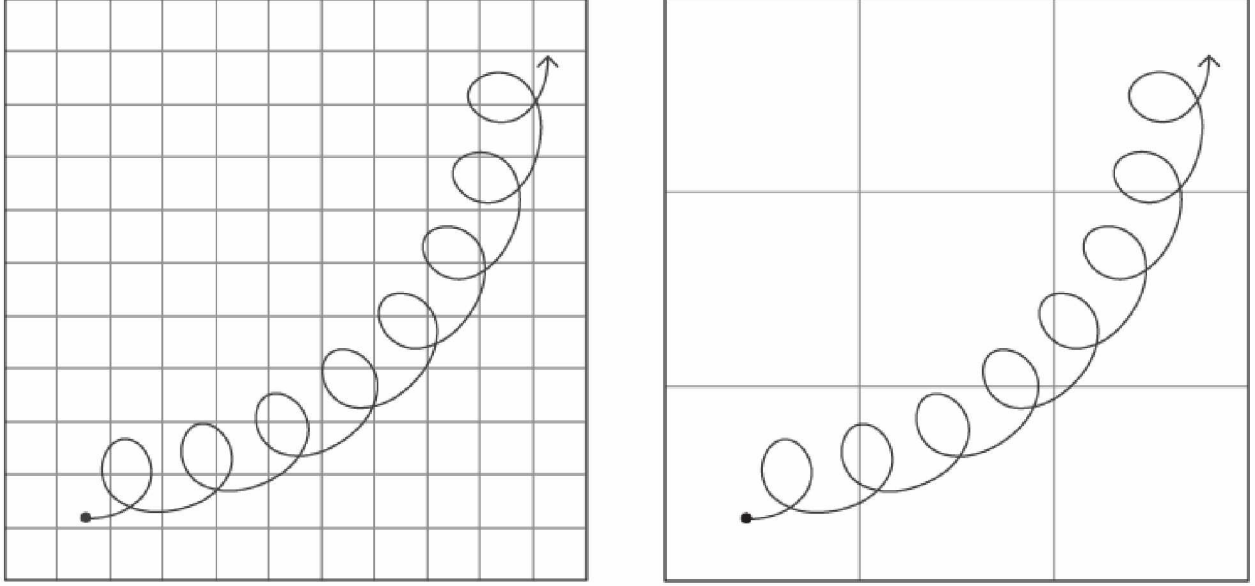


Figure 1.20: Resolved vs. unresolved ion motion. The left figure shows ion gyromotion on a fine grid cell. For each completed rotation, the ion crosses at least one grid cell boundary. In the right figure, ion motion is not resolved on the grid. As long as $\beta \geq \alpha$, gyromotion is resolved on the grid. For $\beta < \alpha$, ion kinetics are not resolved on the grid.

distribution functions of the ion species, and is thus dependent on ion kinetics. The dispersion function is difficult to solve analytically for general cases of ion distribution. Fortunately, the hybrid code self-consistently evolves the ion distribution function with time. As long as an unstable distribution (e.g., anisotropic ring beam) is initialized in the hybrid code, EMIC waves will be generated and propagate. It is not necessary for the grid to be at any particular resolution to produce this effect, as the grid is a representation of spatial scale, and the EMIC waves are dependent on the velocity distribution of the ions. Parallel grid resolution is only important insofar as we wish to reduce aliasing of the generated waves. Generating EMIC waves is even possible for one dimensional simulations, where ion gyromotion is not modeled on the grid. Because the ion velocity distribution evolves with each time step in the hybrid code, EMIC waves will form if the ions are initialized in a distribution that is susceptible to them.

As a test of the hybrid code in one dimension, we compare the dispersion of an Alfvénic perturbation in a low β plasma. A broad pulse in perpendicular velocity ($\sim 20 \lambda_i$) results in a

non-dispersive Alfvén wave that propagates in both directions along the field line. If instead a narrow pulse is initialized ($\sim 5 \lambda_i$ in width), the Alfvén wave is dispersive. The right-hand circularly polarized waves (whistlers), which have a high phase velocity, propagate ahead of the main Alfvén resonance. From these examples we show that the dispersion of the wave is a result of resolving the wave at the ion inertial scale (Hall physics). This is in contrast to numerical artifacts, which cause dispersion as an inherent limitation of resolving a convecting wave on a discrete grid. As a final example, we include the formation of the EMIC waves as a result of initializing a population of ions with a ring beam distribution. There is no initial velocity perturbation, so there is no transfer of momentum from the magnetic field to the ions, and no Alfvén wave. The ring beam distribution is unstable, so EMIC waves are generated. This is an example of an ion kinetic effect, which would not be present in a fluid simulation that does not include an ion distribution function. Throughout this thesis, we will highlight the unique kinetic aspects of the hybrid simulations.

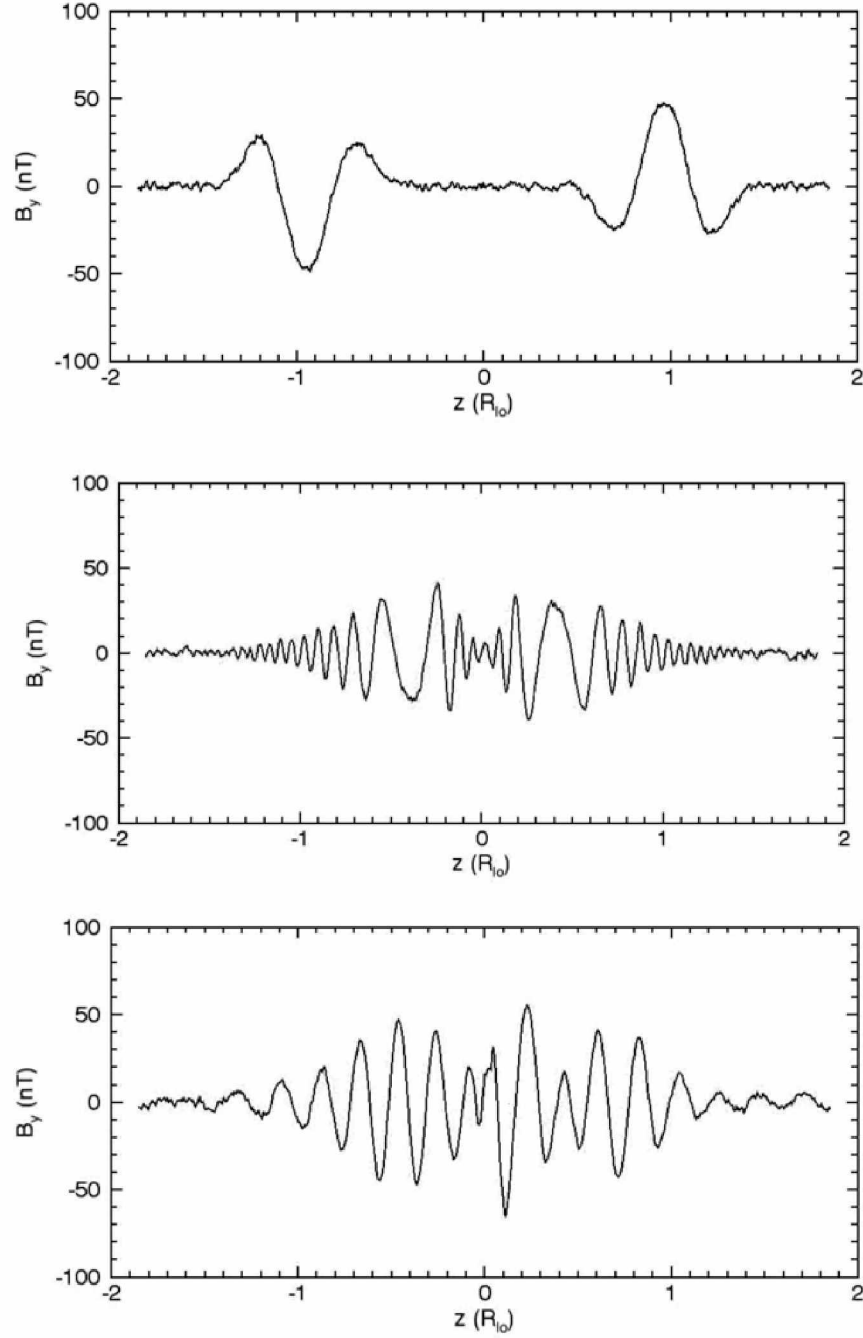


Figure 1.21: Test waves launched in the hybrid simulation. The top panel shows a Alfvén wave propagating with almost no dispersion, as the velocity perturbation is much greater than λ_i , and thus in the fluid limit. The middle figure is where the Alfvén wave was launched as a narrow pulse, with a width on the order of λ_i . The narrow perturbation causes the wave to disperse into left and right handed polarized modes, which meet at the Alfvén resonance. The bottom panel illustrates the ion cyclotron waves as a result of initializing a ring beam distribution of ions.

2.1 Introduction

The motion of Io within Jupiter’s magnetosphere and surrounding plasma torus generates 10^{12} W of power transmitted in the form of an Alfvén wave to Jupiter’s ionosphere where it generates auroral emissions. Observations of Jupiter’s aurorae in visible, UV, and radio wavelengths estimate the power of the aurora to be 10^{10} - 10^{11} W [*Hess et al.*, 2010]. Our goal is to determine the transmitted power of the Alfvén wave into accelerated electrons at small wavelengths in the flux tube. Our hypothesis is that the torus, as a resonant cavity, facilitates a turbulent cascade that accelerates local electrons. These waves can support parallel electric fields when the perpendicular scale length of the wave is on the order of the electron inertial length ($\lambda_e = c/\omega_{pe}$, the inertial Alfvén wave) or the ion gyroradius ($\rho_i = \frac{m_i v_{th}}{qB}$, the kinetic Alfvén wave (KAW)). These waves with extremely small perpendicular scale lengths carry energy into the ambient magnetic field and disperse, accelerating electrons by dissipating Poynting flux.

Hess et al. [2010] modeled the large and small scale propagation of these waves. They discovered that the large-scale Alfvén waves must be broken down and and filamented to small scales to permit wave transmission through the torus boundary and couple the wave to electron inertial lengths at high latitudes. They break up the power transmission profile into three distributions: 1. Large-scale, non-dispersive waves, 2. Filamented waves formed by plasma turbulence, and 3. Small-scale waves formed by compressional modes at the ion inertial length ($\lambda_i = c/\omega_{pi}$). Within the torus the KAW dissipates energy by accelerating electrons, while the IAW is the primary mechanism for dissipation at high latitude (Figure 1.17).

Magnetohydrodynamic (MHD) global Io simulations has been previously attempted (e.g. *Jacobsen et al.* [2010]). The *Jacobsen et al.* [2010] MHD model predicts the presence of electron beams in Io’s wake, which are then responsible for generating the aurora. Unfortunately,

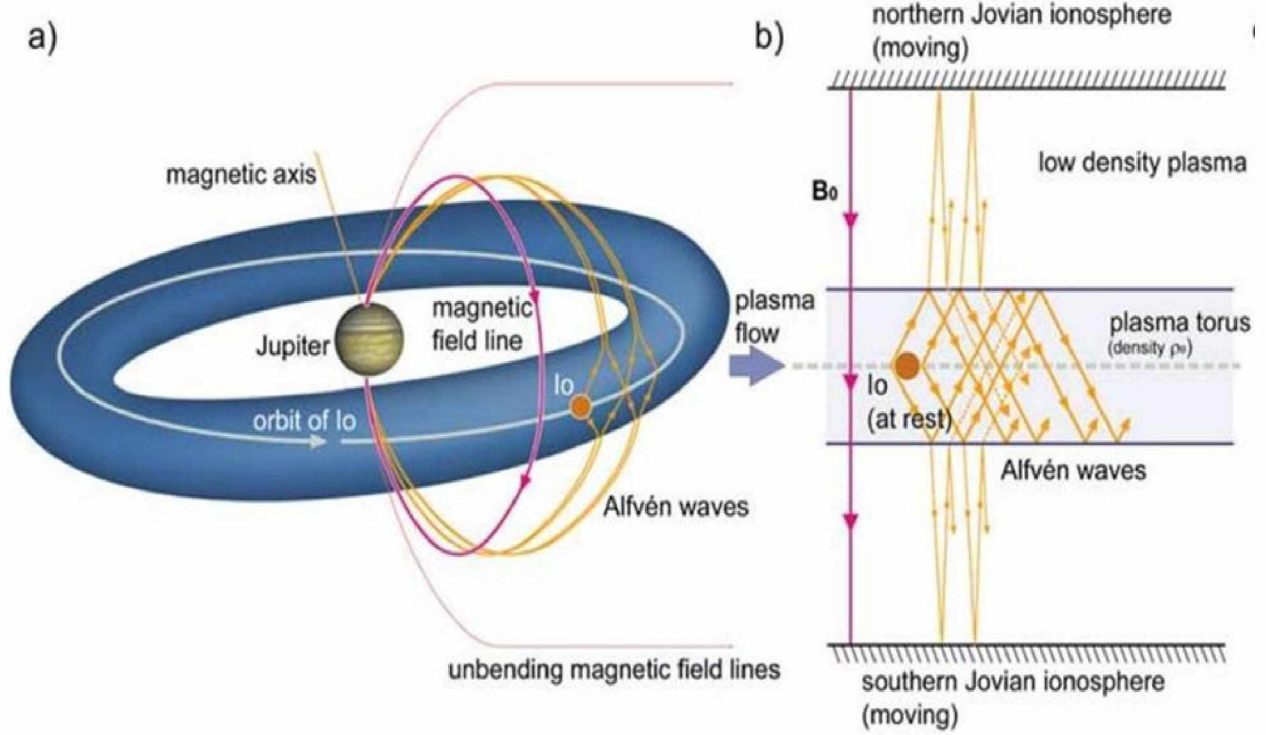


Figure 2.1: MHD model for the propagation of dispersive Alfvén waves in the Io plasma torus [Jacobsen *et al.*, 2010]. Alfvén waves that originate from Io propagate along the magnetic field line until they reach the torus boundary. The waves are then partially transmitted and mostly reflected [Jacobsen *et al.*, 2010].

MHD treats both electrons and ions as a fluid and therefore lacks any mechanism to resolve wave features at ion kinetic scales, meaning dispersive Alfvén waves would not be present in such a simulation. See Figure 2.1.

We begin by describing a model for the mass loading rate. We will be modeling the interaction of a flux tube of plasma as it encounters an obstacle to flow. This is similar to case where a plasma cloud moves through a magnetic field, subject to the frozen-in condition (See Figure 2.3). The cloud is considered to be a box with side length L . Starting with the MHD momentum equation,

$$\frac{\partial (\rho \mathbf{v})}{\partial t} + \nabla \cdot \left(\rho \mathbf{v} \mathbf{v} + \mathbf{P} - \frac{\mathbf{B} \mathbf{B}}{\mu_0} + \frac{B^2}{2\mu_0} \mathbf{I} \right) = 0, \quad (2.1)$$

we then focus only on the Maxwell stress of the magnetic field. The Divergence Theorem

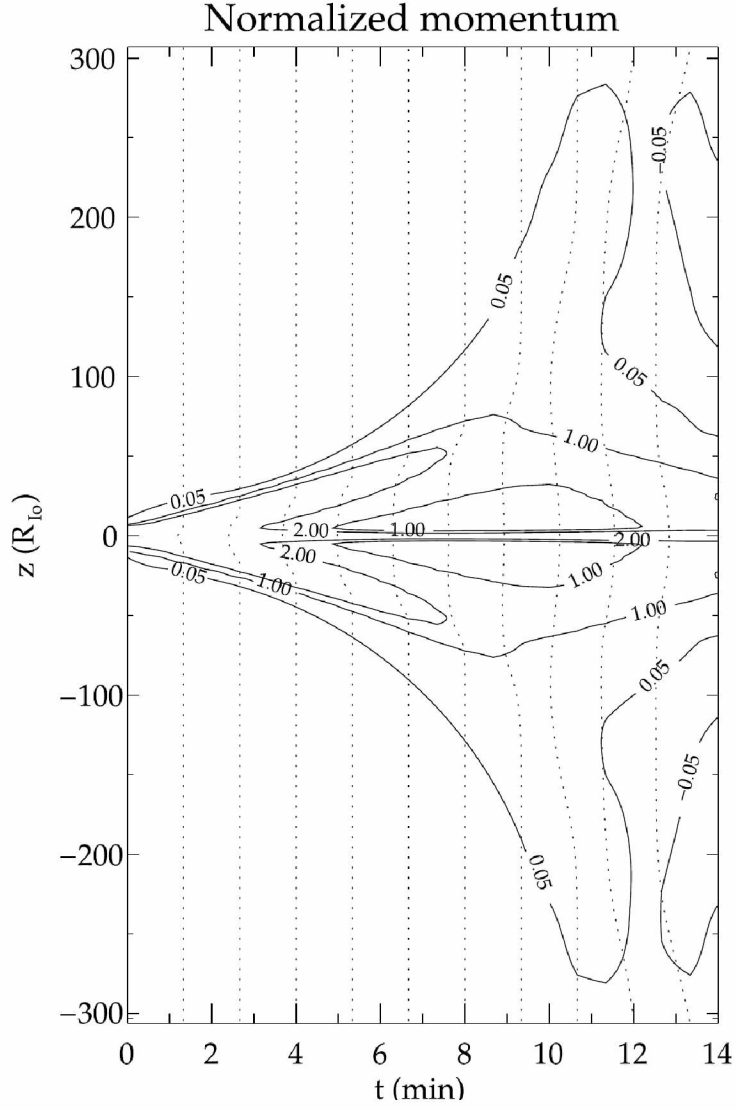


Figure 2.2: 1D mapping of the time evolution of the magnetic field line interacting with Io. The dotted lines are spatial representations of the magnetic field at 80 s intervals. The contours show normalized momentum. Much of the momentum is contained within the torus because of the reflection of Alfvén waves at the torus boundary. From *Delamere et al.* [2003].

allows us to calculate the force on the box by integrating the magnetic shear stresses over the surface of the box. Only the top and bottom sides of the box are subject to the magnetic shear.

$$\begin{aligned}
\dot{\rho}\mathbf{v} &= \int \overleftrightarrow{\mathbf{T}} \cdot d\mathbf{a} \\
&= (T_{xz}da)_{top} + (T_{xz}da)_{bottom} \\
&= \frac{+B_x B_z}{\mu_0} (+L^2) + \frac{-B_x B_z}{\mu_0} (-L^2) \\
&= \frac{2B_x B_z}{\mu_0} L^2
\end{aligned} \tag{2.2}$$

Now we let L^2 become the area of the interaction region where ions are picked up (A). Assuming that the corotational velocity v is constant, we can solve for the change of mass with time to get the mass loading rate:

$$\dot{m} = \frac{2B_x B_z A}{\mu_0 v} \tag{2.3}$$

2.2 Hybrid Code Initialization

Initialization of the hybrid code begins by specifying a grid and parameters for the background plasma that encompasses a flux tube that convects past Io and undergoes mass loading. For the one dimensional case, we have the computational resources to model a realistically sized flux tube that utilizes a straight magnetic field line through the domain, unlike a typical dipole. This is only because we are interested in wave propagation in the torus, where the local ambient magnetic field is directed perpendicular to the torus. Different stream lines will experience different mass loading rates, depending on the proximity to the atmosphere and thermal electron properties [Dols *et al.*, 2008]. The relevant dimension, z , runs the length of the flux tube, with the center of the mass loaded region initialized in the center of the domain, designated z_0 . The x direction corresponds to azimuthal plasma

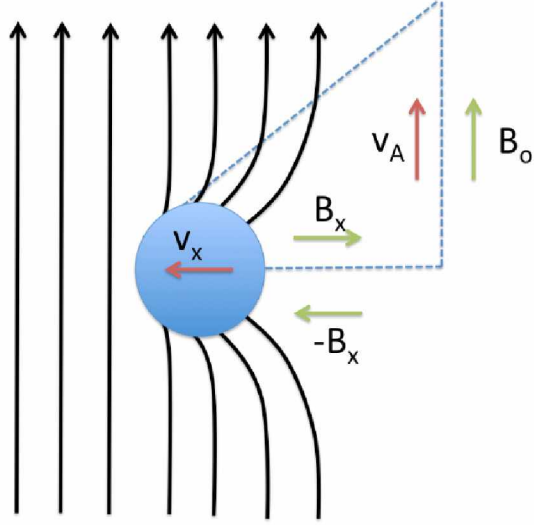


Figure 2.3: Convection of a cloud of plasma. A plasma cloud moves through a magnetic field, and drags the field lines with it. An Alfvén wave is launched from the resulting perturbation. The size of the perturbation depends on the ratio of the convection velocity to the Alfvén velocity.

flow, while y is the radial direction. The z boundary is periodic. The grid is initialized such that the space between grid points is $dz(z) = \lambda_i(z)$ so that we have resolution of the ion inertial length throughout the domain. Since density varies significantly at the boundaries of the plasma torus, the grid spacing is not uniform, but dependent on density. There is better resolution inside the Io torus than outside it, to resolve the initial formation of plasma waves. Outside the torus, density does not vary, and the grid spacing becomes uniform. The initial resolution of the grid in the inner torus because the lower density outside the torus increases the wavelengths of the Alfvén waves. The magnetic field is initialized to 1700 nT along z .

Maximum density inside the torus is $2 \times 10^3 \text{ cm}^{-3}$. We set the minimum density outside the torus at $n_0 = 4 \text{ cm}^{-3}$, making the maximum density five hundred times greater than minimum density ($H_0 = 500$). The density gradient is modeled as a Gaussian distribution,

giving us the following expression for density:

$$n(z) = n_0 \left(1 + (H_0 - 1) \exp \left[-\frac{(z - z_0)^2}{L_0^2} \right] \right) \quad (2.4)$$

where L_0 is $\sim R_J$ (This is $2400 \lambda_i$ for $dz_0 = \lambda_i = 24.4$ km at $z = z_0$). We initialize the density using a base number of 320 particles per cell (p_{pc}). After a few trial runs, it becomes apparent that there are not enough particles at the peak of the torus to maintain good particle statistics. The original constant number of particles per cell makes waves generated from mass loading too noisy, which disrupts the propagation of the waves through the torus. To counter this, we initialize additional particles per cell near z_0 . Again we use a Gaussian distribution for the number of extra particles placed per cell, p_{extra} .

$$p_{extra}(z) = 30 \exp \left[-\frac{(z - z_0)^2}{L_0^2} \right] \quad (2.5)$$

Finally, we apply the weighting function to each ion based on its location. The weighting function needs to account for the added ions, and adjust the weight of the original ions such that the density profile is generated as described in Equation 2.4. The function is just a ratio of simulated ions to modeled number of ions, so we get

$$w(z) = \frac{p_{pc} + p_{extra}}{n(z)L_x L_y dz(z)} \quad (2.6)$$

where L_x and L_y are the lengths of each respective domain (these are set to dz_0 for the 1D case). We then obtain the density profile shown in Figure 2.4. The domain stretches to $50 R_J$, far larger than the actual torus. The goal here is not to model the entire flux tube, but instead provide space for propagation of fast waves outside of the torus, while slower waves are still being generated. Extending the domain prevents interaction of counter propagating waves before all the waves have exited the torus.

The maximum value of the β based on density, magnetic field strength, and ion tempera-

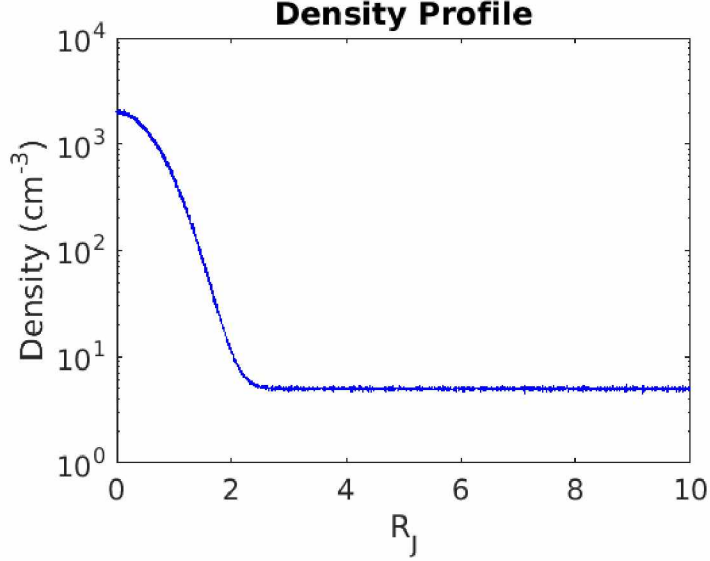


Figure 2.4: 1D density profile of the Io plasma torus. The boundary of the simulation extends far beyond any realistic model for the edge of the ionosphere. The profile is described using a Gaussian distribution.

ture within the simulated torus is 0.011, which decreases even further outside the torus. Such a low β is not relevant in a 1D model, as perpendicular ion motion is not modeled anyway. The value of ion kinetics in the hybrid model comes from the velocity distribution function. Recall that the dispersion relation for left-hand circularly polarized waves (Equation 1.16) is dependent on the velocity distribution function, which has a pole in the denominator ($k_{\parallel}v_{\parallel} - \omega - \Omega_i$ approaches zero for resonance). All of those quantities are represented in the hybrid code, so it will generate ion cyclotron waves as long as there is an anisotropic velocity distribution, even if perpendicular spatial ion motion is not part of a 1D grid.

Stability of the density gradient must be maintained for the duration of the simulation. For this, we implement an effective gravitational force (essentially the centrifugal force) that confines the plasma so that it remains consistent with its initialized density gradient. Starting with an expression for pressure balance,

$$\frac{\partial}{\partial z}(nT) = gnm_i \quad (2.7)$$

where T is the temperature profile, and m_i is the mass of the background ions. We wish to implement a uniform temperature profile, where the initial thermal velocity of the ions is 40 km s^{-1} . The background ions are set to the average ion mass of the torus, 23 amu . With those constants, we solve for g .

$$g(z) = \frac{T \frac{\partial n(z)}{\partial z}}{m_i n(z)} \quad (2.8)$$

Finally, substituting expressions for $n(z)$ and $\frac{\partial n}{\partial z}$, we have a final equation for gravity:

$$g(z) = \frac{-2T(H_0 - 1)(z - z_0) \exp\left[-\frac{(z - z_0)^2}{L_0^2}\right]}{L_0^2 m_i n_0 \left(1 + (H_0 - 1) \exp\left[-\frac{(z - z_0)^2}{L_0^2}\right]\right)} \quad (2.9)$$

Next, the flux tube must be loaded with pickup ions as it convects past Io's atmosphere. The mass loading occurs near the center of the domain. We find an approximate maximum value for mass loading based on Maxwell stresses from the loading region, starting with Equation 2.3. The maximum value of B_x can be found using the Walén relation

$$\frac{B_x}{v} = \frac{B_z}{v_a} \quad (2.10)$$

where v is the convection velocity and v_a is the Alfvén velocity. Solving for B_x , and substituting $v_a = \frac{B_z}{\sqrt{\mu_0 \rho}}$, we obtain the maximum mass loading rate for a saturated Alfvén wing:

$$\dot{m} = \sqrt{\frac{m_i H_0 n_0}{\mu_0}} B_z dy dz \quad (2.11)$$

Using our known parameters, $\dot{m} = 0.0079 \text{ kg s}^{-1}$ within the flux tube. We also modulate the change in mass loading rate over time so that the convection time is roughly one minute, and significant mass loading is limited to about 21 s . This is also done with a Gaussian function. Mass loading rate is now time dependent with

$$\dot{m}(t) = \sqrt{\frac{m_i H_0 n_0}{\mu_0}} B_z dy dz \exp\left[-\frac{(t - t_0)^2}{\tau^2}\right] \quad (2.12)$$

where $t_0 = 4000 \, dt$, $dt = 0.08 \, \Omega_i^{-1}$, and $\tau = 2000 \, dt$ (~ 21 s). The mass loading occurs at the flank of Io where the flows are high and the flux tube is closest to the atmosphere. Based on the flow speed and Io's radius, a Gaussian with $\tau \sim 21$ s is reasonable). Two ion species are mass loaded in equal proportion: $m_1 = 32$ amu and $m_2 = 64$ amu. We simulate the loaded ions by adding two particles for each processing unit near $z = z_0$ each time step. Weighting each ion is then as follows:

$$w = \frac{2n_{processors}m_{1,2}}{\dot{m} \, dt} \quad (2.13)$$

Each particle is assumed to be stationary with the atmosphere when it is ionized. As such, there is no velocity initialization of the ambient ions. Pickup ions are initialized with $v_x = -57 \, \text{km s}^{-1}$, which is the relative velocity of the atmosphere respect to the flux tube.

2.3 One Dimensional Model

Mass loading the central region of the torus creates a perturbation in velocity profile, where the new pickup ions are brought into the corotating flow. The pickup region is spatially very small, at just $3 \, \lambda_i$ along z , making for a very narrow broadband perturbation that will break into many frequencies as the wave propagates. There is then a momentum transfer from the background magnetic field in an attempt to bring the pickup ions into corotation. Perturbations in the velocity and magnetic field travel along in both directions along z , against the density gradient of the torus. The torus acts as a partial resonant cavity, where high frequencies pass through to higher latitude and the lower frequencies tend to be reflected.

Inside the torus, $v_a = 173.5 \, \text{km s}^{-1}$. Using Equation 2.10, we calculate the maximum amplitude of the wave at 550 nT. The hybrid simulation produces only a maximum perturbation of 320 nT while in the torus for the current mass loading rate, leaving the Alfvén wing unsaturated. Figure 2.6 shows the status of the wave after the main Alfvén wing has passed the edge of the torus, at $T = 2800 \, \Omega_i^{-1}$. The main Alfvénic perturbation is situated between 12 and 13 R_J . Ahead of the Alfvén wave is the right-hand circularly polarized (RH) mode,

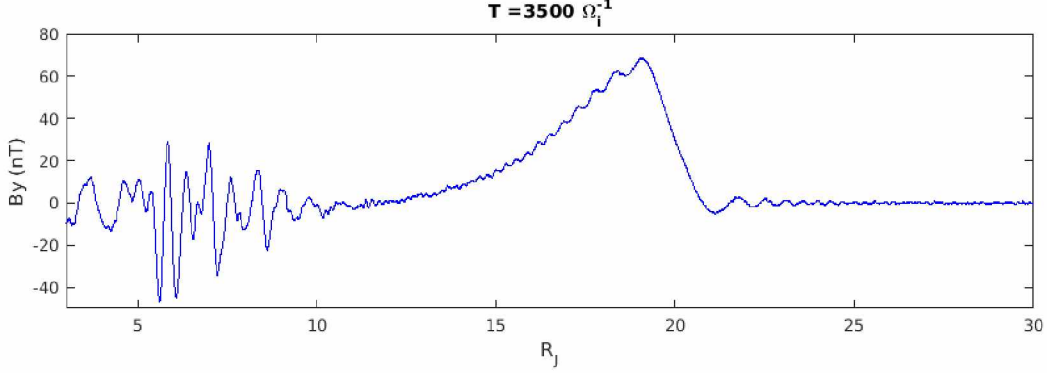


Figure 2.5: Waves transmitted through the Io plasma torus to higher latitudes, measured in units of R_J from the mass loaded region. The right hand circularly polarized waves have the highest phase velocity and precede the Alfvén wing. The left-hand circularly polarized waves follow behind the main perturbation. Ion cyclotron waves are generated last, as a result of the thermalization of the pickup ions.

which consists of high frequency electron waves that have a higher propagation speed than the non-dispersive Alfvén mode. Trailing the perturbation is the left-hand circularly polarized (LH) wave mode. Notice how for the RH mode, there is a phase difference between B_x and B_y , where the peaks of B_x lead the peaks of B_y . In the LH mode, B_y leads B_x . This is indicative of a change in polarization of the waves, from a RH mode to an LH one. The interchange occurs at the main Alfvén resonance, when the characteristic length scale is of the order of λ_i .

When the pickup ions are first brought into the flow, they begin to gyrate in the xy plane, forming a ring beam distribution in velocity space. The combination of a ring beam distribution to the ambient Maxwellian distribution creates a total distribution that is double peaked, and thus unstable. As the pickup ions are brought into corotation, the transfer of momentum shifts the center of the ring beam towards $-x$. Eventually the instability of the velocity distribution function thermalizes the pickup ions, scattering them into a more spherical Maxwellian distribution, similar to the ambient ions (See Figure 2.7). The result of this destabilization is the generation of additional high-amplitude electromagnetic ion cyclotron (EMIC) waves. These waves follow the main Alfvén mode (See Figure 2.8). As a check, we compare the observed frequencies with the gyrofrequencies of the present ions.

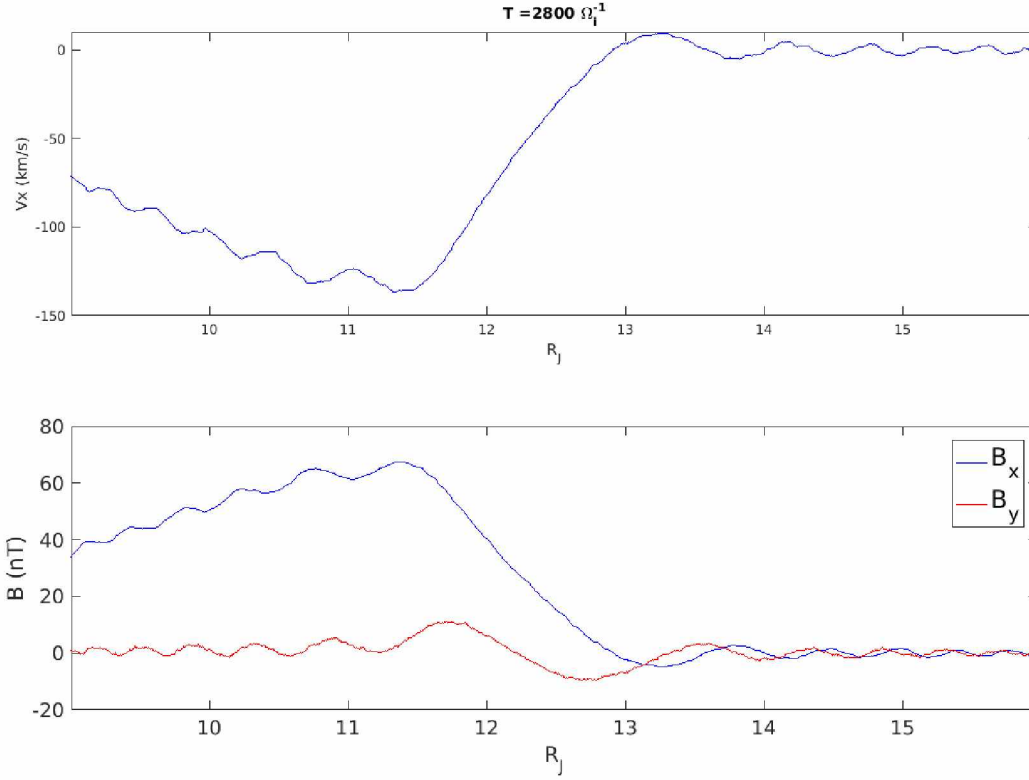


Figure 2.6: Alfvén wave just after exiting the torus. The wave is dispersive, with the right-hand circularly polarized wave ahead of the main Alfvénic perturbation, and the left-hand circularly polarized waves following, as indicated by the phase difference between the separate components of the wave. The Alfvén wing is accompanied by a large perturbation in convection velocity, which brings the higher altitude plasma below corotation.

Figure 2.9 shows the Fourier transform of all the ion cyclotron waves after they have exited the torus. Peak frequency matches that of the ambient ion species. Peaks are also present near the gyrofrequencies of the two mass loaded ion species. Peak power is just below each of the expected ion gyrofrequencies. From Equation B.24, the dispersion function indicates that the wave frequency only approaches ion gyrofrequency in the limit for large values of k . As such, most of the wave power is at a lower value of k , and has a corresponding lower frequency.

Next we examine the dispersion of all the generated wave modes by combining the entire temporal and spatial domains and performing a two dimensional Fourier transform, and generating a relationship for wave power as a function of frequency and wavenumber. This is shown in Figure 2.10. We compare this to some expected wave modes derived from dispersion relationships. First we start with the dispersion relationship that is derived in Appendix B, using Equation B.24:

$$\frac{\omega^2}{k_{\parallel}^2} = v_a^2 \pm \Omega_i^2 \lambda_i^2 \omega \quad (2.14)$$

where (+) corresponds to the RH mode, and the (-) for the LH mode. Solving for ω , we obtain

$$\omega = \frac{1}{2} \left(\pm \Omega_i \lambda_i^2 k_{\parallel}^2 + \sqrt{\Omega_i^2 \lambda_i^4 k_{\parallel}^4 - 4 v_a^2 k_{\parallel}^2} \right) \quad (2.15)$$

and include this function for each of the ion species. Included for reference are the maximum and minimum values for the non-dispersive Alfvén wave, the whistler mode, and the background ion gyrofrequency. The power spectrum spans most of the k space, but high frequency waves are lacking. The primary non-dispersive Alfvén wave is present at about 420 km s⁻¹. Most of the wave power is near the ion resonance for each of the included species. The whistler mode marks the upper bound of wave power.

Now we consider the amount of wave power that is transmitted through the torus based on

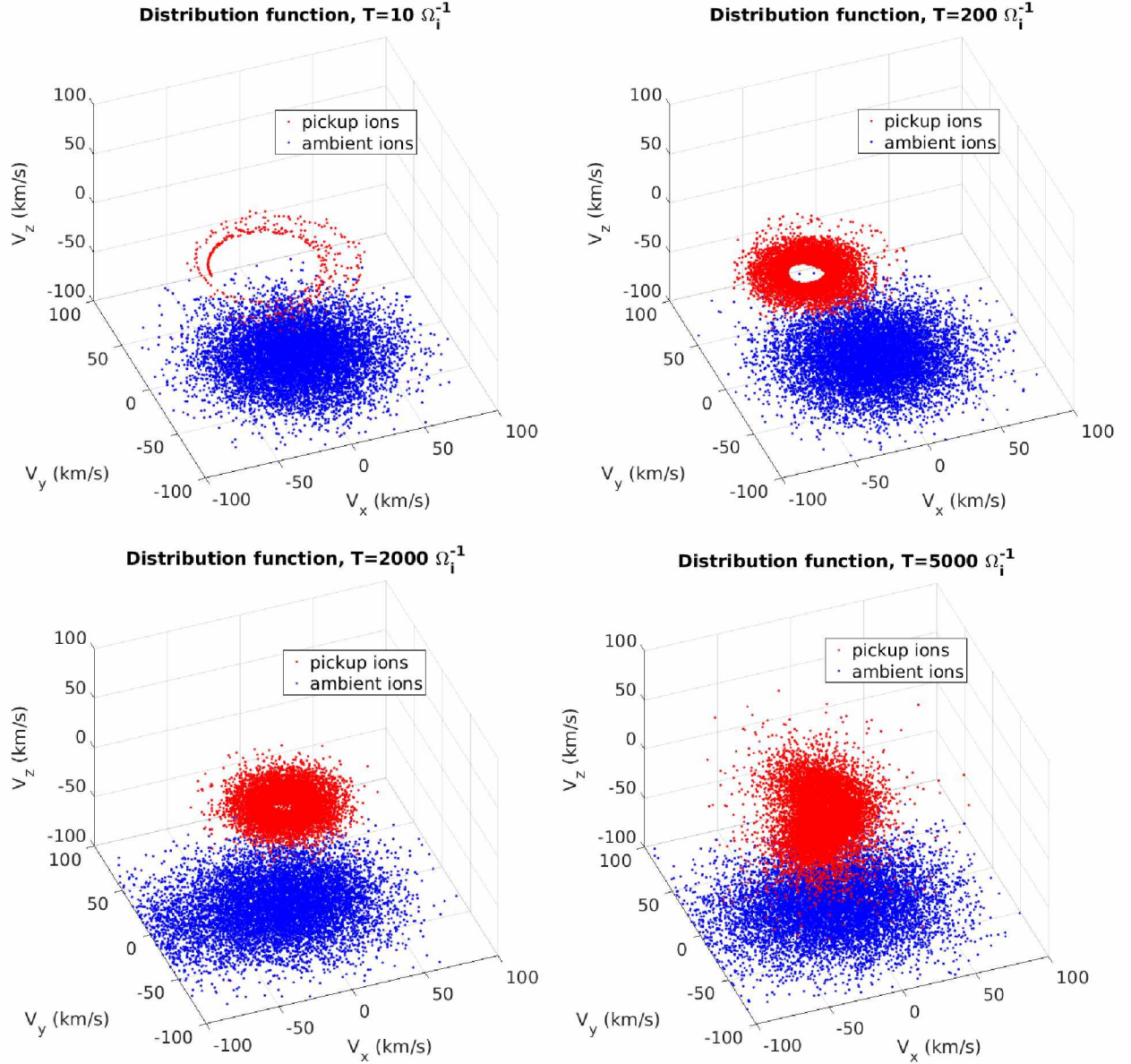


Figure 2.7: Ion velocity distribution with time. Background ions are initialized with a Maxwellian velocity distribution. They are represented in blue and flattened against the bottom panel. Ions that are picked up through charge exchange have an initial ring beam distribution of $\sim 57 \text{ km s}^{-1}$. This distribution is unstable and thermalizes into a Maxwellian distribution with the background ions. The second figure shows the widening of the distribution as more pickup ions are added. The ring beam is offset until momentum is transferred from the magnetic field to the pickup ions.

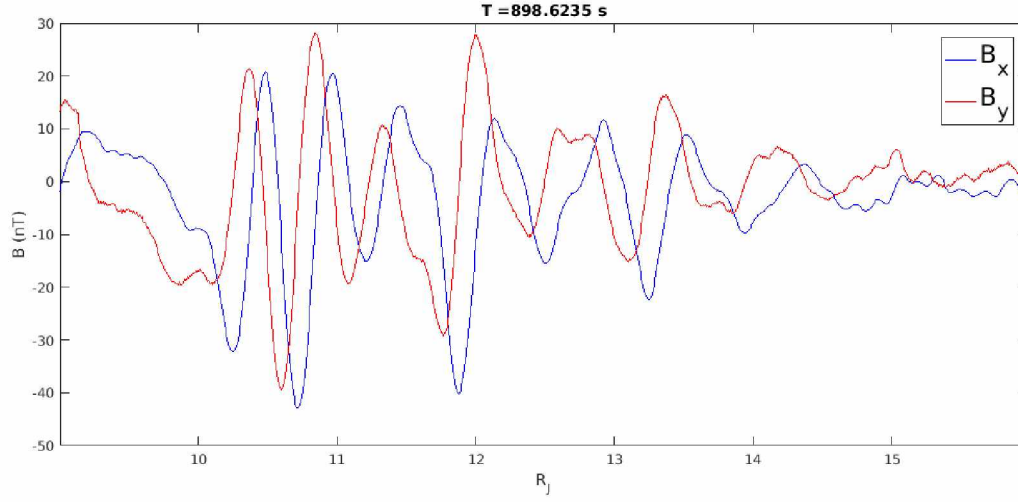


Figure 2.8: The ion cyclotron waves following the main Alfvén wave. There is a phase difference between B_x and B_y , indicating that the wave is left-hand circularly polarized.

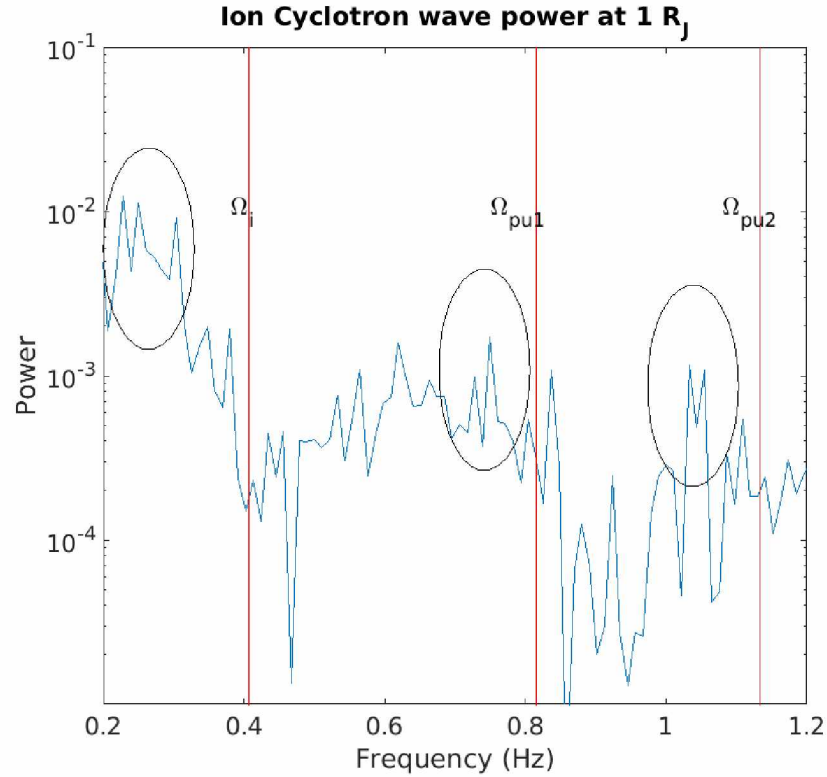


Figure 2.9: Frequency range of wave power in the torus after the passing of the main Alfvén wave. Each of the present Ion species is indicated with its corresponding gyrofrequency. Majority of the wave power is just below each of the expected frequencies.

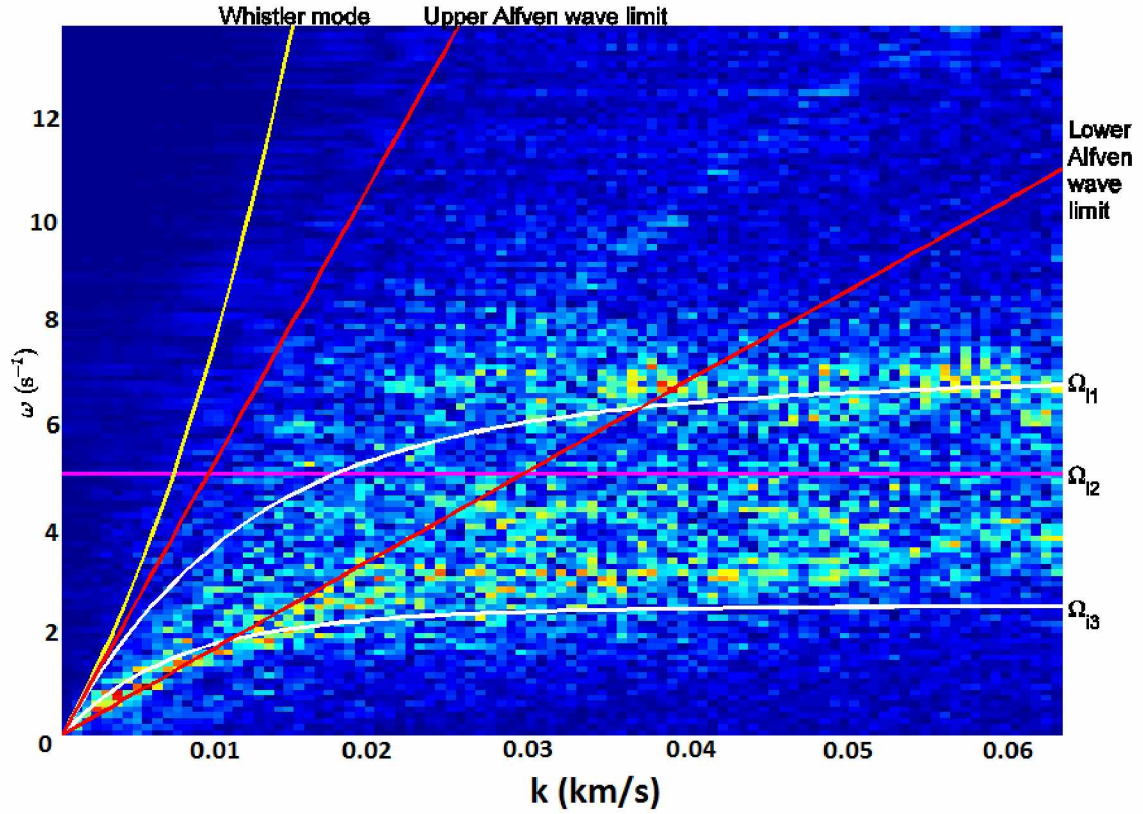


Figure 2.10: Kinetic Alfvén wave dispersion for parallel propagating waves. The red lines represent the upper and lower bounds for the non-dispersive Alfvén wave, based on minimum and maximum density. The white lines are the ion cyclotron frequencies of the two pickup ion species. Finally, the whistler mode is represented in yellow.

mass loading rate. We use the integrated Poynting flux described by the following equation:

$$P(z, t) = \int_0^t v_x(z, t') B_y(z, t') B_z dt' \quad (2.16)$$

Most of the wave power is carried by the main Alfvén perturbation. As the wave front passes through a region, the integrated Poynting flux increases. Reflected waves decrease the integrated Poynting flux as the reverse of the wavefront is added to the total sum of flux. For this, we consider three mass loading scenarios: low, medium and high, representing changes in the the flux tube’s interaction with Io’s atmosphere. Increased proximity to the atmosphere can be modeled as an increase the cross sectional area of the interaction ($dydz$), which has a linear effect on the mass loading rate. For each of these we modify \dot{m} to account for different mass loading targets. The medium case is unchanged. For the low case we use a scalar multiple of a half, while the high case uses a multiple of four. As expected, higher mass loading rates generate more power which propagates to higher latitude. Power transmission is limited by reflection along the torus density gradient. For all cases, the ratio of transmitted power to generated power is about 0.53. Since the time scale for mass loading is constant in all cases, the wavelength of the Alfvénic perturbation is the same in each simulation. We then expect that each case would have similar transmission coefficients.

2.4 Two Dimensional Model

We now expand our model to two dimensions. The one dimensional model can only accommodate variations along the flux tube, or parallel to the magnetic field. We are interested in modeling KAWs in the torus, so we need to include variation in at least one direction perpendicular to the magnetic field.

Adapting the initialization to the two dimensional case requires a few modifications. We keep the plasma parameters the same, but change the scale of the simulation by changing n_z to 401, and reducing the particles per cell to 50. No density gradient is introduced,

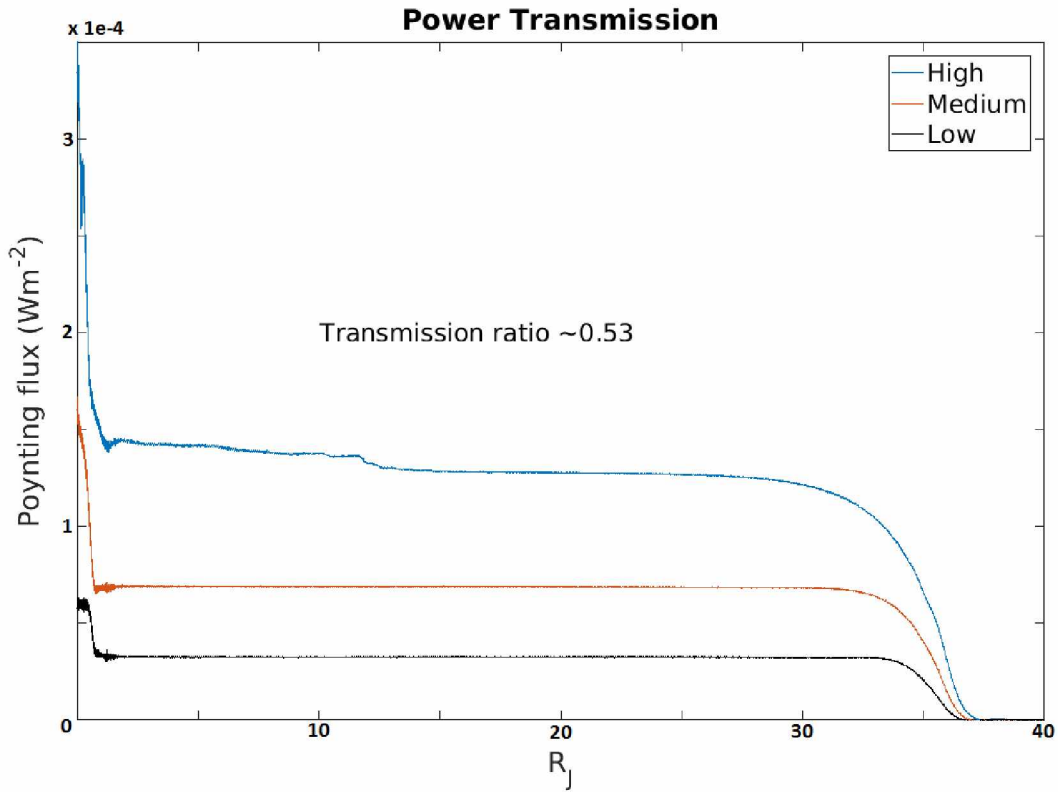


Figure 2.11: Alfvén wave power transmission in the Io plasma torus. Only $\sim 53\%$ of the original Alfvén power spectrum escapes the torus. The rest remains in the resonant cavity. The integrated Poynting flux drops off at $35 R_J$, which is the leading edge of the Alfvén wave.

negating the need for a balancing gravitational force, grid stretching, or individual particle weighting. A few test cases are run without mass loading ions, but produce waves by initializing perturbations in bulk ion momentum. In these cases, the bulk velocity of the ions is initialized to 57 km s^{-1} along x , while the perturbation represents a decrease in momentum due to subcorotation of mass loaded plasma within the torus. Velocity perturbations are modeled using Gaussian or sinusoidal initializations.

With the two dimensional model we expand the y dimension. Instead of modeling the entire flux tube, we start by using a few test cases. The first simulation is set up by applying a Gaussian perturbation to v_x with an amplitude of 57 km s^{-1} and a width of just $2 \lambda_i$, instead of applying the mass loading routine. This simplification is just an ad-hoc perturbation to promote wave formation and is not self-consistent with mass loading from pickup ions. In the MHD limit (where the velocity perturbation is much greater than λ_i), such a perturbation would have no large scale effect on ion density. In this case, where λ_i is resolved, ion inertia is relevant. Plasma- β is the same as in the 1D simulation ($\beta = 0.011$). The Alfvén wave front causes a polarization current, prompting ions on the wave front to drift off their initial field lines. The collective motion of the ions sets up a density gradient along the wave front. The Alfvén wave is also no longer limited to propagating along z , and now has a k_\perp component. Figure 2.12 shows the evolution of the Alfvén wave in B_y . The oblique fast mode runs through the periodic boundaries and interacts with its counter propagating counterpart, which begins the filamentation of the waves.

2.5 2D Turbulent Wave Interaction

To further investigate wave propagation and turbulence at the ion kinetic scale, we initialize a 2D domain with large bulk velocity perturbations at the ion inertial scale in near proximity to each other. We accomplish this by abandoning the torus model and setting the domain to a uniform density ($n = m_i H_0 n_0$) with a grid resolution of $0.1 \lambda_i$. Velocity perturbation is not localized, but instead filled with a large sinusoidal pattern in y and z ,

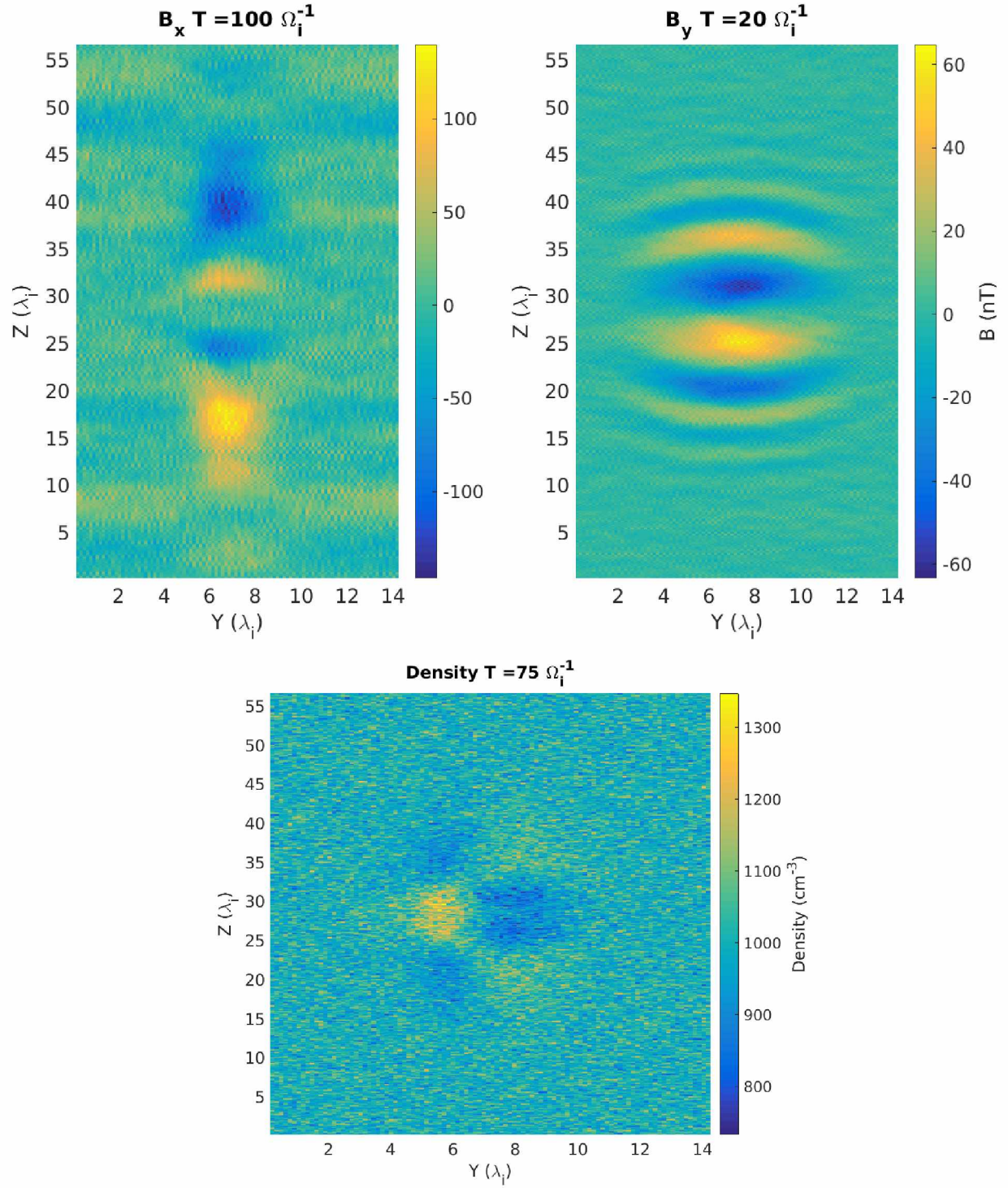


Figure 2.12: 2D Alfvén wave propagation in B_y, B_x , and density in the yz plane. A velocity perturbation that is on the order of λ_i launches Alfvén waves that propagate along z . The wavefront causes ions to gyrate from their initial position and create a density gradient.

reminiscent of an “eggbox” (See Figure 2.13). The peaks of the sinusoid are separated by $7 \lambda_i$, and have a maximum amplitude of 200 km s^{-1} . The electron temperature is set to 100 eV. β is still 0.011, but with the fine grid resolution, ρ_i is barely resolved on the grid ($\sqrt{\beta} = 0.1049 > \alpha = 0.1$). The multiple velocity perturbations are analogous to placing a bunch of Io satellites in close proximity so that there is immediate interaction of counter propagating waves. Just like the 2D torus model, density separation is exhibited on the grid after about $30 \Omega_i^{-1}$ due to ion motion that is not captured in MHD (See Figure 2.13).

As a contrast, we also conduct the same simulation near the MHD approximation by changing the peak separation to $50 \lambda_i$ and increasing the grid spacing to compensate. The MHD limit case does not exhibit density separation, suggesting that the density separation is an ion inertial effect (Hall MHD).

Contrasting the dispersion relationships for each, we see that in the MHD scale simulation, wave power is correlated with the non-dispersive Alfvén wave ($\omega/k = v_A$). The ion inertial scale simulation has no discernible power in the main Alfvén mode, but a faint signature for the KAW. Most of the wave power is concentrated at the wavenumber of the initial velocity perturbation and its multiples (Figure 2.14). The KAW is comparatively weak for the chosen β parameter.

When we take a fast Fourier transform of B_x along x at $z = 28 \lambda_i$, we obtain a relationship of wave amplitude compared to k_\perp (See Figure 2.15). The result is a Kolmogorov profile for perpendicular wavenumber. Energy is transported into shorter wavelengths until it reaches λ_i . High grid resolution allows more dissipation beyond this scale. One initially surprising aspect is that there is almost no transfer of energy from the waves to the ions to accomplish heating via ion Landau damping. Field energy and particle energy are both conserved throughout the simulation. Plasma- β is too low for the turbulent cascade to dissipate energy into the ions. Greater heating requires a larger ion gyroradius, such that $k_\perp \rho_i \sim 1$. Landau damping becomes more significant when $\beta \sim 1$ [Lin *et al.*, 2010; Johnson and Cheng, 2001].

To verify the ion heating, we jettison the Io-like plasma conditions by decreasing B_0 to

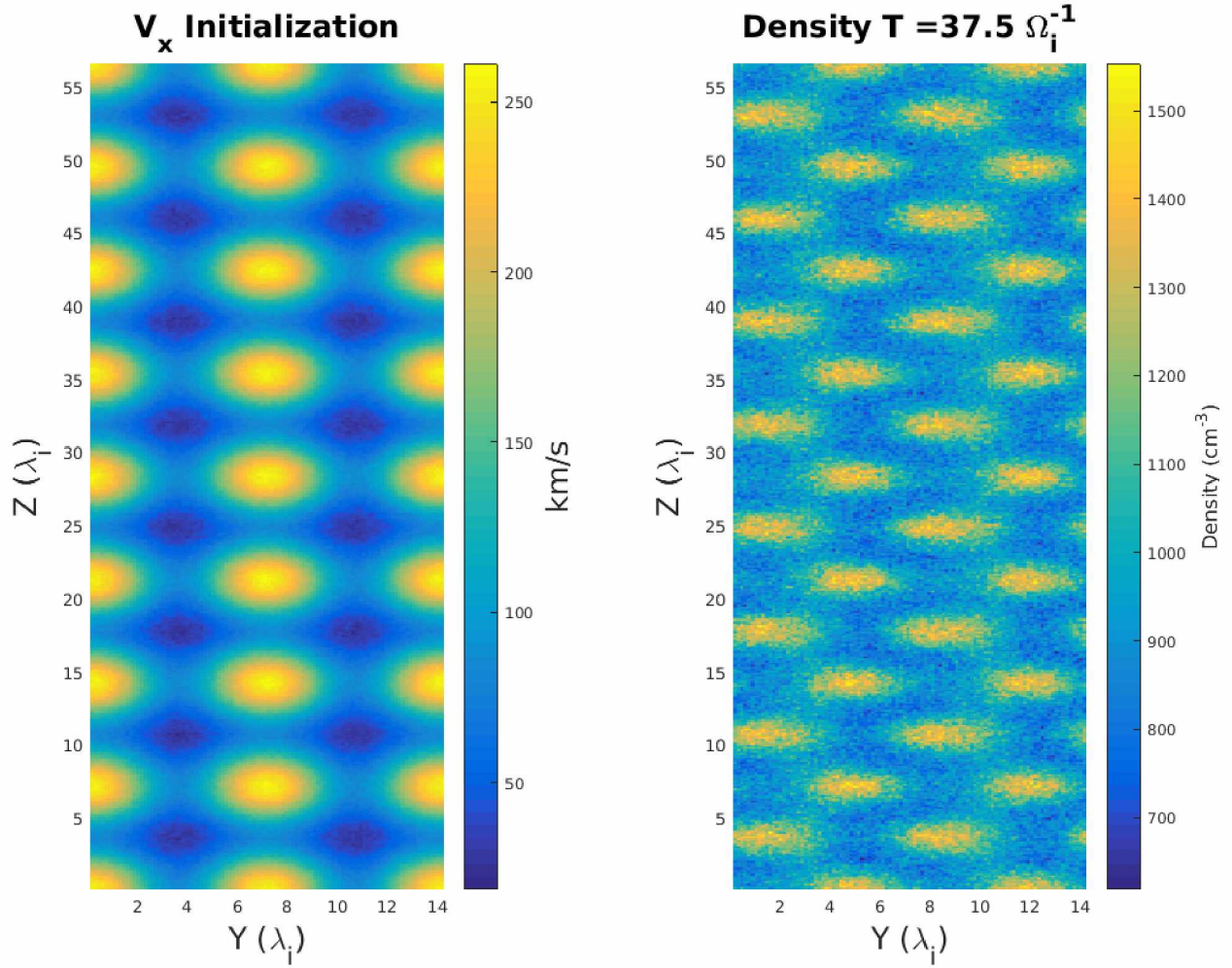


Figure 2.13: Eggbox velocity perturbation. The left figure shows the bulk velocity distribution, while the right figure corresponds to density perturbations within the domain at $37.5 \Omega_i^{-1}$. The scale of the velocity perturbation is on the order of λ_i . In the fluid limit, the density profile is uniform.

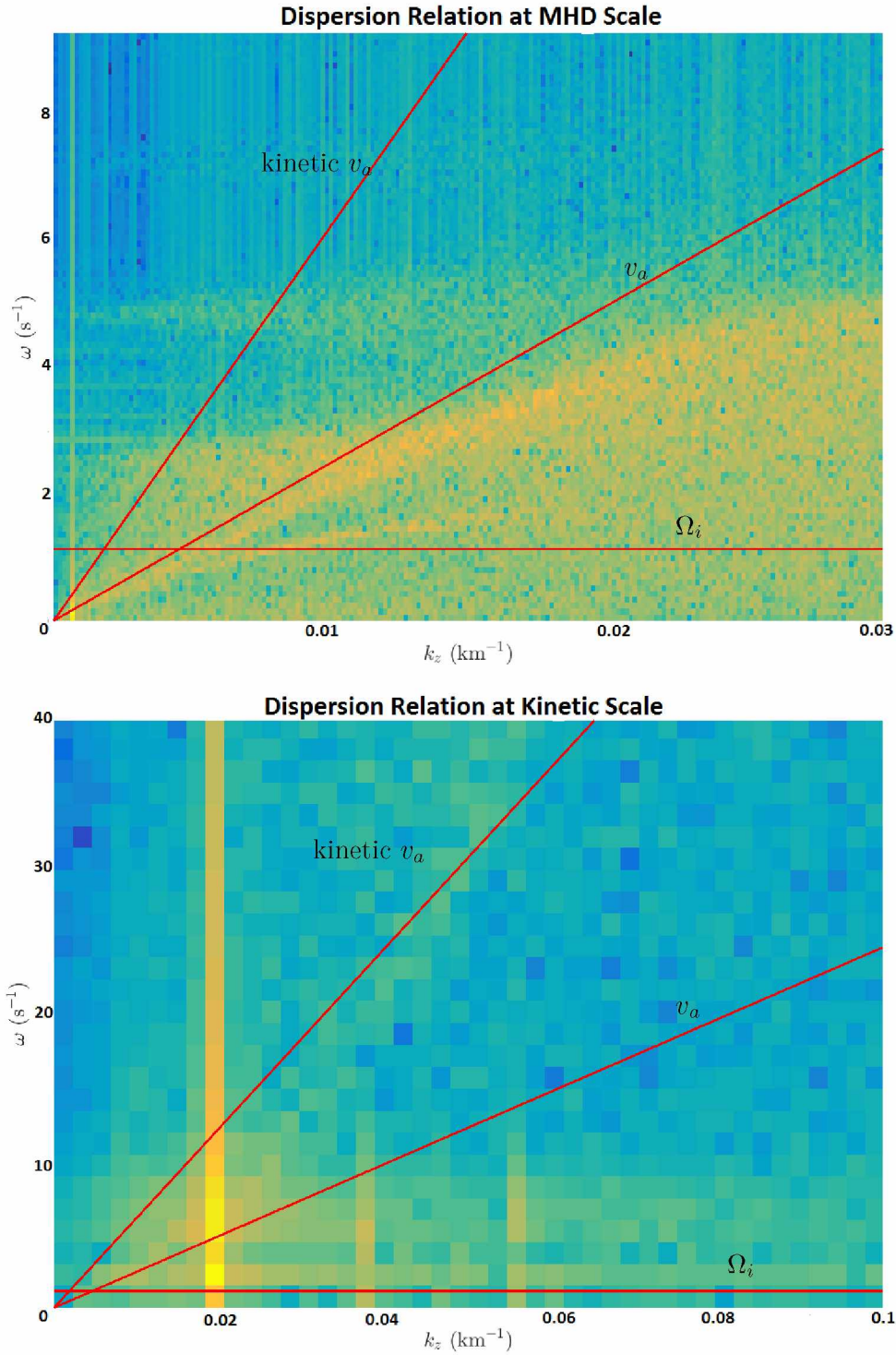


Figure 2.14: Dispersion relations at the fluid and kinetic scale. The left figure shows the wavepower is focused in the primary dispersionless Alfvén wave, with no kinetic effects. On the right, more wavepower is concentrated in the kinetic Alfvén wave. The strong vertical signal is the size of the initial perturbed wavelength.

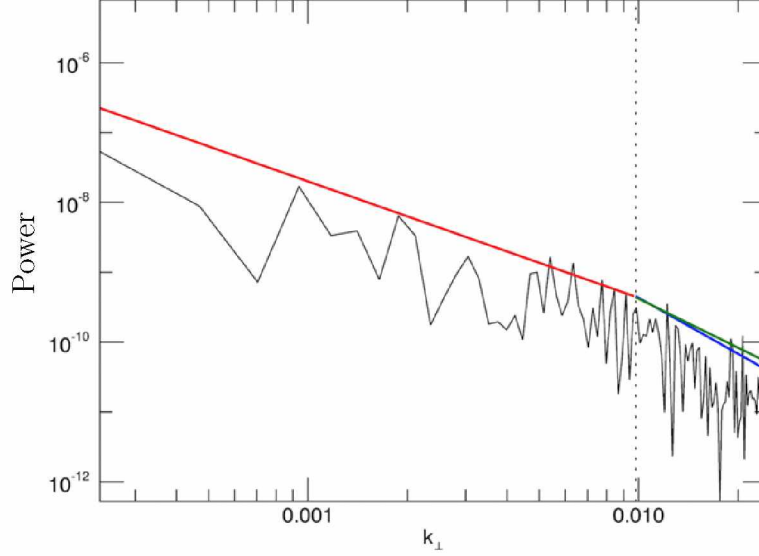


Figure 2.15: Evidence of turbulence from the frequency analysis due to the interaction of counter propagating waves. The red line has a slope of $-5/3$. The knee occurs at λ_i . The remainder of the plot has a slope of $-7/3$.

100 nT and increasing the ion thermal velocity such that $\beta = 1$. These parameters are more applicable to conditions in Jupiter's middle magnetosphere. Figure 2.16 plots the normalized ion energy over time. After the initial transitory period, there is a rapid gain of ion energy relative to wave energy. After about $60\Omega_i^{-1}$, ion heating rate slows. Near the end of the simulation, the normalized energy peaks above one, indicating that there is a small increase in overall energy within the domain. We attribute this to the propagation of small numerical errors, so a small percentage loss or gain of total energy is not unusual.

2.6 Conclusion

The hybrid simulation of wave propagation along the Io flux tube is unique in the fact that it self-consistently models momentum transfer between pickup ions and the ambient magnetized plasma. All previous attempts relied on providing a perturbation in velocity, or modeling a conducting obstacle to plasma flow [Wright, 1987; Delamere *et al.*, 2003; Jacobsen *et al.*, 2010]. The hybrid simulation is more realistic in its treatment of momentum transfer by inserting individual ions into a plasma flow which are then influenced by the

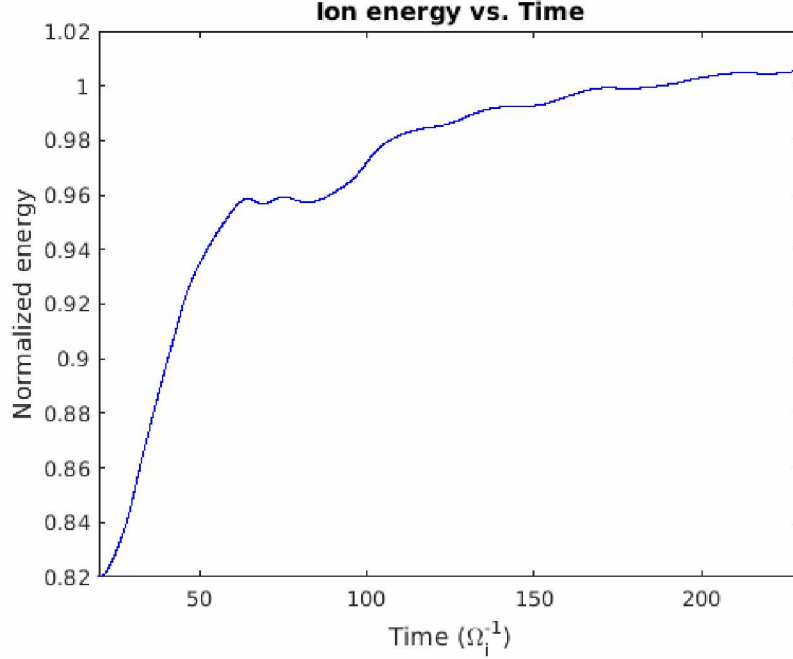


Figure 2.16: Ion heating over time for the “eggbox” domain with plasma- $\beta \sim 1$. The energy is normalized to the total energy present in the initialized domain. Energy in the domain is shared between waves and particles.

ambient electric and magnetic field. Momentum transfer from the ambient plasma is what restores corotation. It also models ion kinetic effects as a result of accurately evolving the ion distribution function (generation of EMIC waves).

From the one dimensional study, we have the Poynting flux generated within a flux tube to be $5 \times 10^{-5} - 3 \times 10^{-4} \text{ W m}^{-2}$, which varies based on the mass loading rate. About 53% of the generated power escapes the torus as part of the Alfvén wave, which is greater than earlier attempts to estimate wave power transmission by *Wright* [1987] and *Delamere et al.* [2003]. This is independent of the mass loading rate. Instead, the transmission ratio is more dependent on the size of the Alfvénic perturbation, which is determined by the interaction time between the Io and the convecting flux tube. Flows around Io are incompressible, so the interaction time of each streamline is roughly the same [*Dols et al.*, 2008]. Figure 2.17 shows the streamlines around Io and the changes in relative flow velocity.

Hess et al. [2010] calculate the a reflection coefficient for a continuous density transition

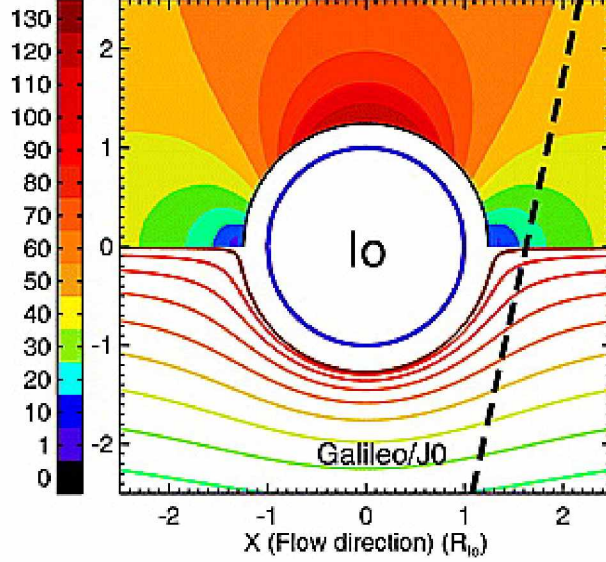


Figure 2.17: Incompressible plasma flows around Io. The colored upper half refers to the color scale on the left and shows the relative speed of the plasma flow. The bottom half shows a number of modeled stream lines. The dotted line is the trajectory of the Galileo spacecraft. Streamlines closer to Io have faster flows, but have to be diverted around Io. Each streamline has the same interaction time on average [Dols *et al.*, 2008].

where the length scale (L_0) is larger than the Alfvén wave (λ_{\parallel}). This is applicable to the 1D torus simulation with a Gaussian distribution in density. The reflection coefficient is given by

$$R = \frac{\lambda_{\parallel}}{L_0} \left(\frac{n_1 - n_2}{n_1 + n_2} \right), \quad (2.17)$$

where $n_{1,2}$ are the indices of refraction (c/v_A) at the peak of the torus and outside the torus respectively. Inside the torus, we measure λ_{\parallel} to be $\sim 0.5R_J$, and $v_{A1} = 173.5 \text{ km s}^{-1}$, $v_{A2} = 3880.6 \text{ km s}^{-1}$. The calculated reflection coefficient is then $R = 0.46$, making the transmission coefficient 0.54. Our result for Poynting flux transmission in the torus corresponds with this prediction.

The increased Poynting flux transmission over previous results (from $\sim 20\%$ to 53%) is also important to the power budget of the Io-Jupiter interaction. The power input from the interaction (10^{12} W) is dissipated before reaching the ionosphere (10^{10} W of power in Io’s auroral footprint). With a low transmission ratio in the 20% range, most of the wave power at high latitude had to be entirely used for electron acceleration (Recall that only

10% of electron energy is converted to light in the ionosphere, and the rest is dissipated through ionospheric heating. The power budget demands that all the wave energy be used to accelerate electrons). An increase in power transmission reduces the needed efficiency for transferring wave power to precipitating electrons via inertial Alfvén waves.

The 1D model also shows the presence of right and left hand circularly polarized modes in the waves transmitted out of the torus. These are generally only present when the perturbation to the torus approaches λ_i . However, the Alfvénic perturbation is much larger than λ_i in the torus. These waves must be because λ_i is changing rapidly along the field as a consequence of the torus density gradient. The circularly polarized modes are not present near the peak of the torus, soon after being generated. Instead, dispersion of the wave occurs near the edge and outside of the torus.

The slower EMIC waves present will be affected by the Alfvén wave that is reflected back into the torus. The initial EMIC waves have an amplitude of 50 nT, a significant fraction of the Alfvén wave (~ 100 nT). The interaction of the EMIC waves and counter propagating Alfvén wave could contribute to turbulence within Io's wake and/or pitch angle scattering of trapped electrons.

The 2D eggbox simulation is set up to promote counter propagating waves at the ion inertial and ion kinetic scales. Counter propagating waves produces a turbulent cascade of wavelengths in the perpendicular components of the magnetic field. At Io, counter propagating waves are set up by a resonant cavity as a result of the density gradient in the plasma torus. Also, β is very small, so we do not see any turbulent heating of the ions. Only when β approaches unity does ion Landau damping occur, because the phase velocity of the wave is comparable to the thermal velocity of the ions (Recall that $\beta = v_{th}^2/v_A^2$, so when $\beta \sim 1$, then $v_a \sim v_{th}$).

Io's primary auroral footprint does not appear to involve counter propagating waves. However, *Jacobsen et al.* [2010] showed that non-linear Alfvén waves tend to reflect back on themselves within the torus, contributing to turbulence. We must address the limitations

of modeling turbulent cascade in just one or two dimensions. The electric field update subroutine is dependent on a double cross product of the \mathbf{k} vector with the electric field. Without both components of k_{\perp} , we have a poor understanding of the turbulent waves within the simulated domain. To resolve this, further study will focus on modeling a flux tube in 3D initialized with counter propagating waves.

2D Rayleigh-Taylor Instability

3.1 Introduction

The investigation of the Rayleigh-Taylor (RT) instability is for modeling radial transport of plasma in the giant magnetospheres. The instability generates Alfvén waves that propagate to higher latitudes, similar to Io’s interaction with Jupiter’s magnetosphere. The initial growth of the RT instability includes scale lengths that are shorter than the ion inertial length, λ_i . *Huba and Winske* [1998] previously compared the linear theory for the Hall MHD and hybrid cases. Conventional MHD theory is a fluid approximation that is restricted to systems where the length scale of grid resolution (L) is much greater than λ_i and the finite ion Larmor radius ($\rho_i = v_{th}/\Omega_i$). In the regime where $L \lesssim \rho_i$, the ion Larmor radius effects become significant, but can still be incorporated into the MHD model where ion and electron currents are treated separately (Hall effect). *Roberts and Taylor* [1962] discuss how these effects have a stabilizing effect on the RT instability, inhibiting growth. Figure 3.1 illustrates the divergence of growth rates for each of these MHD effects based on linear theory. For low mode number (m), where wavelengths are larger, The corrected growth rates closely match the conventional growth rate. Only for very high mode numbers, or large k_\perp , does the conventional growth rate diverge from MHD theory.

Huba and Winske [1998] also compare the MHD cases to the hybrid model by examining the RT instability at higher resolution, where $L < \lambda_i$. Hybrid simulations show the development of electric fields that cause $\mathbf{E} \times \mathbf{B}$ drifts in the plasma that are not present in the MHD case. The corrections made for the ion Larmor radius are also invalid at this scale, further necessitating a kinetic ion approach. The hybrid simulations are much noisier than the fluid cases (See Figure 3.2), and have developing turbulence that was not well resolved at very short wavelengths.

In this chapter we compare various hybrid simulations of the RT instability in 2D. In particular, we are interested in how seeded surface waves affect the growth rate of instability

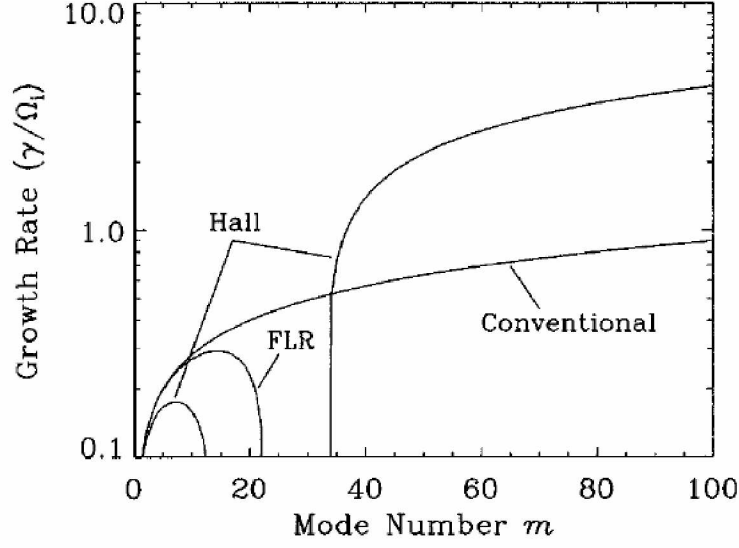


Figure 3.1: Growth of the Rayleigh-Taylor instability as a function of mode number m for conventional, Hall, and finite ion Larmor radius MHD (FLR) [Huba and Winske, 1998].

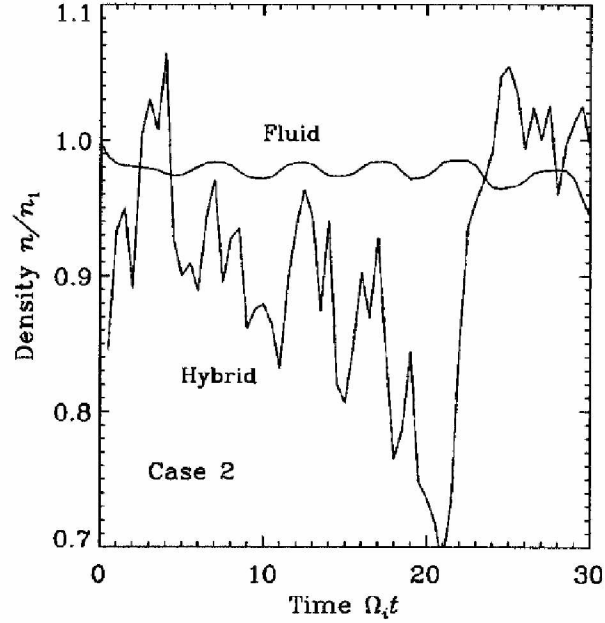


Figure 3.2: RT density change comparison: MHD vs. hybrid. The normalized density at the center of the boundary layer versus time for the fluid and hybrid simulations. The fluid case has a well behaved surface wave, while the hybrid case is less stable. Stochastic ion motion diverges from the ideal case and can cause larger density fluctuations in the hybrid simulation. Pressure balance is maintained for the duration of the simulation in 2D [Huba and Winske, 1998].

and how that compares with the predicted conventional growth rate from Equation 1.12. We need to confirm that growth rates in 2D match the linear theory before considering the 3D case, which includes parallel propagating modes. In addition, we seek to compare the evolution of mode number for cases with a seeded perturbation at the interface boundary, along with simulations where stochastic ion motion self-seeds the initial surface wave at the shortest resolved wavelength on the grid.

3.2 Hybrid Code Initialization

One challenging aspect of modeling the RT instability in the hybrid code is maintaining pressure balance. The ions have to be initialized with a density gradient and temperature profile so that the density transition region does not drift during the formation of the instability. The equation for equilibrium is given by

$$\frac{\partial}{\partial z} \left[p(z) + \frac{B_y(z)^2}{2\mu_0} \right] + \rho(z)g = 0 \quad (3.1)$$

where $p(z)$ is the pressure profile ($p(z)$ can be expressed as $n(z)T(z)$), $B_y(z)$ is the out-of-plane magnetic field component, $\rho(z)$ is the mass density profile, and g is the effective gravitational force (i.e., the centrifugal force in the non-inertial rest frame of the plasma in the magnetodisc). *Huba and Winske* [1998] maintain pressure balance by prescribing $n(z)$, $T(z)$, and g , and then calculating a gradient profile in B_y . In the local region of the magnetosphere that we will be simulating, the pressure balance is not maintained by a magnetic field gradient, so we will not be achieving pressure balance in the same fashion. Initializing a single population of ions requires a numerical integration to self-consistently solve for T and n such that the gradients in each satisfy the equilibrium condition. All the attempts to initialize the ions in such a way suffered from stability issues. Our solution involved initializing two ion populations, one with constant density and varying temperature, and the other vice versa. This better matches the conditions in the magnetodisc, where a hot

ion population is present. The dual ion population creates favorable equilibrium conditions for the onset of the RT instability in 2D, but creates issues with late runtimes in 3D. The full consequences of this approach are not fully understood and merit additional study.

We begin initialization of the RT hybrid code by specifying the coordinate system and boundary conditions. As shown in Figure A.1, ρ_1 and ρ_2 are differentiated along the z axis. The force of gravity acts along z . The y axis is out of plane, and the x axis runs along the boundary between ρ_1 and ρ_2 . Since y is out of plane, its corresponding boundary condition is necessarily periodic. Any ion that exceeds the limits of the y coordinate is returned at the opposite side of the domain with the exact same velocity to preserve momentum. The x axis is also periodic. The size of the x domain (L_x) will limit the number of possible RT wave modes, as well as the maximum size of the $m = 1$ wave mode.

The most complicated boundary is at the limits of the z axis. The density gradient presents a discontinuity should we attempt to make that boundary periodic as well. Instead, ions that cross the upper and lower boundaries are reintroduced somewhere at the exact same boundary they crossed. The ions are reinitialized with the same v_x and v_y with which they exited, but a reversed v_z , so they will move back into the domain. Their new x coordinate is randomized to maintain uniformity at the boundary. This boundary condition also tends to be reflecting with Neumann boundary conditions.

We attempt to replicate plasma conditions similar to the giant magnetodiscs. There is a trade off here, however. Attempting to reproduce the exact conditions would be too great a strain for computing resources. The limiting factor is comes from the growth rate, which is dependent on the effective gravity and density gradient. Too small a growth rate would take too long to replicate in a reasonable time. The best way to overcome this is to attempt to create a density gradient that has a much smaller length scale than the magnetodisc, and then adjust the temperature such that plasma- β is similar to that found in the magnetodisc. To start off, we set the background magnetic field out of plane at 5 nT, with no in plane components. The minimum plasma density is set to 0.05 cm^{-3} . The Atwood ratio ($\frac{\rho_1 - \rho_2}{\rho_1 + \rho_2}$) is

set to 0.5 for sufficient growth, so $\rho_1 = 3\rho_2$. The grid resolution is uniform and set to $0.5 \lambda_i$, where λ_i is the minimum value of the ion inertial length in the domain (This is c/ω_{pi} in the ρ_1 side of the domain, as c/ω_{pi} increases with decreasing density. The ion inertial length is therefore always resolved on the grid). The dimensions of the the simulation are $n_x = 109$ and $n_z = 459$. 60 particles per cell is sufficient for particle statistics and to avoid violating the Courant condition with the chosen time step $dt = 0.02 \Omega_i^{-1}$.

Due to our boundary condition at z , the gravity component cannot be uniform across z , lest ions on the boundary get trapped near the edges of the domain and we create a discontinuity. Instead, gravity must be kept uniform at the interface of ρ_1 and ρ_2 , and gradually decreased to zero near the boundary. To accomplish this, the gravity profile consists of two hyperbolic tangents as given by the following equation where g_0 is the maximum gravity, $0.2v_{th}^2/\lambda_i$, z_0 is the location of the RT boundary, L_0 is a length scale for the gravity transition region set to $15 \lambda_i$, and L_1 is the displacement of the transition region from the center of the domain ($55 \lambda_i$). See Figure 3.3 for the resulting profile.

$$g(z) = g_0 \left[\tanh \left(\frac{z - z_0 + L_1}{L_0} \right) - \tanh \left(\frac{z - z_0 - L_1}{L_0} \right) \right] \quad (3.2)$$

We now construct the density and temperature profiles to satisfy the equilibrium condition. To do this, we initialize two ion populations, one with a fixed density, $n_2 = \text{const}$, and the other with a fixed temperature, $v_{th} = \text{const}$. The following equation is for the z dependent gradient in n_1 , where n_2 is set to the minimum plasma density:

$$n_1(z) = n_2 \left[1 - \tanh \left(\frac{z - z_0}{L_0} \right) \right] \quad (3.3)$$

This places the density gradient in the center of the domain and gives n_1 a maximum value of $2n_2$. The addition of n_1 and n_2 is the total density profile (shown in Figure 3.3), and maintains the the needed mass density ratio ($\rho_1 = 3\rho_2$). The n_1 population is set to have a constant thermal velocity of $v_{th} = 50 \text{ km s}^{-1}$. The challenge now is to derive an expression

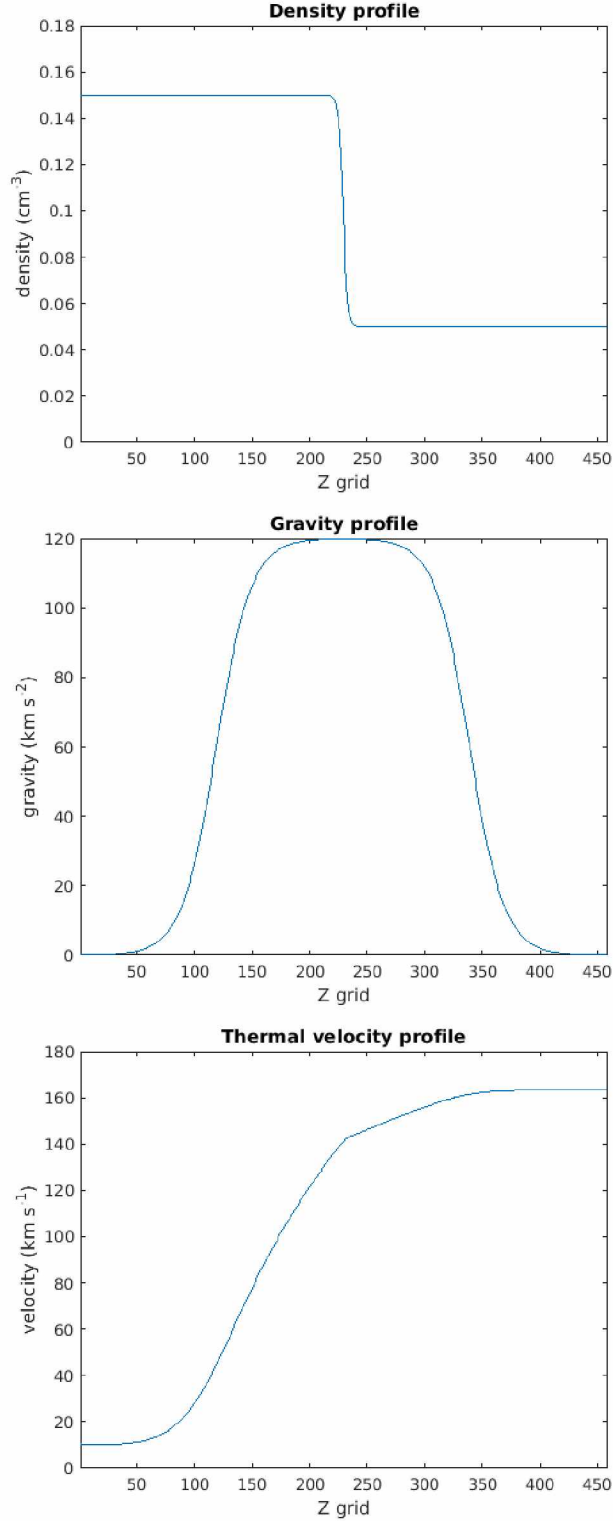


Figure 3.3: Initial parameters for the 2D RT instability. The density gradient is modeled using a hyperbolic tangent (See Eq. 3.3). The gravity profile is uniform across the domain, except at the z boundaries. It is also modeled using hyperbolic tangents (see Equation 3.2). The thermal velocity profile is derived from the the other two profiles (See Equation 3.10) so as to maintain pressure balance. This results in a profile that is monotonically increasing.

for the thermal velocity of the n_2 population. We start with Equation 3.1 and substitute some expressions. To simplify, the magnetic field does not vary with z , so we can leave it out. Let $p(z) = nT$ and $\rho(z) = mn(z)$. This leaves us with

$$\frac{\partial}{\partial z}(nT) = nmg \quad (3.4)$$

Another substitution is made using the definition of thermal velocity ($\frac{1}{2}nmv^2 = nT$) and the two ion populations, so that we obtain an equation for force balance:

$$\frac{\partial}{\partial z} \left(\frac{1}{2}n_1mv_1^2 + \frac{1}{2}n_2mv_2^2 \right) = (n_1 + n_2)mg \quad (3.5)$$

From this we derive an expression for v_2 .

$$v_1^2 \frac{\partial n_1}{\partial z} + n_2 \frac{\partial v_2^2}{\partial z} = 2(n_1 + n_2)g \quad (3.6)$$

$$\frac{\partial v_2^2}{\partial z} = -\frac{v_1^2}{n_2} \frac{\partial n_1}{\partial z} + 2 \frac{n_1 + n_2}{n_2} g \quad (3.7)$$

$$\int_0^z dv_2^2 = \int_0^z \left[-\frac{v_1^2}{n_2} \frac{\partial n_1}{\partial z} + 2 \frac{n_1 + n_2}{n_2} g \right] dz \quad (3.8)$$

$$v_2^2(z) - v_2^2(0) = -\frac{v_1^2}{n_2} \int_0^z dn_1 + 2 \int_0^z \left(\frac{n_1(z') + n_2}{n_2} \right) g(z') dz' \quad (3.9)$$

$$v_2(z) = \left[v_2^2(0) - \frac{v_1^2}{n_2} [n_1(z) - n_1(0)] + 2 \int_0^z \left(\frac{n_1(z') + n_2}{n_2} \right) g(z') dz' \right]^{1/2} \quad (3.10)$$

The thermal velocity for the constant density population is now a function of the density gradient, gravity function, and some initial thermal velocity (set to the minimum thermal velocity v_{1th}). The integral here does not have an analytic solution for the chosen density and gravity functions, but can be found numerically by summing over the density gradient times gravity across the grid. The resulting temperature profile is shown in Figure 3.3. Ion velocities are then initialized using v_{th} and Equation C.4. The resulting pressure gradient is

shown in Figure 3.4.

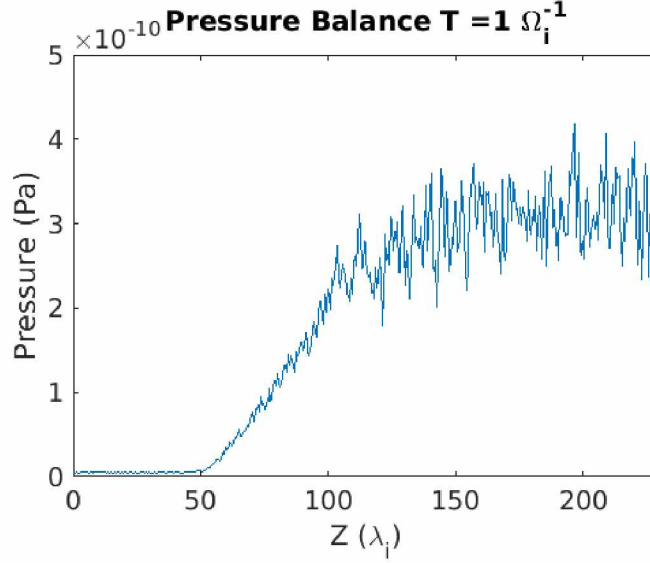


Figure 3.4: Initialized pressure profile along z . As z increases, plasma pressure must increase to balance the weight of the plasma on top of it. Noise is introduced due to the random initialization of the ion velocities (See Eq. C.4).

To maintain a standard number of ions in each grid cell, and reduce the number of simulated ions, we adjust the weight function w for each ion in the n_1 population, rather than just tripling the number of ions in their part of the domain. This results in a z dependent weighting function:

$$w = \frac{N_{total}}{L_x L_y L_z n_1(z)} \quad (3.11)$$

where N_{total} is the total number of ions, and L_x , L_y , and L_z are the lengths of each respective domain.

With these initialization parameters, we can construct a profile of the plasma- β along z , based on the ratio of the pressure to the magnetic field strength ($\beta = \frac{\rho_i v_{th}^2}{B^2/\mu_0}$, see Figure 3.5). Plasma- β is also equivalent to ρ_i^2/λ_i^2 (Equation 1.15), so $\rho_i \sim 3.4 \lambda_i$ at $z = z_0$. In the high density section of the domain, the plasma is cool and $\beta < 1$, so the grid spacing is greater than the ion gyroradius, and ion kinetic effects are not resolved. For $z > 75\lambda_i$, plasma pressure is increased enough such that $\beta > 1$, and ion gyromotion is fully resolved. The boundary interface is $110\lambda_i < z < 120\lambda_i$, where $\beta > 10$, so ion kinetic motion is reflected on

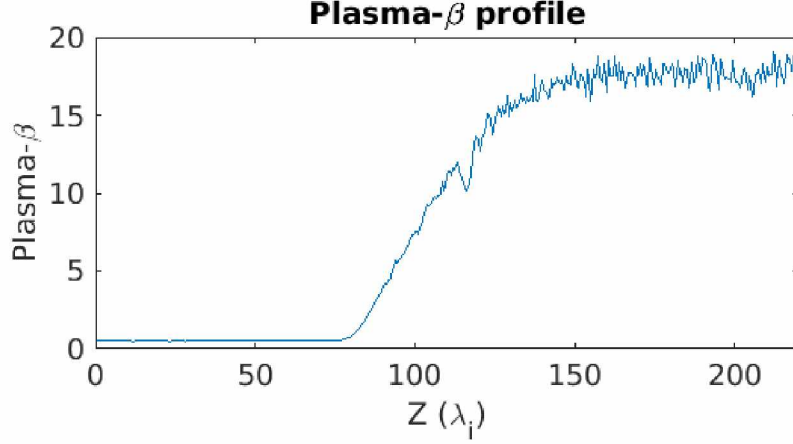


Figure 3.5: Plasma- β profile of the 2D RT instability across z based on the ratio of the plasma pressure ($\frac{1}{2}\rho_i v_{th}^2$) to the magnetic pressure (B^2/μ_0) averaged across x . The grid resolution is $0.5 \lambda_i$, so where $\sqrt{\beta} > 0.5$, the ion gyroradius is also resolved. For $z > 75\lambda_i$, β is large enough to resolve ion gyromotion, which is important near the interface boundary.

the grid in the most important region of the simulation.

In contrast to a fluid simulation, there is no need to initialize a surface wave into the density gradient boundary. Unstable equilibrium is automatically disrupted by the random initialization of ion location and velocities. Self-seeded runs, however, require a longer runtime, as it can take a while for a coherent surface wave to register on the grid. In order to investigate and compare the behavior of the instability at specific wave modes, it is necessary to seed the perturbation with a specific wavelength. This is done by adjusting the ion velocity initialization near the density gradient boundary. Starting with the initialization of a Maxwellian distribution (see Equation C.4), we add another term that is x dependent:

$$v(x, z) = v_{th}(z) \sqrt{-\ln(r_1) \cos(\pi r_2)} + v_{th}(z) \cos\left(\frac{2\pi m x}{L_x}\right) / \cosh^2\left(\frac{z - z_0}{L_1}\right) \quad (3.12)$$

where m is the selected wave mode, L_1 is a length scale set to $4 \lambda_i$, and $r_{1,2}$ are random numbers between zero and one (stochastic ion initialization). The hyperbolic cosine keeps the perturbation near the relevant region to allow for variation along y .

3.3 Growth Rates

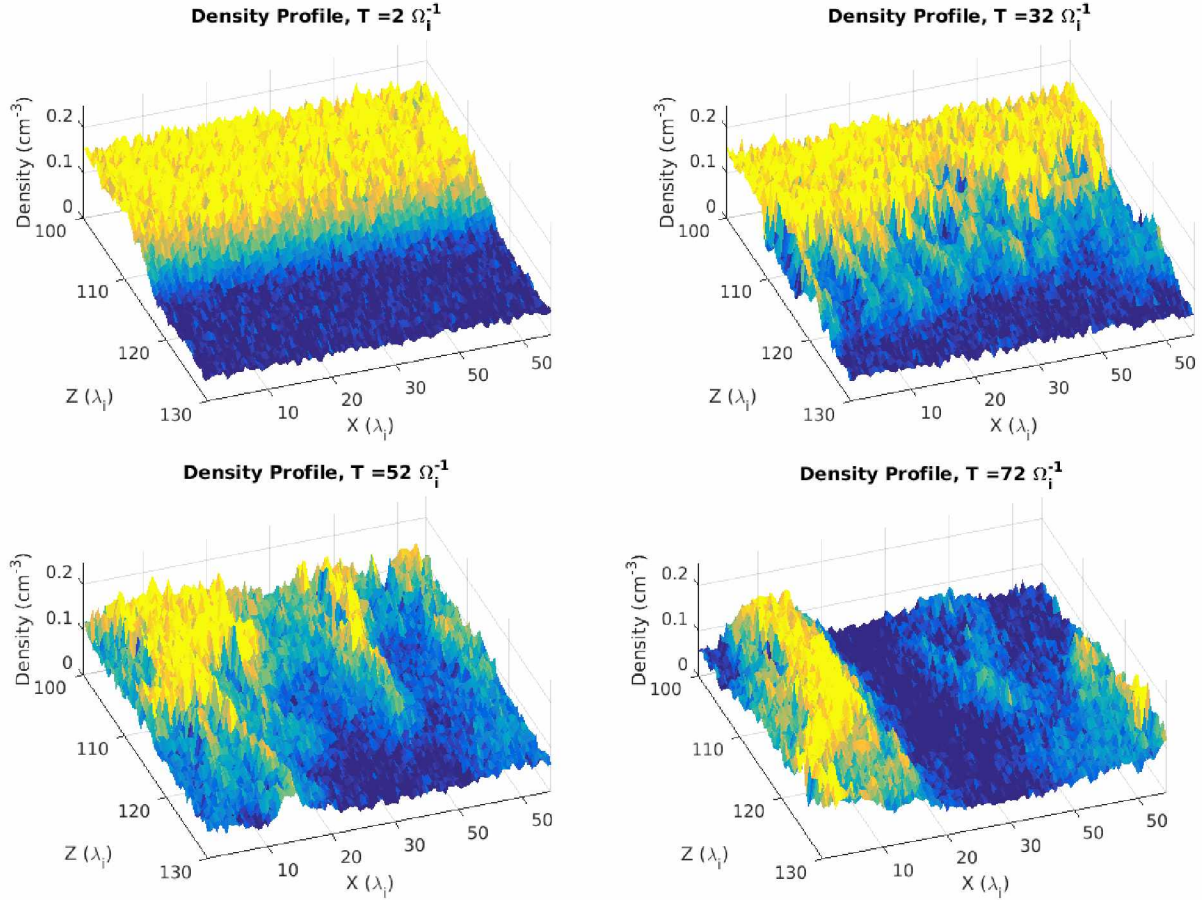


Figure 3.6: Density profile of a self-seeding RT instability. Small surface waves begin at the size of the grid cells. The beginning of the simulation has a high m number. Later the waves coalesce into an $m = 2$ mode that fills the domain. Growth rate depends on the density gradient, gravity, wave number, and the in-plane magnetic field, as given by Equation 1.12.

Examination of the self-seeded run proceeds. In Figure 3.6 we plot the density gradient of the instability as a surface plot. The minimum size of the surface waves begins at the scale of the grid (about $0.5 \lambda_i$), resulting in a high initial number of wave modes (high m number). We can compare the rate of growth with the linear theory using Equation 1.12, simplified for the 2D case. There are no wave modes parallel to the magnetic field, so we can eliminate the second term. We can also substitute k_\perp with $m\pi/L_x$. Equation 1.12 is

thus simplified to

$$\gamma = \sqrt{\frac{m\pi g A}{L_x}} \quad (3.13)$$

where A is the Atwood ratio. The higher m is an indicator of a higher growth rate. With time the waves coalesce into larger structures until the $m = 1$ mode is reached.

Figure 3.7 also illustrates the same growth and coalescence. Here we examine the growth and transport with mixing ratios. Each ion is tagged with a zero if $z < z_0$ and a one if $z > z_0$. Mixing in each grid cell is determined by the average value of the of all the ions interior to it. Ion gyromotion results in automatic mixing near the interface boundary. However, transport only occurs through growth of the instability.

In contrast, we examine the growth and and transport of simulations with specific wave modes, ranging from $m = 1$ to $m = 12$. Figure 3.8 shows the same examination of the mixing ratio, but with an $m = 3$ mode. The initial velocity perturbation results an immediate formation of a surface wave that forms much more rapidly than the unseeded case. One benefit of this approach is that growth rate can be more directly compared to the m number, as there is no coalescence of the surface wave for the seeded runs. As can be seen in the figure, growth of the instability has substantially slowed at about half the runtime. After that, we mostly see diffusion of the finger structures. It could be that the physical finger structures are larger than the domain and are still coalescing.

We analyze the growth rate by comparing the rate of change of bulk v_z on the grid. We do this by finding the maximum value of v_z on the grid within 100 grid cells of the interface boundary. We limit the range of investigation to reduce the incidence of noise from side of the domain that has warmer plasma. The low density combined with the hotter plasma increases the amount of fluctuation of v on the grid when compared to the other side with cooler, denser plasma. The growth rate is the coefficient for the real part for the plane wave solution, i.e.

$$v_z(x, t) = v_z(x) \exp[-i(\omega + i\gamma)t]. \quad (3.14)$$

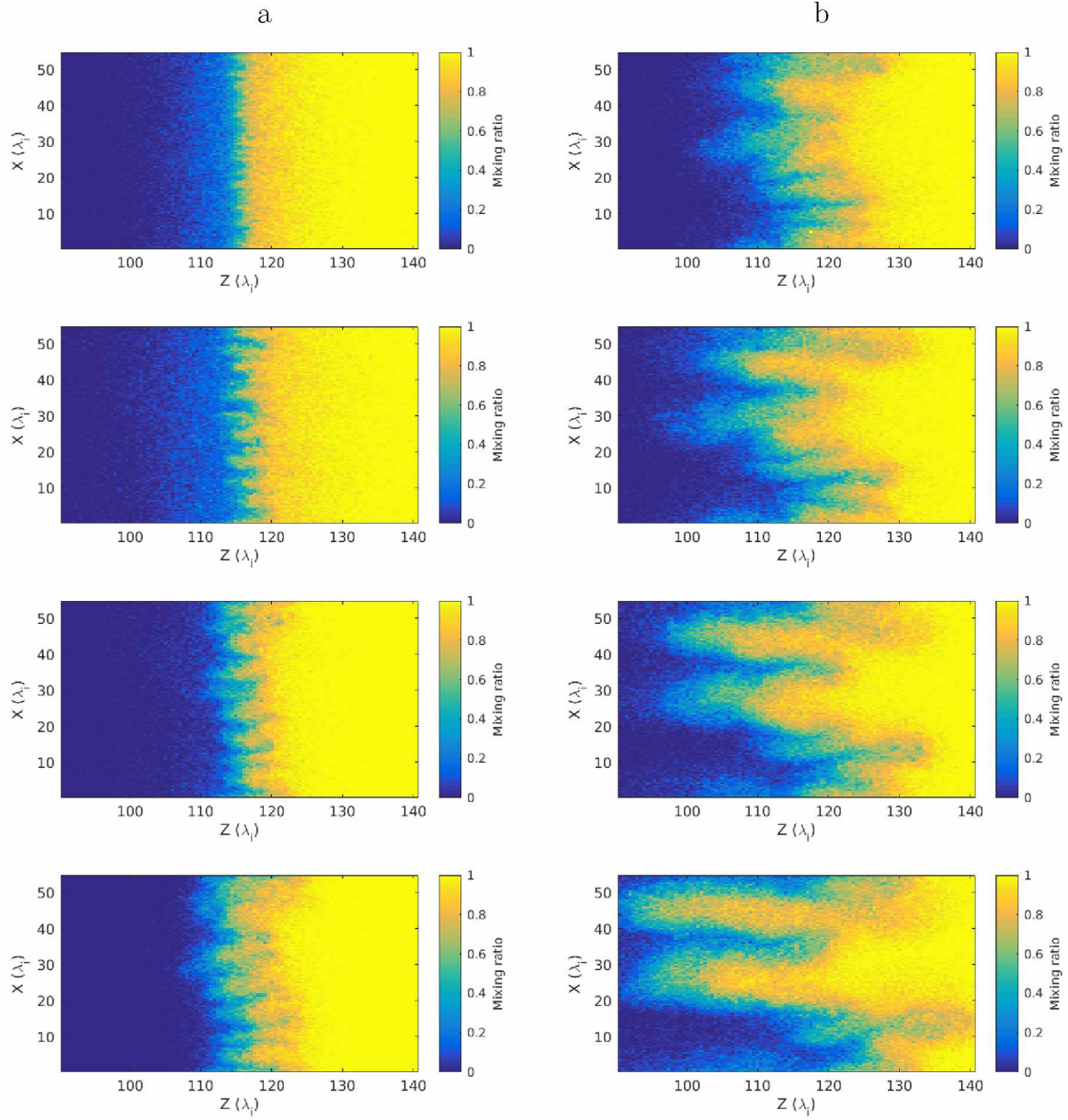


Figure 3.7: Growth of a self-seeded RT instability by mixing ratio. Each ion is tagged with a one or zero depending on which side of the boundary it is on during initialization. Each frame shows the weight of mixing for each grid cell depending on the number of each tagged ion in the cell. Each frame is separated by $8 \Omega_i^{-1}$.

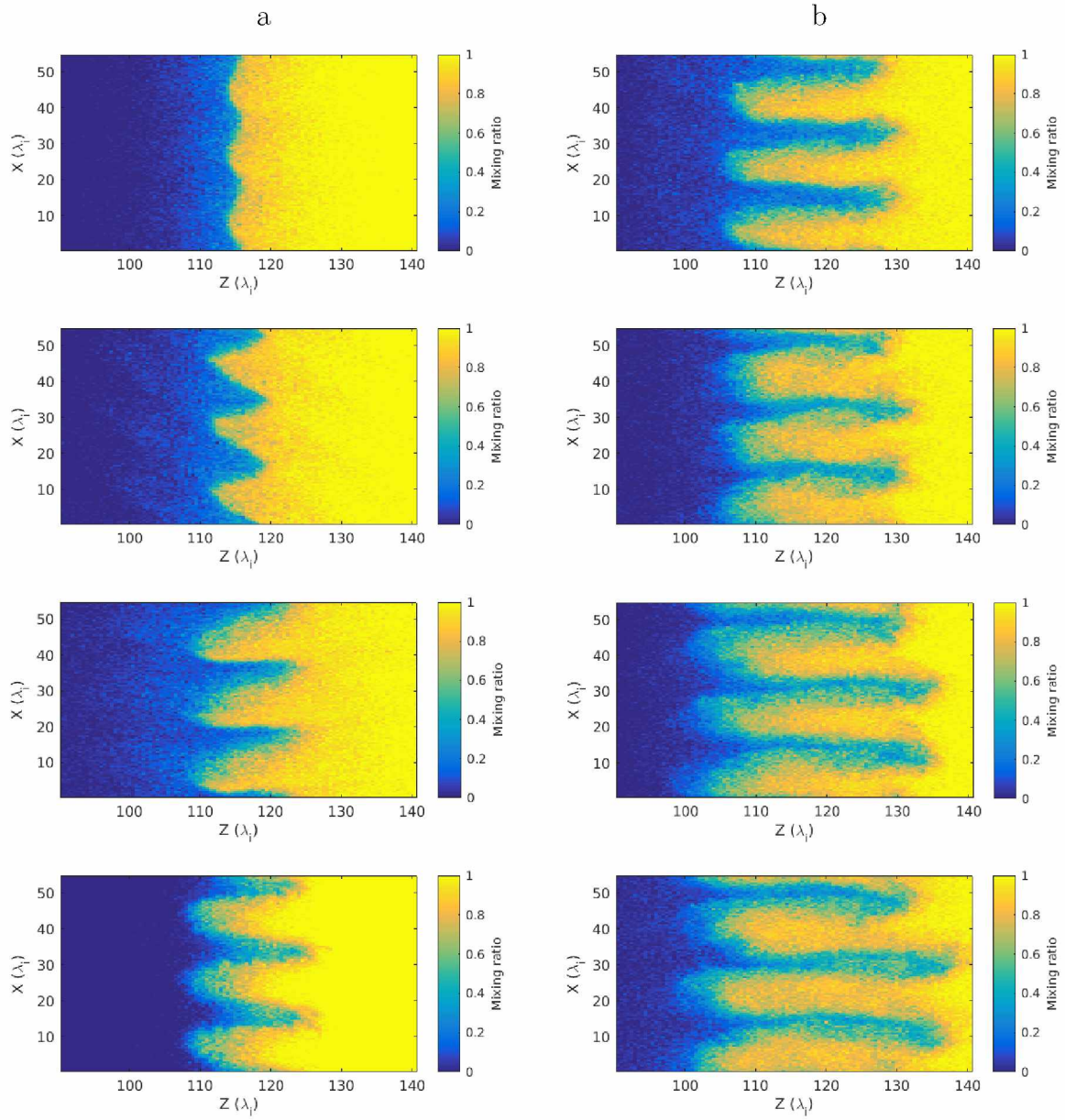


Figure 3.8: Growth of a seeded $m = 3$ RT instability by mixing ratio. Each ion is tagged with a one or zero depending on which side of the boundary it is on during initialization. Each frame shows the weight of mixing for each grid cells depending on the number of each tagged ion in the cell. For seeded runs, there is no coalescence. Each frame is separated by $8 \Omega_i^{-1}$.

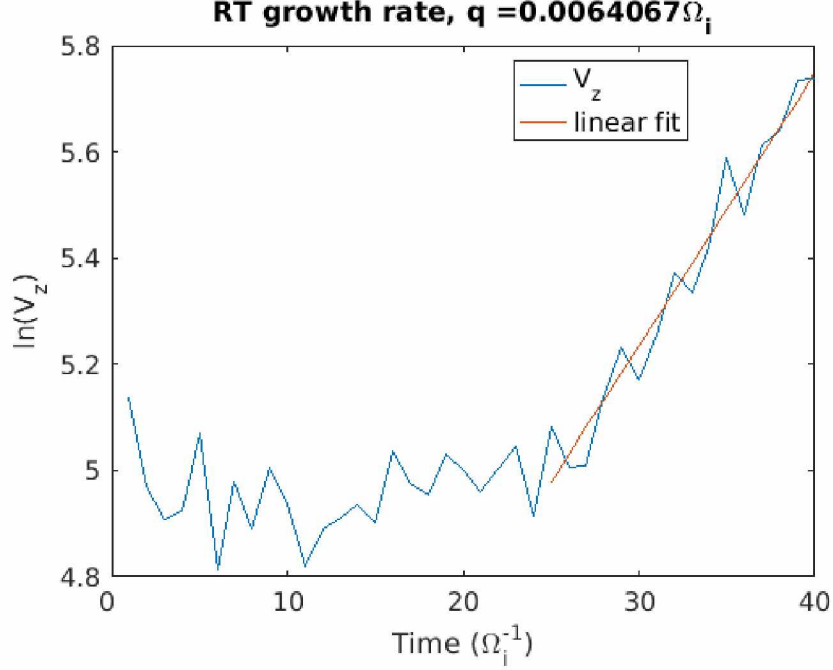


Figure 3.9: Growth rate of the RT instability for the unseeded case. Growth rate is found using the maximum bulk v_z on the grid near the boundary layer. The slope of the natural logarithm of v_z is equivalent to the growth rate.

γ can then be estimated by fitting a slope to the natural logarithm of the change of v_z with time, which we then normalize to the ion gyrofrequency. Figure 3.9 shows an example of a linear fit for the unseeded RT instability, which has no observable growth until $\sim 25 \Omega_i^{-1}$.

In Figure 3.10 we plot the growth rates obtained from seeded simulation runs as a function of mode number and compare it to the theoretical growth rate obtained from Equation 3.13. The growth rates are significantly less than the ion gyrofrequency. For high m numbers, the results are in good agreement with the linear theory, though they show consistently lower numbers. This is due to the fact that the Equation 3.13 describes an upper limit to the growth rate, and neglects that other factors, such as numerical diffusion, can hamper the growth rate.

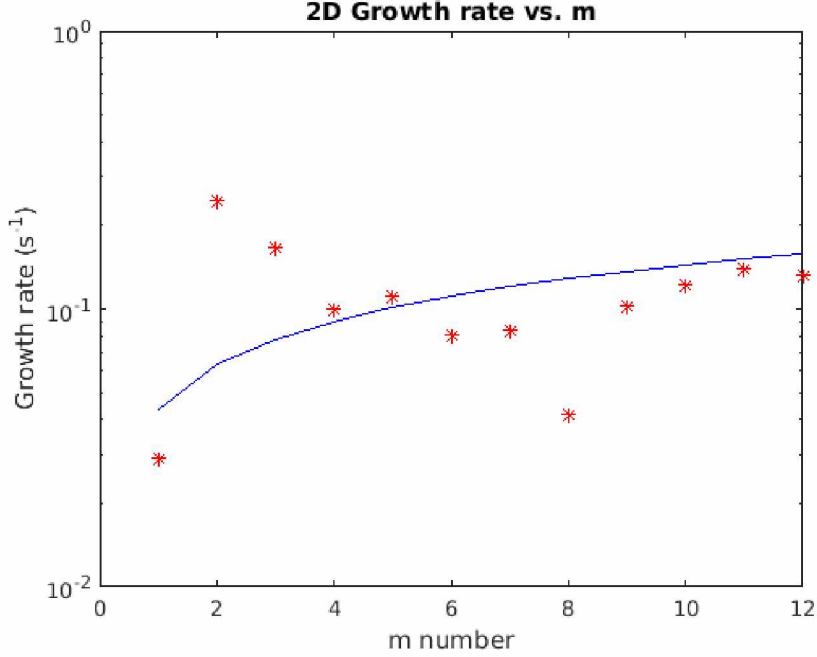


Figure 3.10: Comparison of growth rates based on wave number. The blue line represents the analytical prediction based on Equation 3.13.

3.4 Dispersion Analysis

Wave mode coalescence and dispersion can also be analyzed through frequency analysis. For each seeded simulation we conduct a spatial fast Fourier transform of the various quantities along x at $z = z_0$ (the interface boundary). Pressure balance is maintained across the boundary, so there is little motion of the interaction region. We repeat the Fourier transform for each output time step so that we see the evolution of the wave modes with time.

Figure 3.11 plots the power spectrum of the density profile versus time for the seeded runs. They correlate very well with what was observed before in Figure 3.8: that there is no coalescence of the waves into lower modes, and wave power remains concentrated in the seeded wave mode. This also remains true for analysis of other quantities, including mixing ratios and temperature. One interesting artifact, however, is that there are harmonics present at multiples of the initial wave mode.

Wave analysis for the self-seeded run is shown in Figure 3.12. Before $10 \Omega_i^{-1}$, there is

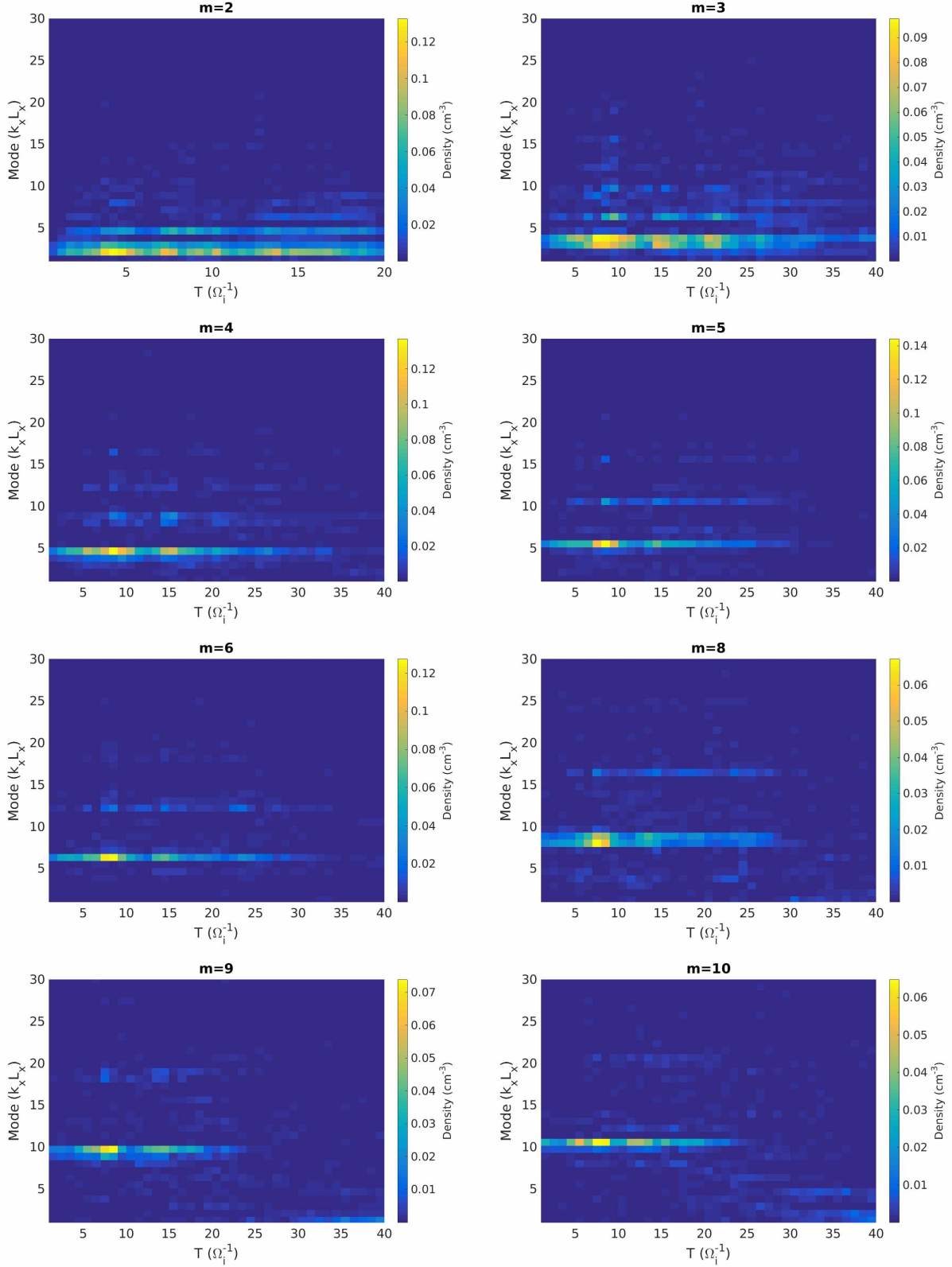


Figure 3.11: Dispersion of specific wave modes. A spatial Fourier transform is applied across the density boundary interface. It is repeated each time step to get the change in m over time.

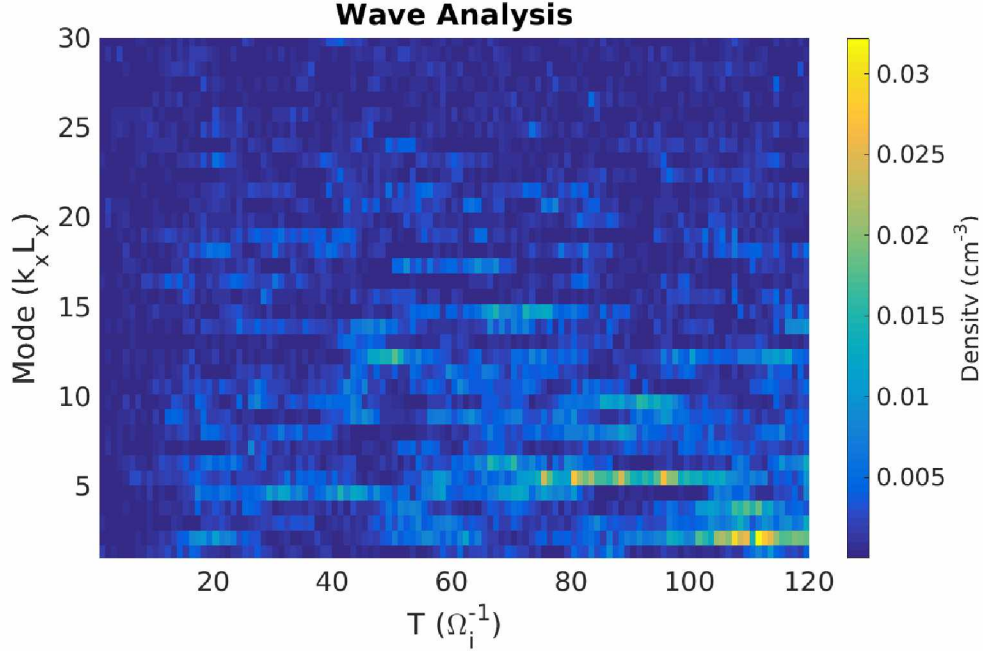


Figure 3.12: Wave mode coalescence. For an unseeded simulation, wave power is distributed across the spectrum. At about $T = 80 \Omega_i^{-1}$, most of the wave power is in the $m = 6$ mode. By $T = 100 \Omega_i^{-1}$, the $m = 2$ mode is dominant.

no wave formation across the boundary, and all we see is noise. After about $20 \Omega_i^{-1}$, the wave formation reaches the grid scale, and wave power begins to register. Power is evenly distributed between many wave modes. After $\sim 60 \Omega_i^{-1}$, wave power decreases in the higher modes as the small waves coalesce. After $80 \Omega_i^{-1}$, wave power settles at the $m = 6$ mode. By $100 \Omega_i^{-1}$, the instability has finally coalesced into the $m = 2$ mode.

3.5 Conclusion

Growth rates for seeded runs match well with the theory for maximum growth rate for the RT instability for high m numbers. The growth rate does not account for k_{\parallel} , as the magnetic field is initialized out of plane. One way to include the $\mathbf{k} \cdot \mathbf{B}$ term from the growth rate equation would be to initialize an in-plane component to the magnetic field. This would have the effect of stabilizing the surface waves. However, since we are interested in propagation along the magnetic field line, we will need to expand the simulation to three dimensions. This will also capture both components of k_{\perp} , which is important when modeling

turbulence at ion kinetic scales.

It is also interesting to discover that the seeded runs have very little change in m with time, compared to the self-seeded case where wave modes coalesce. This is also a problem in fluid simulations of the RT instability, which requires a perturbation at the interface boundary, and do not exhibit changes in m number. In the self-seeded run, there is a change in observed wavenumbers because mixing is better promoted by v_{th} with no extra v_z perturbation. It is also interesting to consider that the coalescence is an inverse turbulent cascade, where energy is injected at small wavelengths, and is then transferred to larger wavelengths. Slower growing modes (with a small k_{\perp}) with larger amplitude eventually envelop the smaller surface waves (large k_{\perp}), completing the inverse cascade. In addition, nothing limits the growth of larger wavelengths except for the size of the simulation domain. No matter our choice for the size of the x domain, the instability will eventually cascade to an $m = 1$ mode. The large perturbations in the magnetic field in Saturn's magnetodisc (Figure 1.9) have wavelengths that are $\sim 10 \lambda_i$, so there is a limiting factor to the size of k_{\perp} . We will need to investigate in 3D in order to include a limiting k_{\parallel} term in the growth rate.

Figure 1.12 shows the power density spectrum vs. frequency at Saturn. The lower figure shows that there is a larger heating rate density in the dissipation range of the turbulent cascade than in the inertial range. The power spectrum shows a small bump in power density at the ion gyrofrequency. Perhaps energy is being injected at the ion kinetic scale, and then transferred to both larger and smaller wavelengths in a turbulent cascade. The hybrid simulation shows that this is plausible for the RT instability. Since Saturn's magnetodisc is also susceptible to the RT instability, it is not necessary that transport is initiated at large scale and then cascade to small scale. Instead, surface waves at small scale can cascade to large wavelengths to facilitate transport.

3D Rayleigh-Taylor Instability

4.1 Introduction

Located in the inner magnetospheres of Jupiter and Saturn are the primary sources of plasma for the magnetodiscs: Io and Enceladus. The ionization of Io's atmosphere produces a ton per second of plasma that spreads out into the magnetosphere [Delamere *et al.*, 2003]. As the plasma convects away from Jupiter, conservation of angular momentum would normally make it rotate more slowly, except that it is coupled to the Jovian flywheel by the planet's strong magnetic field. The outward-moving magnetospheric plasma stretches the magnetic field and bends it backwards. The resulting $\mathbf{J} \times \mathbf{B}$ force creates an electrical current that flows along the magnetic field to keep the the plasma corotating with the planet. At some point, usually about $L = 20$ for Jupiter, the stresses of keeping the plasma corotating becomes too much: there is insufficient electrical conductivity in the ionosphere to complete the necessary currents. Slippage of the magnetic field at high latitudes provide the parallel electric field necessary to accelerate superthermal electrons enough that they precipitate into the atmosphere. The resulting aurora is therefore a signature of the magnetosphere's failure to keep the plasmadisc in strict corotation (See Figure 4.1). At Saturn, only $\sim 50 \text{ kg s}^{-1}$ of plasma is transported radially outward [Achilleos *et al.*, 2014; Fleshman *et al.*, 2013]. IR and UV aurora in Saturn's lower latitudes have been shown to correspond to this plasma motion [Stallard *et al.*, 2008; Grodent *et al.*, 2010]. The source of auroral emissions is still disputed, however, in the case of the giant magnetospheres. It is an open question whether Jupiter has an open magnetosphere, and if the solar wind is the source for more poleward emission. At Earth, solar wind is the primary driver of magnetospheric transport and auroral activity, but since Jupiter is driven more by internal plasma sources, sources for polar auroral emissions are unclear.

Earlier attempts to model the global transport of plasma have been attempted. These have primarily consisted of magnetohydrodynamic (MHD) and multi-fluid simulations. MHD

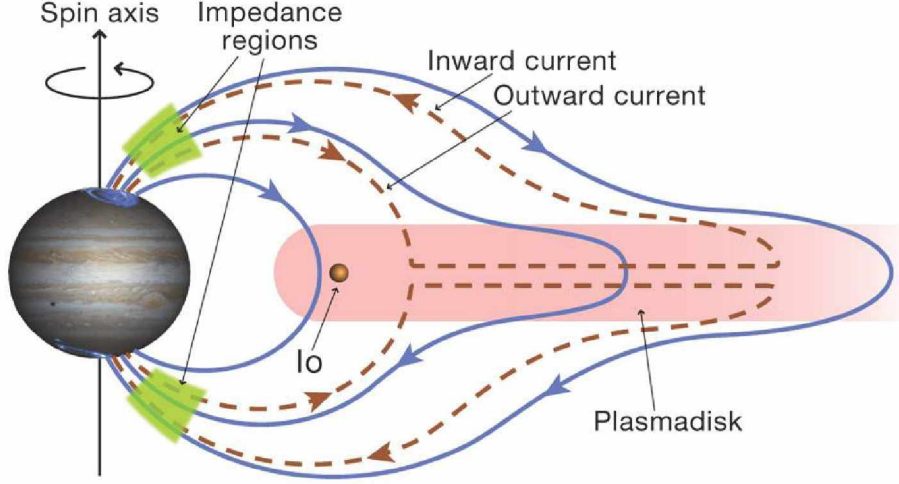


Figure 4.1: Illustration of Jupiter magnetosphere-ionosphere coupling [Cowley and Bunce, 2001].

models require a set of inner boundary conditions to represent ionospheric conductance and set up a mass loading rate [Chané *et al.*, 2011; Kidder *et al.*, 2009; Winglee *et al.*, 2013]. Liu and Hill [2012] use the Rice Convection Model to simulate radial transport of plasma (Figure 4.2). This approach also requires a model for the magnetic field and ionospheric conductance, but requires conservation of the first and second adiabatic invariants, and relies on equipotential magnetic fields.

Ma *et al.* [2016] examine a local region of the magnetodisc extended to higher latitudes using a 3D MHD model, including evidence that RT instabilities in the magnetodisc cause a twist in the magnetic field lines at high latitude. Anti-parallel in-plane components of the magnetic field are brought together and reconnect, decoupling plasma from the magnetosphere, illustrating the importance of a parallel electric field (See Figure 4.3). This is very different from models where entire flux tubes are interchanged and close in the ionosphere (e.g., the Rice Convection model). This allows transport without a large change in field configuration.

Caudal [1986] uses a self-consistent axisymmetric model for Jupiter’s rapidly rotating magnetosphere in which both the pressure gradient and the centrifugal force balance the Lorentz force. Using empirical plasma profiles from Thomsen *et al.* [2010], Ma [2018] applied

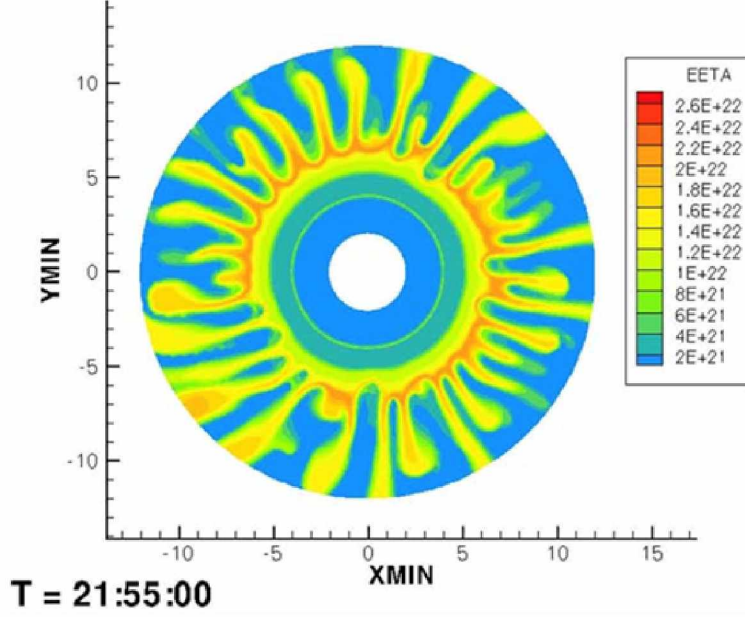


Figure 4.2: Global MHD simulation of Saturn's inner magnetosphere using the Rice Convection Model. Plasma pressure acts in the same direction of the centrifugal force and drives radial plasma convection [Liu and Hill, 2012].

the model to the conditions present at Saturn (See Figure 4.4). As expected, the flux tube entropy increases with radial distance, indicating stability of the magnetodisc. Flux tube interchange can change the local profile. In the limiting case that interchange involves the entire flux tube, higher entropy would be transported inward, leading to instability. *Ma* [2018] showed that this destabilizing feedback can be resolved by magnetic reconnection somewhere along the field line, preserving a stable flux tube entropy profile (i.e. partial flux tube interchange).

All the global models are limited in detail as a result of scale and limited computational resources. Fluid models are limited in that they do not resolve individual ion motion, where adiabatic invariants may not be conserved, or ion drifts are not present on the grid. Turbulent heating at ion scales are also not resolved. We present a more local simulation of the magnetodisc using the hybrid code in an attempt to clarify the effect of ion scale motion on the formation of the RT instability and any inverse turbulent cascade. To include the effects of all perpendicular and parallel propagating wave modes, we model the formation

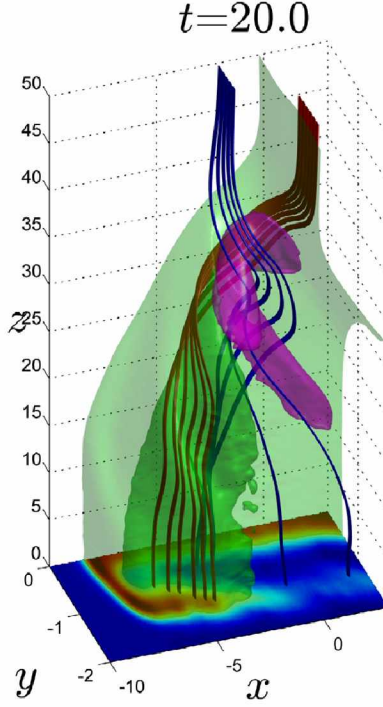


Figure 4.3: MHD RT instability. At large scales, RT instabilities causes magnetic field lines to twist at higher latitude, where magnetic reconnection takes place, decoupling the plasma from the magnetodisc [Ma *et al.*, 2016].

of the RT instability in three dimensions. Only a small section of the middle magnetodisc is modeled (at Saturn, this would correspond to $L = 15$). The density scale height of the torus acts as a resonant cavity, trapping the majority of parallel propagating waves within the simulation domain. Figure 1.19 illustrates the modeled section of the magnetosphere.

4.2 Hybrid Code Initialization

Initialization of the 3D hybrid simulation is based off of the earlier code setup detailed in section 3.2. The xz domain remains the same, with $n_x = 109$ and $n_z = 459$. We now add in a domain of y to eliminate an ignorable direction and allow for the propagation of waves parallel to the magnetic field ($n_y = 87$). Ion gyromotion remains limited to the xz plane, and motion along y is primarily thermal, lessening the need for the same resolution in y . Instead it is best to maximize the value of L_y so that the k_{\parallel} is minimized initially, and there

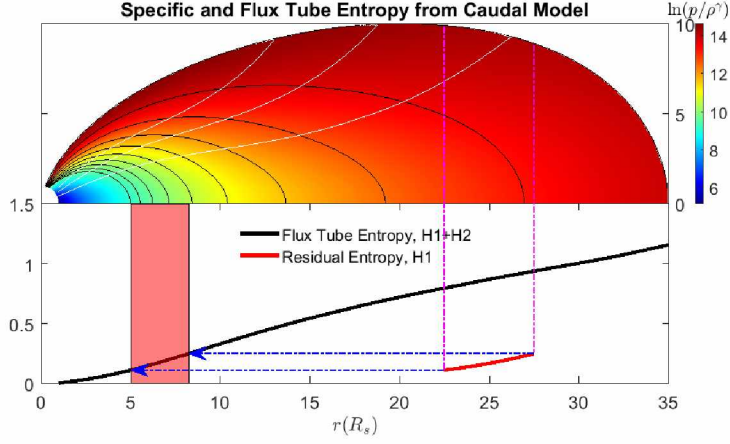


Figure 4.4: Specific and flux tube entropy at Saturn. Equilibrium configuration of Saturn's magnetodisc following the Caudal model using profile of plasma density from *Thomsen et al.* [2010]. The magnetic field lines are shown in black, and the color scale represents the flux tube entropy at the appropriate radial distance and latitude.

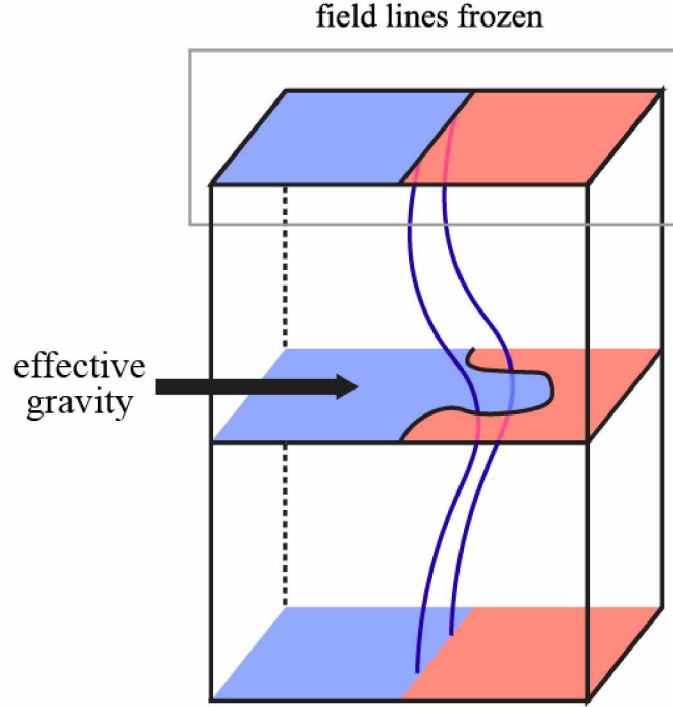


Figure 4.5: 3D RT simulated domain with fixed field lines. The simulated region of the magnetodisc is shown in Figure 1.8, which acts as a resonant cavity. Magnetic field lines are fixed at the top and bottom by boundaries. A surface wave is seeded at the center of the domain ($y = y_0 = L_y/2$). Growth of the instability bends the magnetic field lines.

is sufficient time for the instability to form and grow before any wave reflection from the boundary becomes significant. We will be examining two different scenarios: one where the boundary conditions at y are reflective, and one where y has periodic boundary conditions. Grid spacing along y is set to $1.5 \lambda_i$ (recall that λ_i is the minimum value of c/ω_{pi} in the domain). 60 ions are initialized per cell, and the weighting function from Equation 3.11 is still applied to them.

Since the goal is to set up a resonant cavity in the first scenario, the y boundaries are set to be reflective. Therefore, the value of the electric field is set to zero (i.e. infinitely conducting) in the grid cells at the boundary. The derivative of the electric field is set also set to zero in the two grid cells adjacent to the boundary. Parallel propagating waves can cause surface waves to form at the y boundary, unless the ions are treated more aggressively. The objective here is to prevent any plasma or momentum transfer at the y boundary, and thus prevent the formation of surface waves there. Individual ion velocities near the boundary are reset to their initial thermal gyromotion using a Monte Carlo selection technique. Each time step a random number r , where $0 < r < 1$ is generated for each ion. If r is less than the following Maxwellian relationship, the ion's velocity is reset to its initial value.

$$\begin{aligned} r &< \exp \left[- \left(\frac{y - L_Y}{6 \, dy} \right)^2 \right], \text{ or} \\ r &< \exp \left[- \left(\frac{y}{6 \, dy} \right)^2 \right] \end{aligned} \tag{4.1}$$

This means that ions in the boundary grid cells are certain to be reset, which prevents changes in bulk velocity and the formation of surface waves. Ions further from the y boundary have a lower chance of having their velocity reset, and ions near the center of the domain are unaffected by the boundary conditions.

For seeded perturbations, the surface wave is restricted to the center of the y domain ($y = y_0 = L_y/2$). Ions near the interface boundary are set similar to Equation 3.12, modified

to confine the perturbation in y :

$$v(x, z) = v_{th}(z) \sqrt{-\ln(r_1) \cos(\pi r_2)} + v_{th}(z) \frac{\cos\left(\frac{2\pi m x}{L_x}\right)}{\cosh^2\left(\frac{z-z_0}{8dz}\right) \cosh^2\left(\frac{y-y_0}{8dy}\right)} \quad (4.2)$$

Recall that this is the initialization for individual ions with a modification to a Maxwellian distribution. The first term represents the initialization of the Maxwellian (where $r_{1,2}$ are randomly generated numbers from zero to one to model stochastic ion initialization), and the second term provides a surface wave perturbation near the boundary interface.

Profiles of n , g and v_{th} are the same as the 2D case. We only change the ambient magnetic field strength from 5 nT to 20 nT, which helps promote stability in the initial formation of the surface wave, but lowers the maximum value of plasma- β . Maintaining pressure balance for the duration of the simulation is difficult for runs with a seeded perturbation. One such difficulty is maintaining resolution of ion motion along z . The grid scaling is meant to primarily resolve ion motion near the interface boundary, and is sufficient for the temperature of the ions in that area ($\rho_i \sim 1.4\lambda_i$ at $z = z_0$, see Table 4.1 for initialization parameters). However, near the $z = 0$ boundary ions are too cold to resolve some of the gyromotion, and we could be missing some balancing current. Figure 4.6 shows a profile of the plasma- β at $y = y_0$, where a transition occurs from $\beta < 1$ to $\beta > 1$. Additionally, fast bulk velocities and an increase in the in-plane magnetic field near $y = y_0, z = z_0$ create additional currents that can disrupt pressure balance.

Figure 4.7 shows the evolution of the thermal pressure of the domain. A sudden increase in pressure forms at the interface boundary at $T = 15 \Omega_i^{-1}$. The discontinuity increases throughout the rest of the run. A result of this is stagnant growth of the instability by $T = 50 \Omega_i^{-1}$. Followed is a severe collapse in density on the ρ_1 side of the instability, leaving behind dense plasmoids near where the interface boundary used to be.

Comparison of the pressure with scaled values for density and temperature are shown in Figure 4.8. Here the density collapse is made more apparent, combined with density peaks

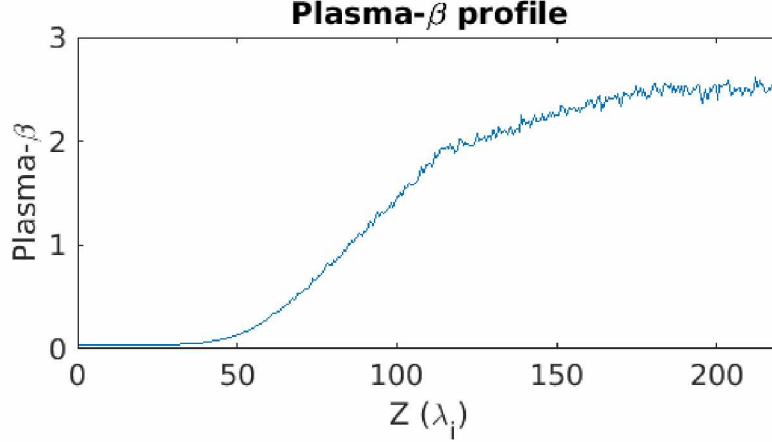


Figure 4.6: Plasma- β profile of the 3D RT instability at $y = y_0$, averaged across x . The grid spacing is $0.5 \lambda_i$, so for the region where $\sqrt{\beta} < 0.5$, the grid resolution is less than ρ_i . As a result, ion motion near the transition region of $\beta = 0.25$ is not fully resolved. Past $z = 75\lambda_i$, β is large enough to fully resolve the ion gyromotion.

near $z = z_0$. We would instead expect that average pressure, temperature, and density profiles remain relatively unchanged from their initial states. It is clear that results past the initial growth phase are tainted by this pressure catastrophe. As such, we will limit our investigation of these simulations to their early growth stages and initial wave propagation.

It is unclear to us why pressure balance is so easily disrupted. The 2D RT simulations did not have this issue, so the imbalance is a 3D effect. Test cases where velocity perturbations are not seeded on the boundary are not subject to the density collapse, but are also too stable for plasma transport. Varying initial parameters such as the density gradient and g_0 does not resolve the issue. We suggest that it may be a combination of gravity and initial velocity perturbation. Prior test runs produced a bulk v_z that causes plasma to build up near the area where gravity is deactivated on the low β side of the simulation. Velocity perturbation of the ions might have been too great relative to stochastic motion, and caused an imbalance near the gravity transition region. The choice of a dual ion population is also likely to be a factor. Only a fraction of the ions have a thermal velocity that contribute to the pressure required for balance.

The second scenario we will investigate involves simplifying the y boundary to be periodic.

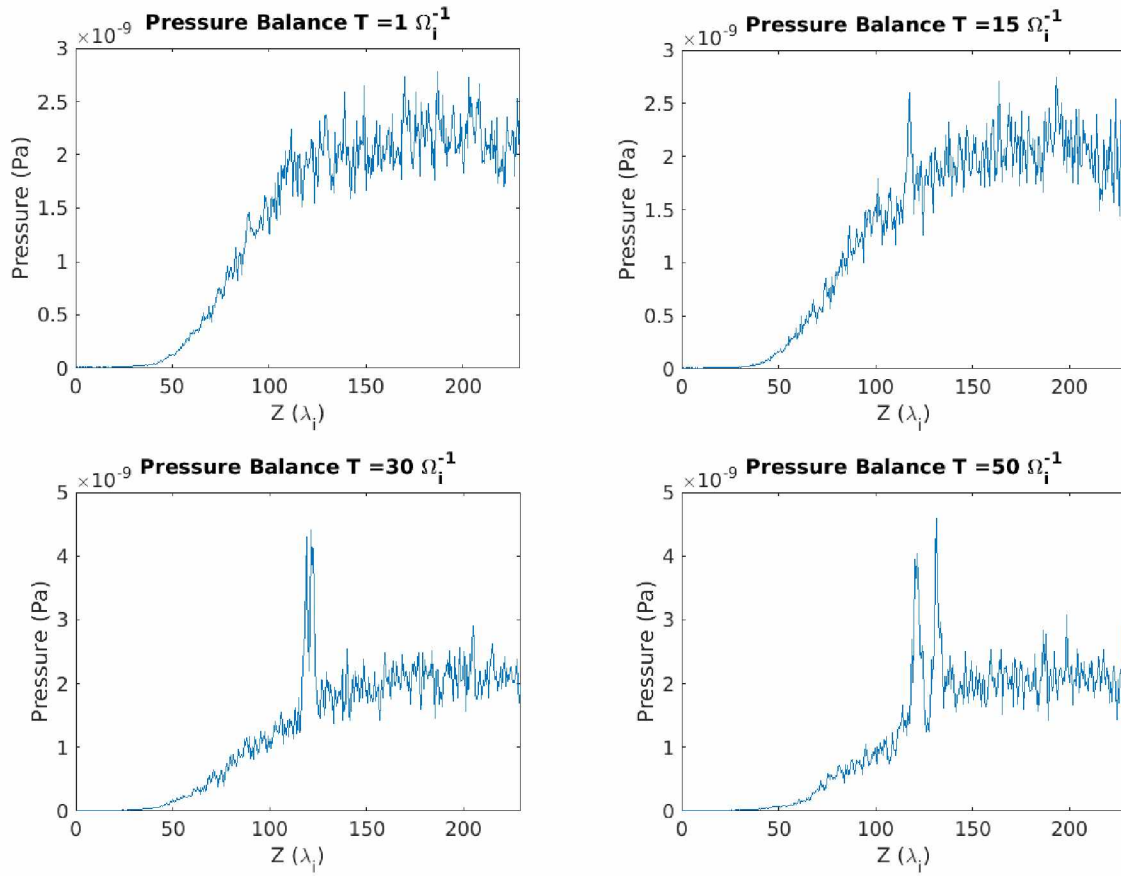


Figure 4.7: Pressure evolution of the 3D RT instability. Initially, the entire domain is in pressure balance. Growth of the instability and bending of the background magnetic field can cause an increase of pressure at the interface boundary. This disruption of the pressure balance shifts the boundary in the positive z direction. See Figure 4.8 for a comparison with other macro scale quantities.

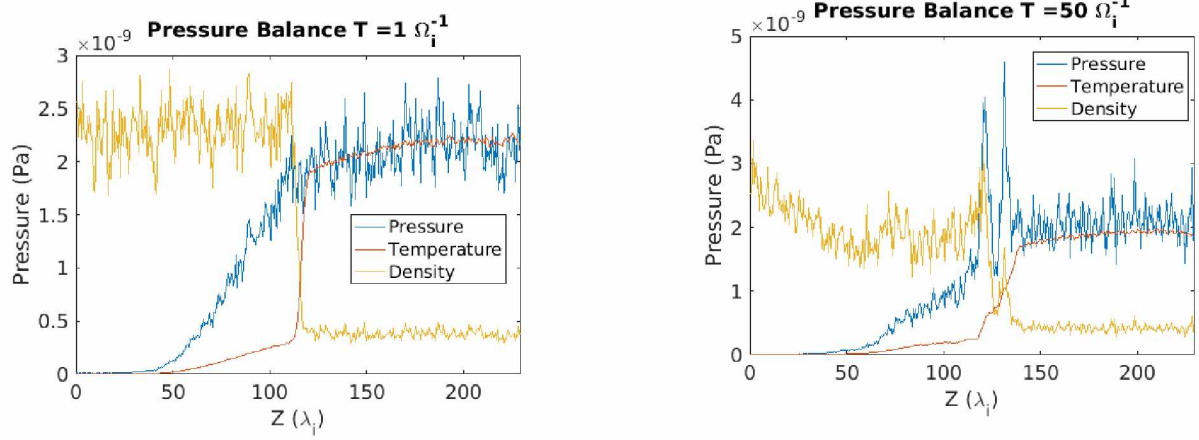


Figure 4.8: Pressure comparison with temperature and density. Change in the pressure profile near the interface boundary is associated with density depletion and thermalization. Mixing of the plasma smooths out the temperature profile, while a loss of pressure on the $z < z_0$ side of the boundary causes a density depletion. Plasma accumulates near the boundary where pressure is greatest.

This eliminates the reflection, and allows motion of the magnetic field lines at the boundary. The size of the domain, L_y , still limits the size of the fundamental k_{\parallel} mode. In this scenario, we will not be seeding a perturbation into the ion velocities, and instead let the instability form through a stochastic process. This is illustrated in Figure 4.9.

The self-seeding run require more modification in order to run in a reasonable time. Using the same parameters as in section 3.2 would take weeks to run before the formation of any appreciable RT instability. Therefore, we modify some of the parameters to increase the growth rate. First we increase the density gradient by setting $\rho_1 = 6\rho_2$ (an increase in the Atwood ratio from $\frac{1}{2}$ to $\frac{5}{7}$), and increase the effective gravity ($g_0 = 0.8v_{th}^2/\lambda_i$). A corresponding change in the thermal velocity profile based on Equation 3.10 is required to maintain pressure balance. Finally, we increase the ion-electron collision frequency, which has the effect of increasing magnetic diffusion so that the magnetic field lines will not bend too much. This is represented in the hybrid code with the parameter ν_{init} , which is the coefficient of the resistive term in the generalized Ohm's law ($\nu\mathbf{J}$, see Equation 1.13). The nominal value of ν_{init} is $0.002 \Omega_i$ for all previous simulations, but is increased to $0.01 \Omega_i$ for

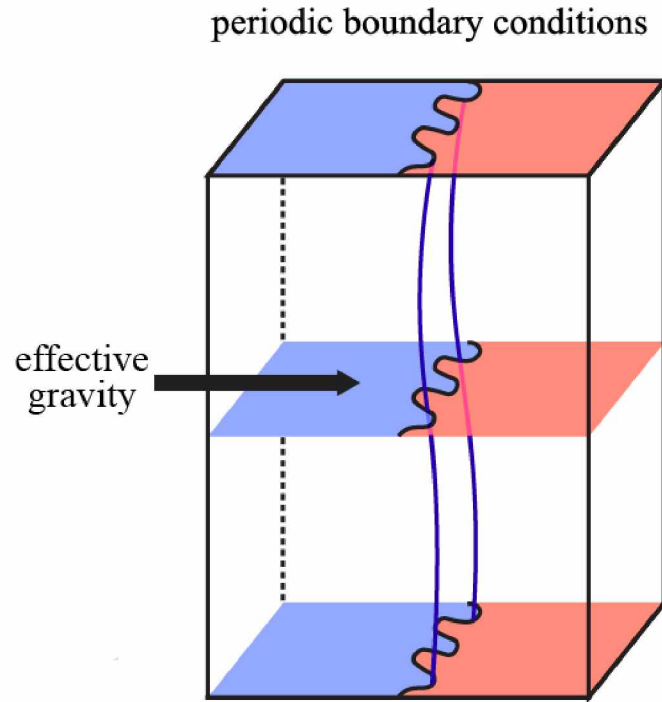


Figure 4.9: 3D RT simulated domain with periodicity along the vertical axis. The simulated region of the magnetodisc is shown in Figure 1.8. The top and bottom boundaries are periodic. Stochastic ion motion provides the onset of the surface waves. Increased magnetic diffusion prevents the field lines from bending very much.

Table 4.1: RT simulation parameters

Simulation	λ_i (km)	ρ_i (λ_i)	g_0 (v_{th}^2/λ_i)	ρ_2 (cm^{-3})	ρ_1 (ρ_2)	B_y (nT)	ν_{init} (Ω_i)
2D RT	2348	3.4	0.2	0.05	3	5	0.002
3D RT, seeded	2348	1.4	0.2	0.05	3	20	0.002
3D RT, self-seeded	1660	3.6	0.8	0.05	6	20	0.01

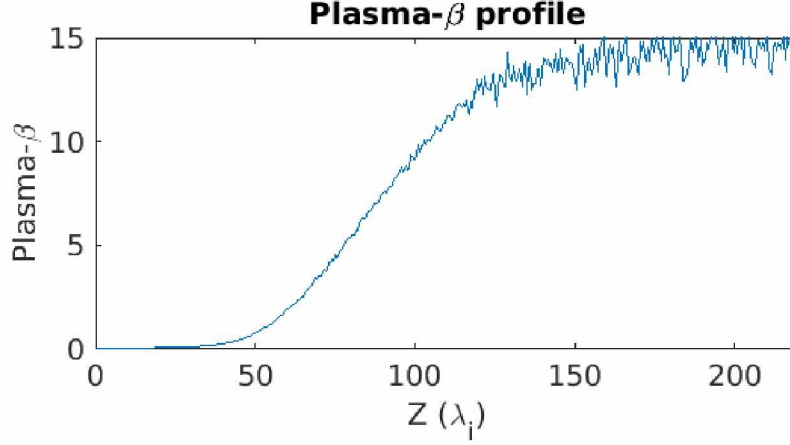


Figure 4.10: Plasma- β profile of the 3D RT instability with periodicity along y . $\beta > 1$ at the boundary interface so ion kinetic motion is resolved on the grid.

the self-seeded run. We no longer have direct comparison with the 2D RT instability, but runtime has been reduced to 26 hours. The plasma- β profile is shown in Figure 4.10. The increase in the Atwood ratio has also increased β so that ion kinetics have similar resolution to the 2D RT instability ($\rho_i \sim 3.6 \lambda_i$ at $z = z_0$, so ion gyromotion is resolved in the relevant region of the domain). Table 4.1 shows a comparison of the parameters used in all of the 2D and 3D RT simulations.

4.3 Simulations with Seeded Wave Modes

Growth rates are limited by the second term in Equation 1.12, which includes $\mathbf{k} \cdot \mathbf{B}$, indicating that parallel propagating waves inhibit growth. We simplify this term to $k_{\parallel} B_y$, and substitute $k_{\parallel} = m_y \pi / L_y$, where m_y is the parallel wave mode. We will limit our assumption

to the $m_y = 1$ case. That leaves us the expression for the maximum growth rate:

$$\gamma = \sqrt{\frac{mg\pi A}{L_x} - \frac{2\pi^2 B_y^2}{\mu_0 L_y^2 (\rho_1 + \rho_2)}} \quad (4.3)$$

Increasing L_x or density decreases the effect of the parallel wave mode, while increasing the background magnetic field suppresses growth of the instability. Figure 4.11 shows the growth of the instability for the $m = 3$ case. Plasma- $\beta > 1$ in this region, so convection is driven by free-energy in the system (i.e gravitational potential). The magnetic field lines become twisted with the motion of the plasma, and a parallel wave mode is transported from $y = y_0$ towards the y boundaries.

We analyze the growth rate of the 3D seeded runs similar to 2D case, using the change in $\ln v_z$. Plasma motion is occurs primarily in the $y = y_0$ plane, so we confine our sampling of v_z to within three grid cells of that plane. We also limit the sampling to before $50 \Omega_i^{-1}$ to avoid including effects from the later pressure collapse. Conducting the simulation for all wave modes between $m = 1$ to $m = 12$, we compare the resulting growth rates with the expected values from Equation 4.3. This is shown in Figure 4.12. Like the 2D case, we have close agreement with the linear theory. Growth rates are slightly less than the predicted values for $m \leq 10$. More unexpected is the large increase of the growth rate for $m > 10$. It is likely that this is just statistical noise, but it could also be due to the decreased influence of k_{\parallel} for large values of m . Since the growth rate is faster, the surface waves form and deform the magnetic field (i.e. magnetic tension) before there is any effective propagation of the wave to the fixed resistive boundary. Alternatively, shorter wavelengths might imply that some magnetic decoupling is taking place due to ion inertial effects (at $m = 11$, $k_{\perp} \sim 2\pi/5\lambda_i$), reducing the effectiveness of magnetic tension.

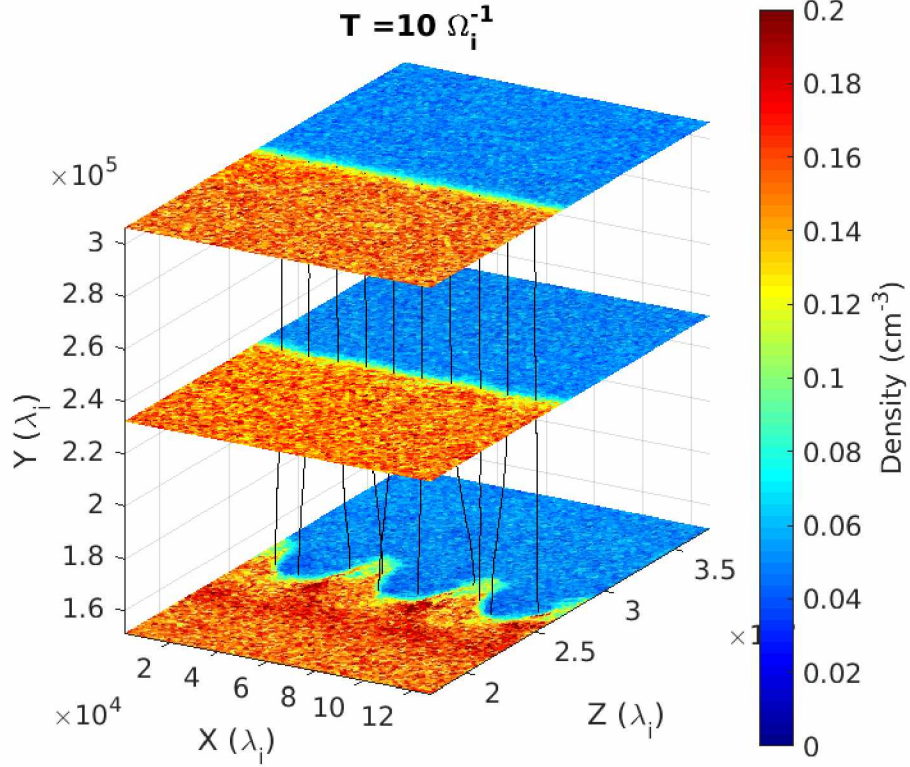


Figure 4.11: Formation of the $m = 3$ wave mode in 3D. Only the span $L_y/2 < y < L_y$ is shown. The magnetic field is modeled as black lines. As seen in the lowest panel, there is a density increase near the boundary. Growth of the instability creates a wave in the magnetic field that propagates along y and creates an effective k_{\parallel} . The magnitude of k_{\parallel} is limited by L_y .

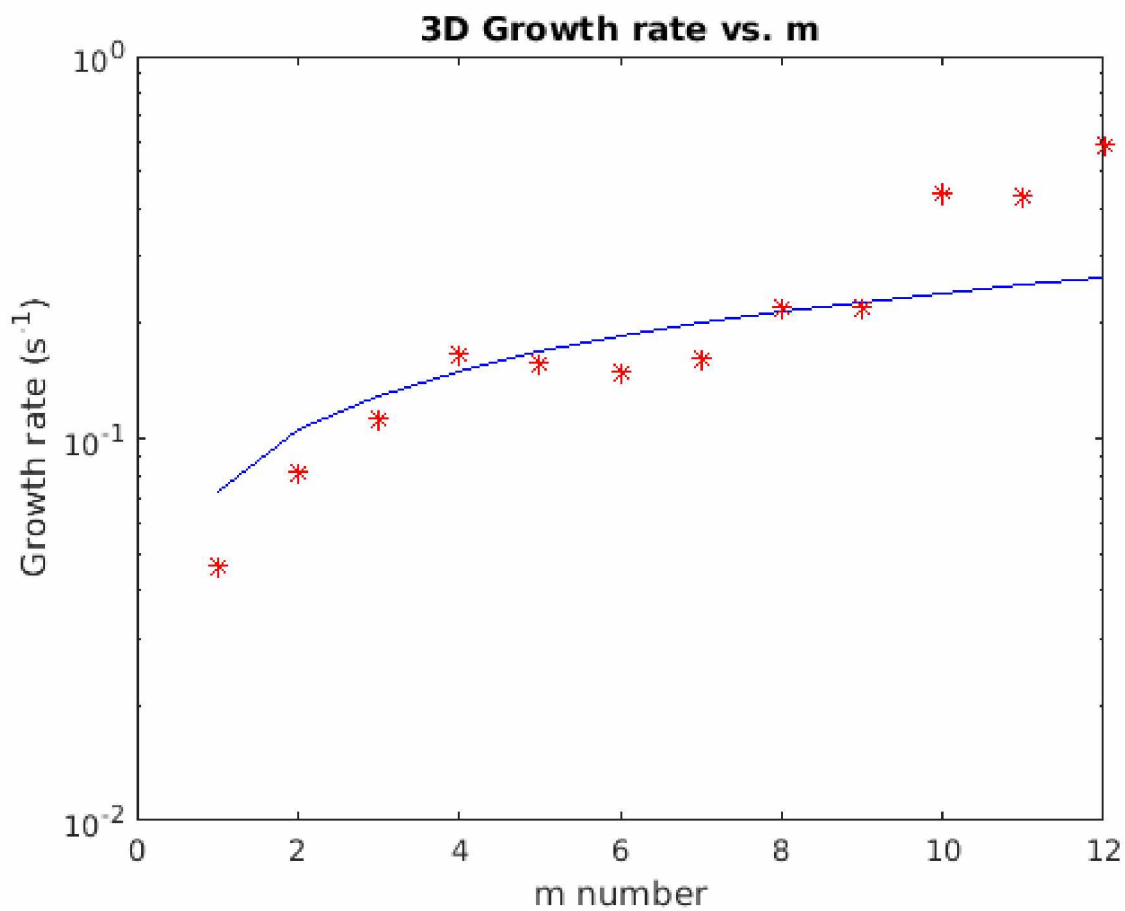


Figure 4.12: 3D RT growth rate comparison. The blue line represents the analytical prediction based on Equation 4.3.

4.4 Self-seeded Simulations

Self seeded runs have a much slower growth rate than the simulations with an initial perturbation. Formation of the instability depends on the stochastic motion of the ions near the boundary. As there is no initial bulk flow, and a strong initial magnetic field, the earliest surface waves do not manifest on the grid until about $T = 10 \Omega_i^{-1}$. The initial mode structure is constructed of short wavelengths. In addition, the transition region, or width of the mixing layer, increases with time. However, the initial short wavelength peaks do not expand into the transition region, but are rather subsumed by coalescence. Late in the simulation, larger wave modes are present, but ion-scale structure remains. Finally, there is a slight drift in the interface boundary in the $+z$ direction. The initial pressure balance is sufficient at the start of the simulation, as the interface boundary remains stable until the formation of the surface wave. Only at about $T = 26 \Omega_i^{-1}$ does the pressure balance fail enough to move the boundary. Fortunately, this does not result any further disruption of density or velocity distribution, but will make it more difficult to conduct a wave analysis later. Figure 4.13 shows the evolution of the instability.

Variation of the instability along y comes from phase differences in the initial formation of the surface waves. The surface waves that initially form at $y = y_0$ are greatly separated from the surface waves that form at the y boundary, with the only mediation through parallel propagating waves. Very small parallel wave modes are one factor inhibiting the growth of the initial waves, due to magnetic tension between adjacent grid cells. The earliest surface waves (large k_\perp) have little correlation in phase. This is best illustrated in Figure 4.14. An isosurface representing the interface boundary (indicating where the mixing ratio is 0.5) is included to show variation along y . The left figure shows the structure of the interface boundary at an early point in wave formation. The boundary is thin, but there is significant variation along y . The right figure shows the isosurface after coalescence into larger wave modes, and the increase of size of the transition region. Here the phase difference between the layers has been reduced, and the surface waves have become better correlated, making

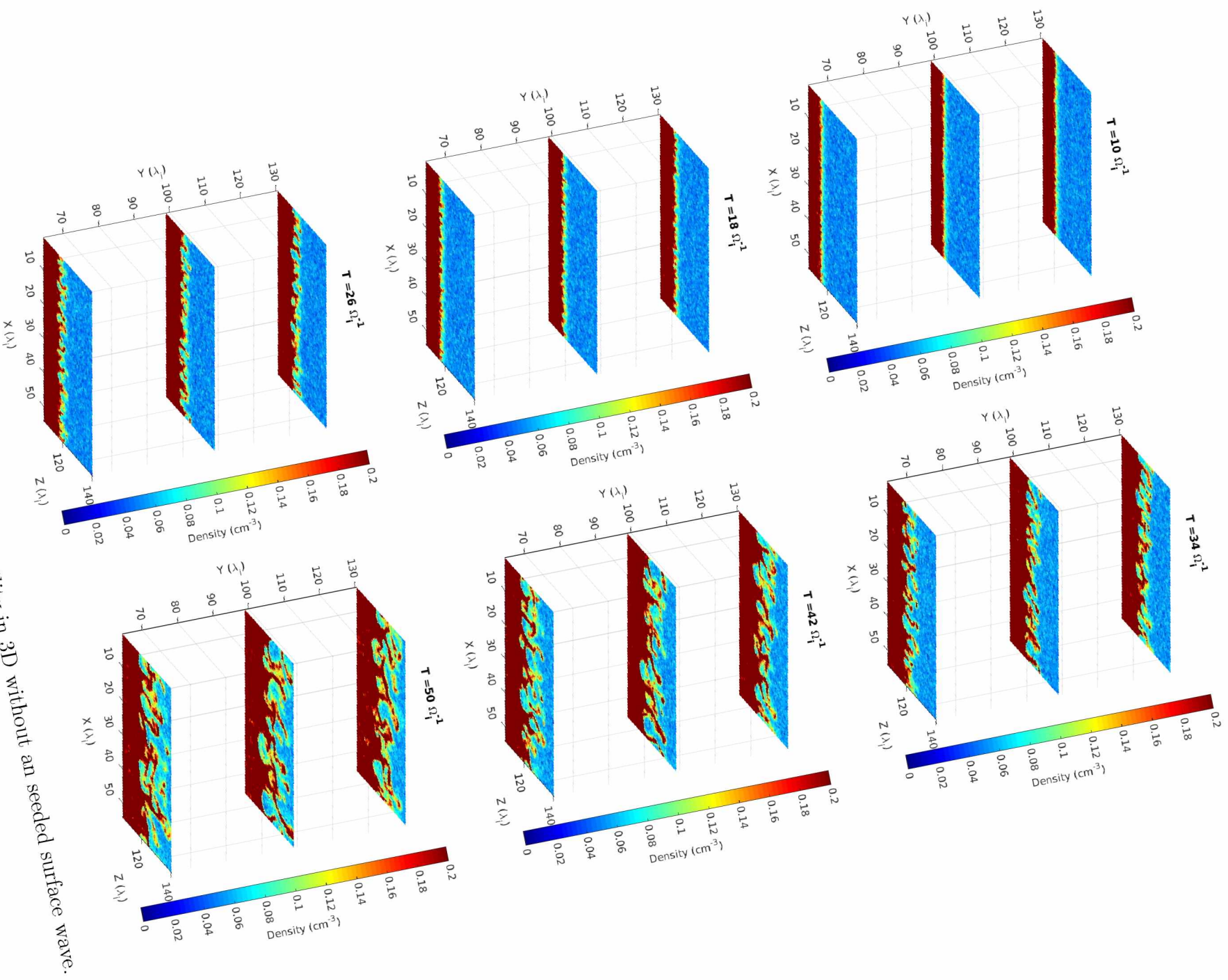


Figure 4.13: Growth of the RT instability in 3D without an seeded surface wave.

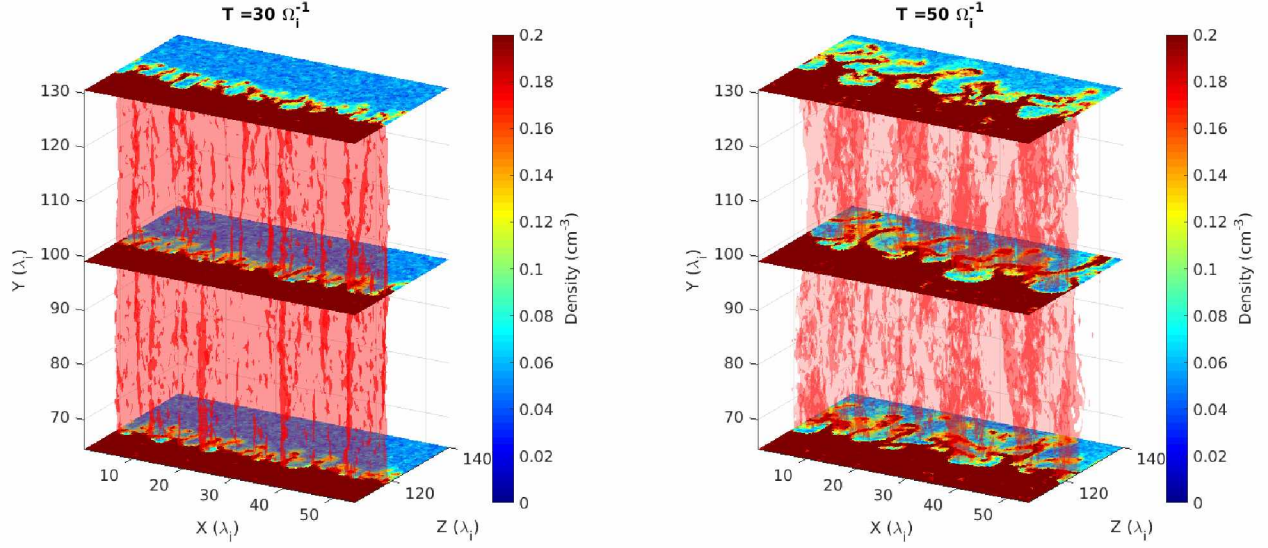


Figure 4.14: Phase alignment in the RT instability. The red isosurface represents the interface boundary where the mixing ratio is 0.5. Variations in phase produce detailed structure in the interface boundary. Later, after propagation of the parallel waves in the magnetic field, the m number decreases, and the phases of the waves become more aligned.

the instability essentially 2D.

The finger-like structures that form have widths that are on the order of λ_i . Since $\beta \sim 13$, the ion gyroradius, ρ_i , is $\sim 3.6 \lambda_i$. This makes the the width of the structures near ρ_i as well. The boundary layer separating the fingers is likewise very thin, less than ρ_i . Ion gyromotion then becomes a relevant mechanism for transport across the boundary separating the fingers. The transport of ions in this manner is similar to hybrid simulations of the Kelvin-Helmholtz instability [Cowee *et al.*, 2009]. Ion gyration across the thin boundary is a component of “superdiffusion” of plasma.

Wave mode analysis is conducted by performing a spatial Fourier transform of density at the interface boundary at $y = y_0$, similar to the analysis conducted in section 3.4. The transform is repeated for each time step to find the change in wave numbers with time. One challenge is that interface boundary is moving in the $+z$ direction, so the location of the transform has to move with it. For this reason we conducted the transform at three locations, offset from $z = z_0$. These are at $z = 115 \lambda_i, 120 \lambda_i$, and $125 \lambda_i$. One advantage of

this approach is that we can more easily characterize the motion of the boundary. Prior to the boundary crossing each of these locations, there will not be any appreciable wave power. Figure 4.15 shows the Fourier transforms for each of these locations.

Like the 2D results (see Figure 3.12), there is no initial preferred wave mode. At $z = 115 \lambda_i$, there are no identifiable modes until $T = 30 \Omega_i^{-1}$, but by then results are unreliable because the interface boundary has moved. All that is left is evidence of the tips of the surface waves. $z = 120 \lambda_i$ shows wave power starting at $T = 22 \Omega_i^{-1}$, with $m = 8$ and $m = 14$ modes. This coalesces into modes between $m = 5$ and $m = 10$ before moving on. Finally, at $z = 125 \lambda_i$, the dominant modes are $m = 5, 10$.

Lastly, we look for the formation of any electric field parallel to the magnetic field in the domain, as a result of small scale magnetic reconnection. E_{\parallel} can be induced by increasing the diffusion parameter (ν_{init}) to $0.01 \Omega_i$, as we did earlier to reduce problems with pressure balance. Alternatively, we can add in a electron temperature of 100 eV, which creates an electron pressure gradient for kinetic Alfvén waves. Both of these approaches add an extra term to the electric field update. There is no significant change in the magnitude of E_{\parallel} using either of these approaches.

Figure 4.16 shows the locations where $E_{\parallel} > 8.30 \times 10^{-5} \text{ Vm}^{-1}$. These "blobs" are on the order of λ_i , only a few grid cells wide. Twisting of the magnetic field from growth of the instability causes slippage of the field in these locations. This allows plasma to escape from its originating field line. We see evidence in each of the three layers representing density, where a number of plasmoid "blobs" have broken from spiked fingers, and have been transported along z .

4.5 Conclusion

Hybrid simulation gives us the advantage of looking at the ion kinetic scale effects of plasma motion in the RT instability. One effect is an inverse turbulent cascade, where energy injection at small scales cascades to large scales, and leads to the growth of larger surface

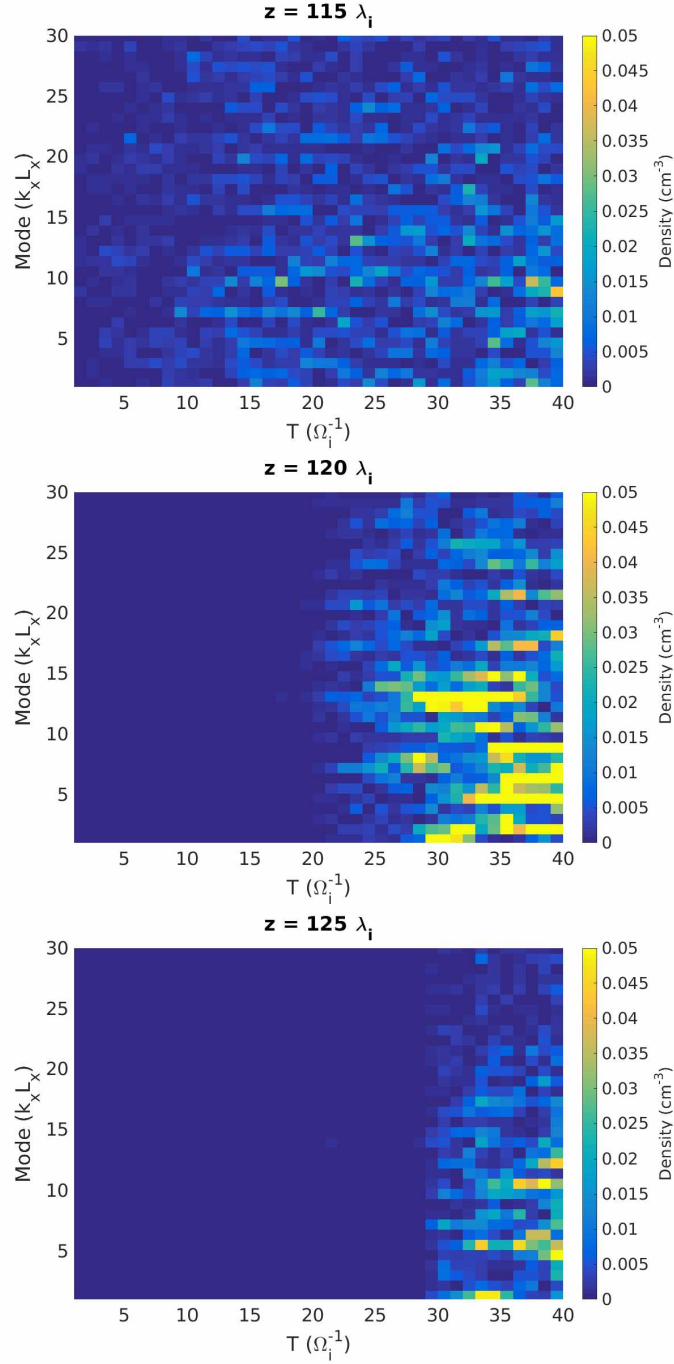


Figure 4.15: Wave power coalescence in density over time. We examine the fast Fourier transform at three different values of z , because of motion of the interface boundary. Similar to the 2D case, wavepower is not focused into any specific m number until coalescence. From the last panel we see that most of the wavepower is in the $m = 2$ and $m = 4$ modes by the end of the simulation.

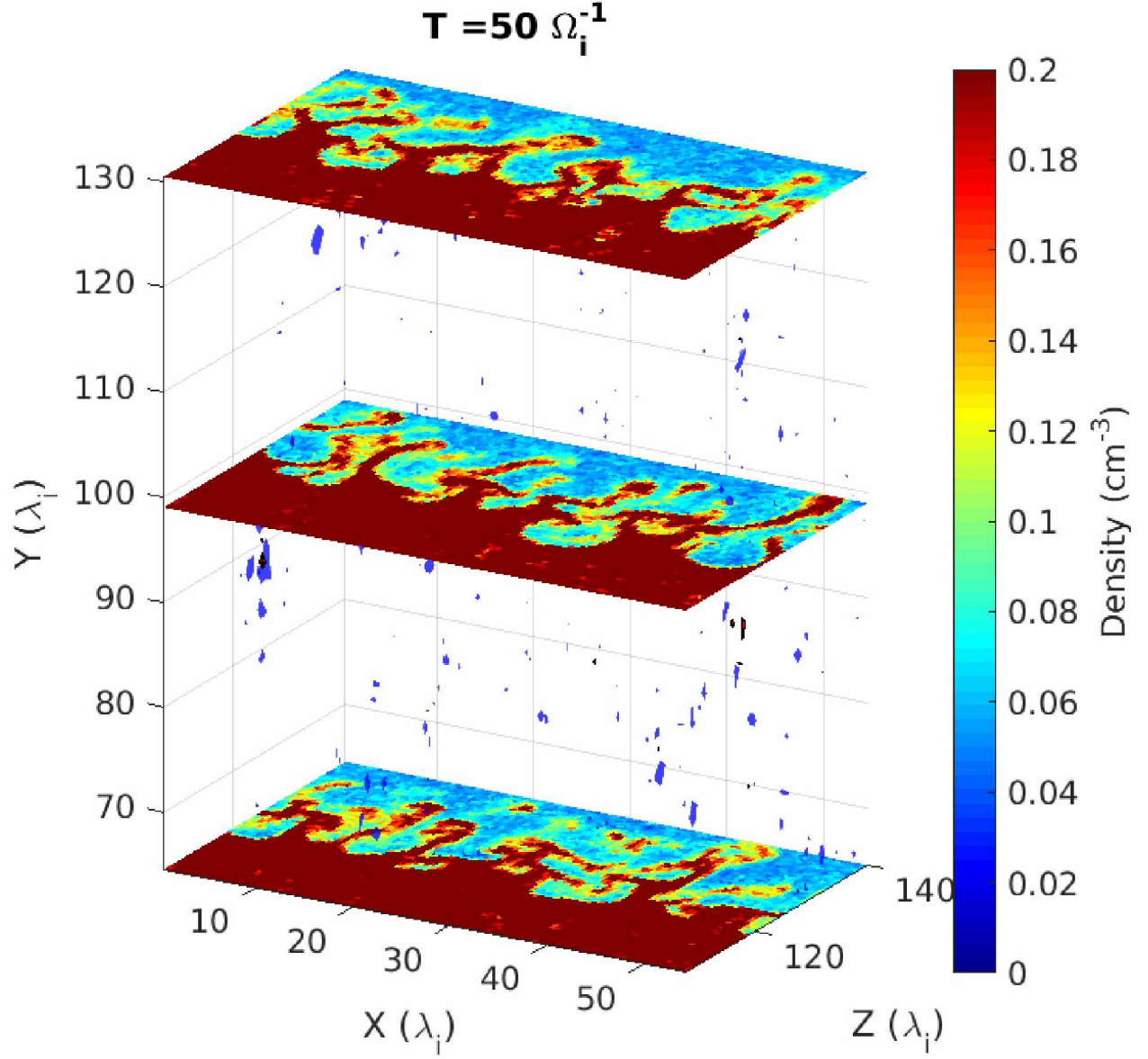


Figure 4.16: Regions of parallel electric field. The blue regions represent areas where $E_{\parallel} > 8.30 \times 10^{-5} \text{ Vm}^{-1}$ at the ion inertial scale. This strong guide field reconnection allows diffusion of the magnetic field, detaching small plasmoids. Thus plasma becomes unfrozen from its initial field lines and is transported radially outward.

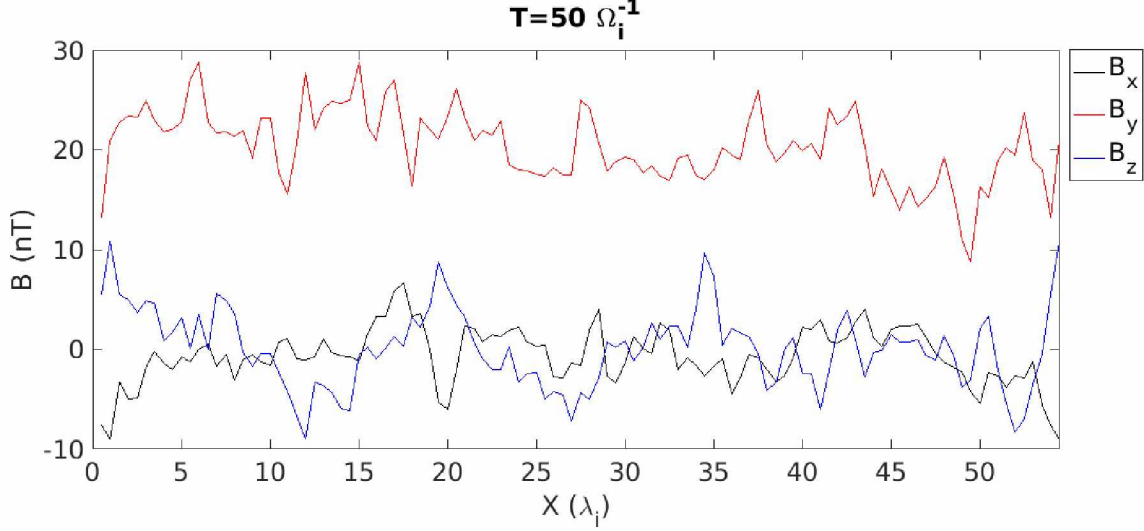


Figure 4.17: RT 3D magnetic field profile across x at $y = y_0, z = z_0$. The profile can be compared to the time series magnetometer data from Saturn (see Figure 1.9). The distance between peaks is $\sim 5\lambda_i$, similar in size to the structures at Saturn.

waves. Stochastic ion motion is the source of the original surface waves in the instability for the unseeded case. The evolution of the instability includes growth of finger-like structures on the order of λ_i . The thickness of the resulting current sheets is also on near λ_i .

Just as with the 2D RT simulation, larger k_\perp has larger growth rates than smaller k_\perp in the seeded runs of the 3D RT instability. Growth rates are lowered by the inclusion of k_\parallel , which is representative of magnetic tension, which acts as a stabilizing force since we are not considering the case of the ballooning instability. However, if we could run the simulation with the frozen field lines at the y boundary for a longer duration, we might witness collapsing flux tubes. Figure 4.17 shows variation in the magnetic field, including B_y at $y = y_0, z = z_0$ across the x axis for $T = 50 \Omega_i^{-1}$.

Fourier analysis of the perpendicular waves along x through the boundary layer reveals the presence of a turbulent cascade for the self-seeded case. The Kolmogorov relationship holds for wavelengths within the inertial range of wavelengths. The grid resolution was insufficient to probe the dissipation range, below λ_i . This is consistent with the detailed structure that is observed in Figures 4.13 and 4.16. Turbulent waves can then propagate to higher latitudes, until the narrowing of the channel makes the electron inertial length relevant. Fragmentation

of the waves at this scale involves inertial Alfvén waves that accelerate electrons into the loss cone and generate the observed broadband aurora. Conducting the same Fourier analysis for the parallel modes (a spatial sampling along y through the center of the boundary layer) shows that k_{\parallel} is not turbulent. The slope is -1, not -5/3, which is consistent with pink noise. Figure 4.18 details the Fourier analysis.

The turbulence observed is a result of counter propagating waves along the magnetic field. The formation of surface waves in the unseeded simulation has an initial phase that varies along y . The motion of the plasma launches counter propagating parallel waves that interact and create turbulence in the perpendicular components of the magnetic field. This is similar to the formation of turbulence in the 2D eggbox simulation from Chapter 2. The counter propagating waves in the eggbox are forced through velocity perturbations, while the 3D RT turbulence is driven naturally through the formation of surface waves.

Next we examine evidence of radial plasma transport. One evidence is the increase of mixing of ions across the interface boundary. Figure 4.19 shows the increase of grid cells that have a mixture of tagged ions that originate from both sides of the instability. Each time step an algorithm takes a summation of all grid cells that have a mixing ratio between 0.25 and 0.75 (i.e. a grid cell with more than a quarter of its ions that originate from the opposite side). This quantity is then normalized to the initial sum of cells that have mixed ions (the cells near the boundary layer are initialized with ions from both sides of the discontinuity). The number of mixed cells increases by a factor of five by $T = 47 \Omega_i^{-1}$. The mixing ratio also exhibits oscillation, with a period of $2\pi \Omega_i^{-1}$, the ion gyroperiod. Individual ions are transported across the interface boundary as part of their gyromotion. Return gyromotion briefly reduces the mixing of the plasma. This is evidence of plasma transport, but is insufficient to demonstrate decoupling of the plasma from the magnetic field. However, the presence of parallel electric fields and spatially isolated high density regions is indicative of transport of small plasmoids through strong guide field reconnection. The width of the finger structures is near ρ_i , so ion gyromotion also becomes a mechanism of diffusive

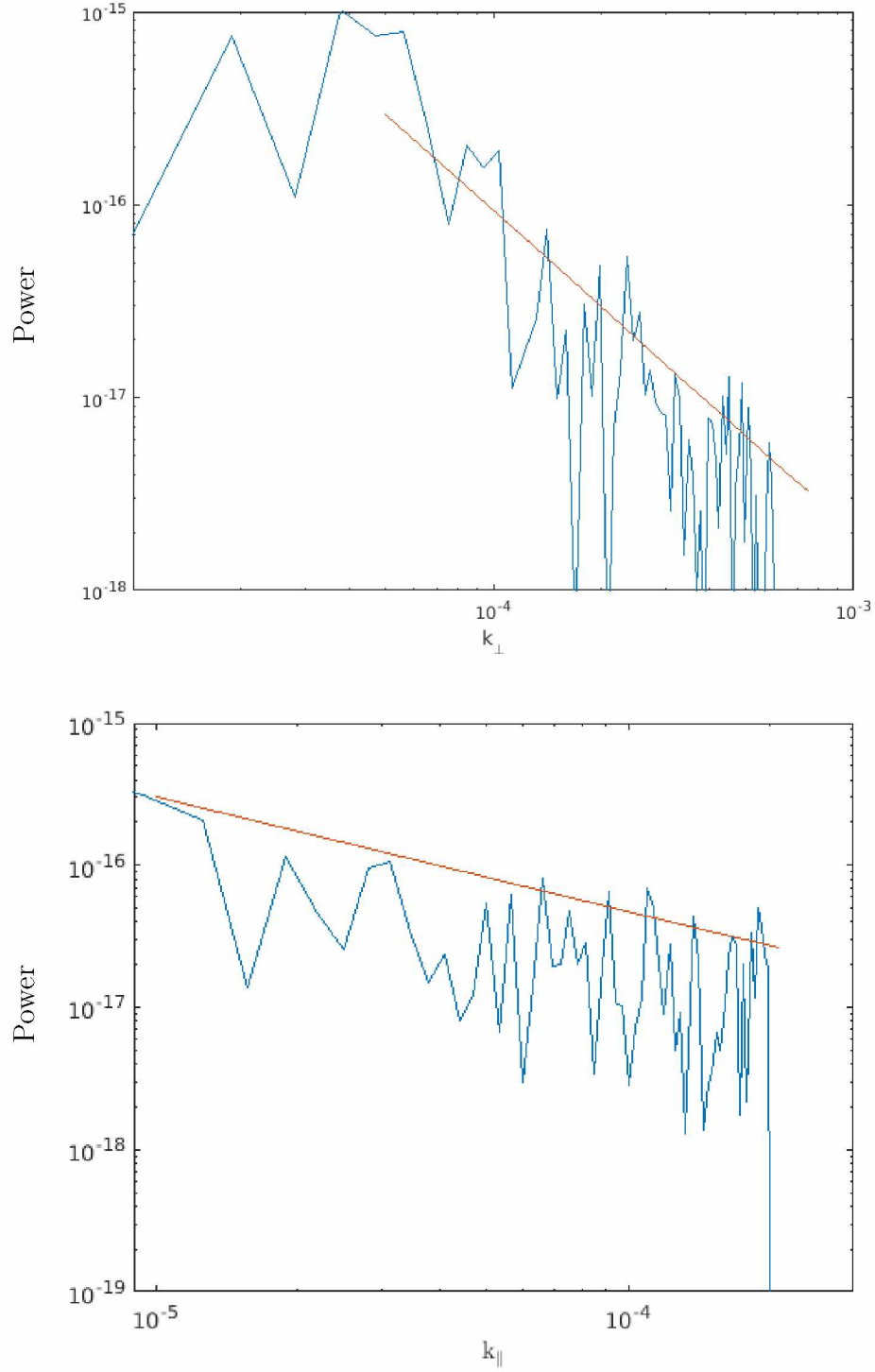


Figure 4.18: Fourier analysis of the perpendicular and parallel wave modes in the self-seeded RT instability. The red lines on each plot represent the fitted slope. For k_{\perp} , the slope is $-5/3$, the expected value for the turbulent cascade. For k_{\parallel} , the slope is -1 , which is consistent with pink noise.

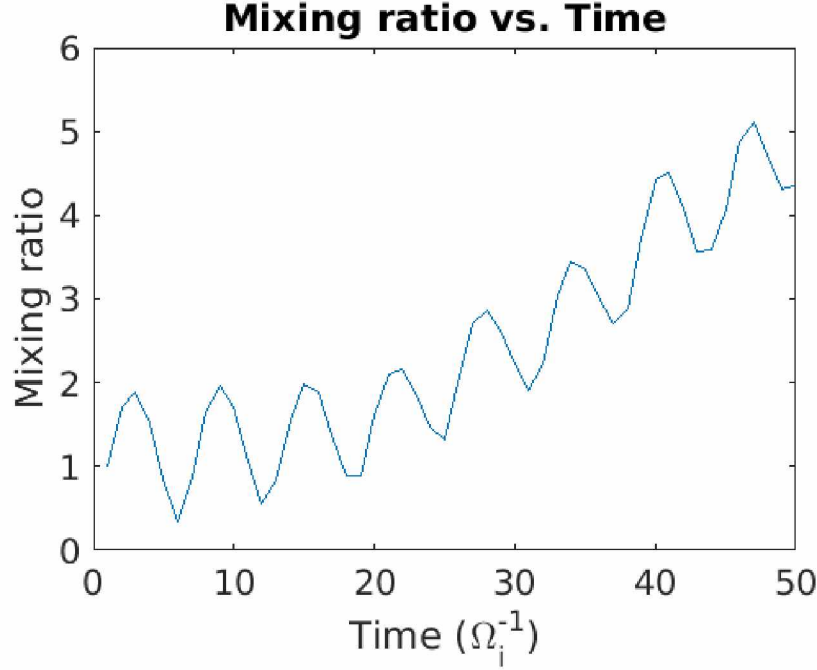


Figure 4.19: Change in mixing ratio over time by grid cell. The sum of grid cells that have more than a quarter of their interior ions originate from the opposite side of the density discontinuity is plotted against time. Mixing increases by a factor of 5 by the end of the simulation. The oscillation is a consequence of ion gyromotion.

transport.

We now compare the simulation results to magnetometer data from Saturn. Figure 4.17 shows the components of the magnetic field. The major peaks (or current sheet crossings) are separated by $\sim 1.4 \times 10^4$ km, or $5 \lambda_i$. The corotational plasma flow is about 100 km s^{-1} , making the current sheet crossings roughly 6.0×10^4 km. Plasma conditions (from *Thomsen et al.* [2010]) are such that λ_i is ~ 5000 km, and the typical distance between current sheet crossings is $12 \lambda_i$. Large scale surface waves form at the same order of magnitude as at Saturn.

If we assume that the instability growth rate stagnates at some point in the equatorial region, the size of the perpendicular wavelengths can be estimated using Equation 4.3. Setting γ to zero, we obtain a relationship for the two terms in the equation:

$$\frac{gA}{L_x} = \frac{2\pi B_y^2}{L_y^2 \mu_0 (\rho_1 + \rho_2)}. \quad (4.4)$$

Solving for L_y , the length of the cavity, we obtain

$$L_x = \frac{gAL_y^2\mu_0(\rho_1 + \rho_2)}{2\pi B_y^2} \quad (4.5)$$

which we can solve using known parameters at Saturn, at $L = 15$. The fundamental mode L_y is estimated to be about $8 R_S$ (the width of the magnetodisc), and g can be estimated using the centrifugal force at $L = 15$ ($g = v_\phi^2/r$). Mass density is roughly $6.3 \times 10^{-21} \text{ kg m}^{-3}$ at $L = 15$, and the Atwood ratio is $3/5$ based on the density at $L = 14$ [*Thomsen et al.*, 2010]. The dipolar field strength is 6 nT. From this, we estimate the wavelength to be $\sim 2.4 \times 10^6$ km. This is same order as the size of the waves estimated from the Cassini magnetometer data (Figure 1.9).

Conclusion

The magnetodisc at Jupiter and Saturn is characterized by turbulence in the magnetic field. Broadband spectra of precipitating electrons at Jupiter suggest that a process is underway whereby large scale perturbations undergo a turbulent cascade. The cascade couples large perturbations to dispersive scales (the kinetic and inertial Alfvén wave). Hybrid simulations of wave propagation in the giant magnetospheres help us understand the Io-Jupiter interaction and transport related physics. In the plasma torus and throughout the magnetosphere, the propagation of Alfvén waves carries power to Jupiter’s ionosphere to generate aurorae. The reflection of waves within the torus/magnetodisc contributes to turbulence via the interaction of counter propagating waves. The centrifugal force from rapid rotation induces the onset of a centrifugally-driven flux tube interchange instability (akin to the RT instability) in the magnetodisc, which is the origin of turbulence within the magnetodisc. Turbulence is one possible explanation for the observed non-adiabatic heating of the magnetodisc.

We will return the discussion to our guiding questions outlined in the introduction and how they enhance our current knowledge of magnetosphere dynamics.

5.1 Power Transmission in the Io Plasma Torus

- How much power from Io-induced waves is transmitted out of the torus, and what are their dispersive characteristics?

Wave power transmission (53%) is much higher than previous models ($\sim 20\%$) [*Wright, 1987; Delamere et al., 2003*]. This increases the available power transmitted to higher latitude. This means that more energy is available to couple directly to the ionosphere. In the previous limit (20% transmission), nearly all of the wave power was required to generate the observed radiated power (only 10% of electron energy is converted into light in the aurora, with the rest being dissipated in the ionosphere, meaning that all the wave energy had to go into electron

acceleration to account for the power observed in the Io aurora). The power transmitted from the torus is $0.3\text{-}1.5 \times 10^{-4} \text{ W m}^{-2}$, depending on the mass loading rate. More mass loading increases the total power transmitted out of the torus, but does not increase the ratio transmitted power to reflected power.

The hybrid code self-consistently evolves the state of the ion distribution function, which enables us to resolve ion inertial and some ion kinetic effects within the torus, which is a more realistic description of the Io-Jupiter interaction than previous models [*Wright, 1987; Delamere et al., 2003; Jacobsen et al., 2010*]. Pickup ions in the hybrid simulation are modeled, rather than just an initial perturbation in flow, or fluid interaction with a conducting obstacle. The momentum transfer rate coupled with the mass loading time scale determines the size of the original Alfvénic perturbation. The pickup ions have an initial ring beam distribution that is scattered into a thermal Maxwellian distribution. This results in the propagation of slow EMIC waves through the torus. The interaction of reflected Alfvén waves and EMIC waves could be a contributor to turbulence in Io’s wake and/or pitch angle scattering of electrons. Turbulence is not observed in the 1D torus model, because there is no inclusion of perpendicular wavelengths. Further investigation requires 2D, or even 3D simulation to include the influence of k_{\perp} .

The 1D torus model includes the characteristics of waves escaping the plasma torus. We have previously identified the right-hand and left-hand circularly polarized waves modes near the Alfvén resonance. Ion cyclotron waves follow from pickup ion thermalization. The KAW mode is inconsequential within the torus with respect to ion heating and electron acceleration. It may not be necessary to accelerate the electrons within the torus (without E_{\parallel}) if large scale perturbations in the torus map to the electron inertial scale at high latitude. The inertial Alfvén wave would then be responsible for the majority of electron acceleration.

- Is there evidence of turbulence in the interaction of counter propagating waves?

The purpose of the 2D eggbox simulation was to investigate wave propagation at the ion kinetic scale, and include a k_{\perp} term to allow for the formation of KAWs. The first eggbox

simulation had a very low β parameter, which is similar to the plasma conditions within the Io torus. The low β prevented the KAWs from heating the ions, due to the relationship β has between the Alfvén speed and the sound speed:

$$\beta = \frac{nk_B T}{B^2 / (2\mu_0)} = \frac{2nk_B T}{\rho} \frac{\mu_0 \rho}{B^2} = \frac{2\gamma p}{\gamma \rho} \frac{1}{v_A^2} = \frac{2}{\gamma} \frac{C_s^2}{v_A^2} \quad (5.1)$$

When $\beta \sim 1$, the Alfvén speed is comparable to the sound speed, and the KAWs can interact with the ions. For $\beta < 1$, there are too few ions to resonantly interact with the wave. We expect that the majority of auroral electron acceleration happens at high latitudes as a consequence of the inertial Alfvén wave (rather than the KAW), which cannot be addressed by the hybrid simulation. The frequency spectrum of the perpendicular component of the magnetic field shows a Kolmogorov cascade, which is characteristic of turbulence.

5.2 The Turbulent Cascade in the Magnetodisc

- Is turbulence present in the perpendicular modes of the RT instability?

Increasing the value of β in the eggbox simulation to unity improves the effect of ion Landau damping (ion Landau damping is effective when $v_{th} \sim v_A$). The interaction here is similar to the self-seeding 3D RT simulation because of the counter propagating waves. In the initial stages of the RT simulation, the formation of surface waves is due to stochastic ion motion. As a result, phase differences arise between the surface waves parallel to the magnetic field. Parallel propagating waves result from the perpendicular ion motion. In the eggbox, the turbulent cascade transfers energy to smaller wavelengths. The 3D RT simulation instead shows evidence of an inverse turbulent cascade, where wave energy is transferred to larger wavelengths as a result of coalescence. Presumably there is a forward cascade as well to the dissipation scale, but we do not have the resolution to observe it. The eggbox, however, has high enough resolution to address ion heating. In the future we would like to run the RT simulation at high enough resolution to observe heating.

Evidence of heating Saturn’s magnetodisc comes from Cassini magnetometer data [*Kaminker et al.*, 2017], but the source of non-adiabatic heating is still unknown. The 3D hybrid simulation shows that a turbulent cascade is present in the magnetodisc, while the eggbox simulation suggests that when the cascade reaches the ion kinetic scale, ion heating takes place. Thus turbulence could be one source of heating for ions in the middle magnetosphere at Saturn.

- Does the RT instability exhibit coalescence of surface waves (i.e., does the dominant mode cascade to larger wavelengths)?
- Can we estimate k_{\perp} from the RT growth rate and the size of the resonant cavity and compare with observations?

Both the 2D and 3D RT simulations with seeded surface waves show consistency with linear theory of the RT growth rate. The fastest growing modes have higher m numbers. In the self-seeded simulations, small scale waves (at the ion kinetic scale) are manifested first. The slower growing modes have larger wavelengths, but eventually envelop the smaller wavelength modes, completing the inverse turbulent cascade of wave energy larger scales. In the 2D simulation, the waves eventually coalesce into a mode with small m number. This is because there is no limitation on the minimum k_{\perp} . In 3D, the k_{\parallel} mode is introduced, which limits the size of k_{\perp} , based on Equation 4.4 (Assume the growth rate goes to zero when the $\mathbf{k} \cdot \mathbf{B}$ term is large enough to constrain the maximum value of k_{\perp}). The magnetic field perturbations from the RT surface waves are on the order of several λ_i , similar in size to the large perturbations in Saturn’s magnetodisc (the disturbed magnetic field in Figure 1.9).

5.3 Radial Transport in the Magnetodisc

- Is there evidence of a parallel electric field in the RT instability that is indicative of plasma decoupling from the magnetic field?

The unseeded 3D RT simulation shows evidence of radial transport of plasma through ion

mixing. The formation of finger-like structures is the result of wave mode coalescence. The width of the resulting current sheets are on the order of λ_i and ρ_i . The transport of plasma also occurs via ion gyromotion across the current sheet. This kinetic mode of transport never goes away during the inverse cascade because the thickness of the boundary remains at the ion kinetic scale, and is a mechanism of diffusion. We also have evidence of the radial transport as blobs detach from the finger structures. Strong guide field reconnection could facilitate this, as evidenced by patches of increased parallel electric field.

5.4 Future Studies

The hybrid code can only model so far in the Io flux tube as a consequence of discounting electron inertia. Once the Alfvén waves reach the boundary of the plasma torus, a sharp decrease in the density profile increases the wave speed to near luminal, and electron inertia becomes relevant. For future study, we propose to use the Gyrofluid Kinetic Electron (GKE) model [Damiano *et al.*, 2007, 2015] to simulate the behavior of the waves at high latitudes. In this region, electron inertial effects dominate and the GKE code is effective at describing the propagation characteristics of these waves and the resulting coupling to electrons.

The GKE model, set up in dipolar coordinates, has seen extensive application in the study of electron energization by Alfvén waves in the terrestrial magnetosphere at the $L = 10$ field line. It models the electron motion along the magnetic field line as drift-kinetic while ions are treated with a kinetic fluid closure based on a solution of a linear gyrokinetic equation [Cheng and Johnson, 1999]. It is a self-consistent model that can describe the dispersion of Alfvén waves at the scales of the electron inertial ($\lambda_e = c/\omega_{pe} = \sqrt{m_e/\mu_0 n e^2}$) and is therefore effective in describing the propagation of inertial Alfvén waves at higher latitudes and the generation of the parallel electric fields within these waves to couple wave energy to electron energization. The waves identified in the 1D torus model can be used to set up boundary conditions for the GKE model just outside the torus. Time dependent variation of the magnetic field at the equatorial boundary can reproduce the same waves in

the GKE domain.

The turbulent cascade for counter propagating Alfvén waves is also poorly understood in the hybrid code. The 2D eggbox is limited by only one direction for k_{\perp} . From the Vlasov theory of plasma waves, dispersion depends on both components of k_{\perp} [Krall and Trivelpiece, 1973]:

$$-\mathbf{k} \times \mathbf{k} \times \mathbf{E}_1 = \mathbf{E}_1 + i\omega\mu_0 \sum_{\alpha} n_{\alpha}q_{\alpha} \int_L \mathbf{v} f_{\alpha} d\mathbf{v} \quad (5.2)$$

where n_{α} , q_{α} , and f_{α} are the the densities, charges, and distribution functions of all present plasma species, and L is the Landau contour. Of note is the $\mathbf{k} \times \mathbf{k} \times \mathbf{E}_1$ term, which arises from combining two curl operations from Ampere’s law and the magnetic induction equation. The dispersion relationship is then dependent on the allowed wave modes in k_{\perp} , which are incomplete without a 3D model. We therefore propose an additional study using the hybrid code in three dimensions.

In the first case, we would expand the setup for the 2D eggbox, with about 30 particles per cell. Ion temperature is initialized such that plasma- $\beta > 1$. The grid scale would need to be $0.1 \lambda_i$ to capture the dissipation range. Lastly, we need to decide the size of the domain such that the endeavor is computationally feasible. We can reserve compute time on the Chinook cluster for about 240 processing units for 48 hours. Completion within that time frame limits each processor to pushing less than one million ions, not including the time it takes to update the field grid. With these limitations, we can simulate a domain of $n_x = n_y = 151$ grid cells in the perpendicular domain and $n_z = 231$ for the parallel domain. $k_{\perp max}$ is therefore limited to $\pi/15 \lambda_i$, and $k_{\parallel max}$ to $\pi/23 \lambda_i$.

Our investigation only included very local sections of the magnetodisc, ignoring global dynamics. To fully understand radial transport of through flux tube interchange, it is necessary to consider the global entropy profile of the magnetodisc. Flux tube entropy must increase with radial distance to maintain long term stability of the magnetodisc. The interchange motion moves high entropy flux tubes deeper into magnetosphere, which creates an unstable state. Further consideration of radial transport will need to address this problem.

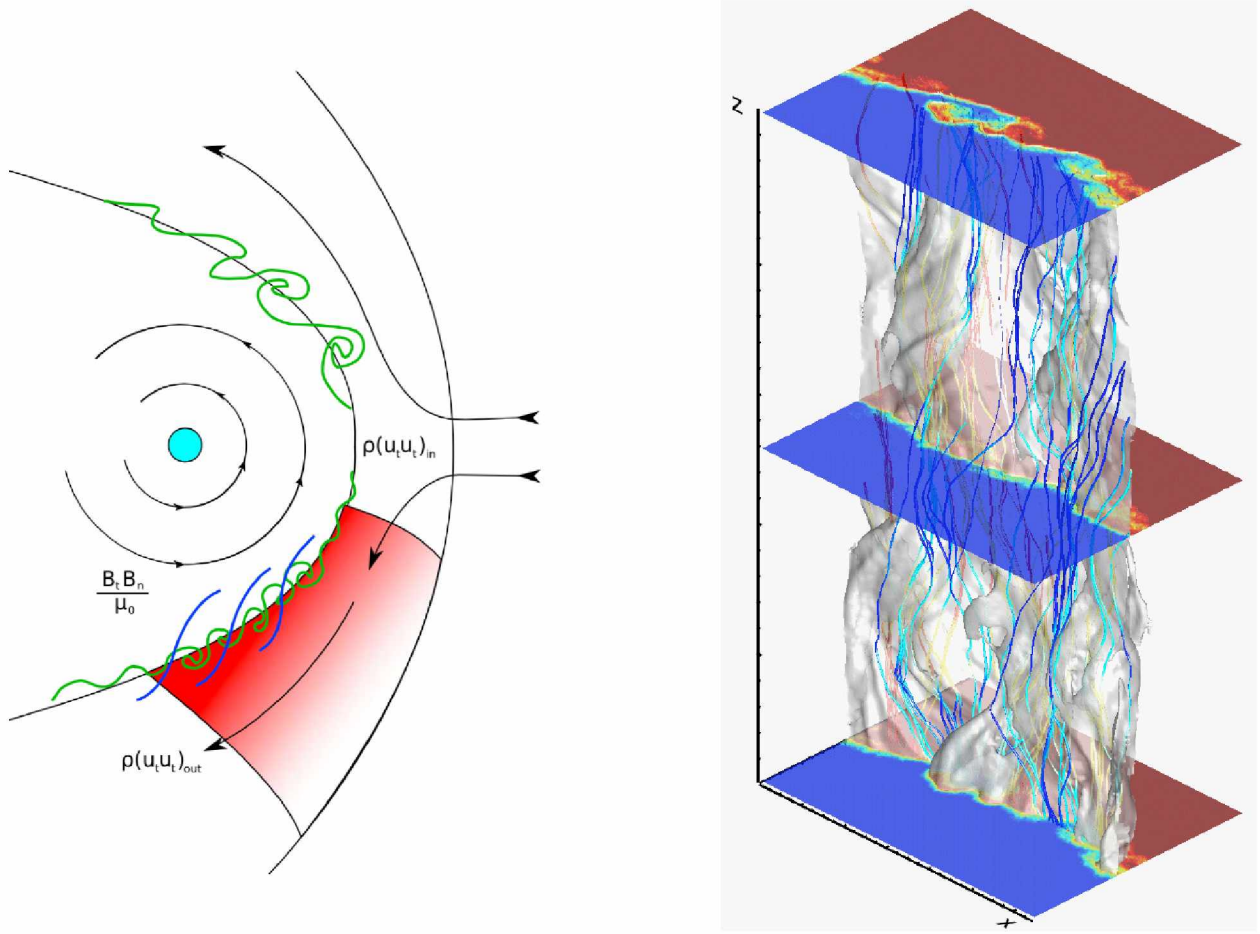


Figure 5.1: Plasma transport at a viscous boundary. On the left, the interface between the magnetosheath flow and magnetodisc circulation is sheared and viscous, making the boundary Kelvin-Helmholtz unstable. The right figure is a 3D hybrid simulation of the KH instability with Saturn-like input parameters and a small magnetic shear.

A further investigation of radial transport will include the interaction of the magnetodisc with the magnetopause. Solar wind interaction with the magnetopause introduces a viscous boundary between magnetosheath plasma and the magnetodisc, as well as opposing shear flows (See Figure 5.1). The resulting tangential drag makes the boundary Kelvin-Helmholtz (KH) unstable. Adaptation of the 3D RT simulation can produce a similar simulation that includes this shear flows. Using this, we can investigate the ion kinetic scale features of a localized section of the magnetopause that might contribute to the asymmetric heating of the day-side magnetodisc. Turbulent heating as a result of RT and KH instability likely occurs at the scales necessary for small scale reconnection [Burkholder *et al.*, 2017].

Appendix A: Derivation of the Growth Rate of the Rayleigh-Taylor Instability

The Rayleigh-Taylor (RT) instability is characterized by a plane boundary between two fluids under the influence of a gravitational field. It is driven by situating the heavier fluid on top of the lighter fluid, which is a higher potential energy state in an unstable equilibrium. The equilibrium condition is described by the equation

$$\frac{\partial}{\partial z} \left[p(z) + \frac{B_y(z)^2}{2\mu_0} \right] + \rho(z)g = 0. \quad (\text{A.1})$$

Any perturbation would lead an unstable state where the heavier fluid would tend to sink while the lighter fluid attempts to rise. We can apply this instability to a plasma system where heavy or dense plasma rests atop a light/tenuous plasma under the influence of gravity or some non-inertial reference frame. We define the coordinate system in an xz plane where gravity is along $-z$, as well as the stratified density gradient. The primary magnetic field is out of plane (y). We limit any components of B to the x and y components. See Figure A.1 for a diagram. We derive the governing equation and growth rate for the RT instability

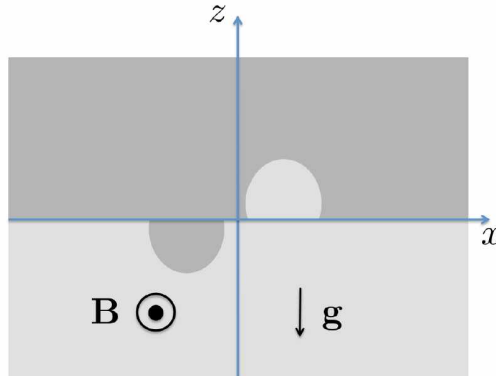


Figure A.1: Diagram of a Rayleigh-Taylor instability. The magnetic field is out of the plane (y), while gravity acts along $-z$. The instability is driven by the higher energy state of a heavy/dense plasma on top of a light/tenuous plasma.

from the MHD equations, and assume incompressible flows [Chandrasekhar, 1961]. We also assume that all variations of the equilibrium state are along z , and that the perturbed

quantities are plane waves of the form

$$\mathbf{u}_1(x, z, t) = \tilde{\mathbf{u}}_1(z) \exp[ikx + qt]. \quad (\text{A.2})$$

We start with using the following equation for momentum with gravity:

$$\rho \frac{\partial \mathbf{u}}{\partial t} = -\rho \mathbf{u} \cdot \nabla \mathbf{u} - \nabla p + \mathbf{J} \times \mathbf{B} - \rho \mathbf{g} \quad (\text{A.3})$$

then linearize each of the MHD equations:

$$\begin{aligned} \frac{\partial \rho_1}{\partial t} &= -\mathbf{u}_1 \cdot \nabla \rho_0 - \mathbf{u}_0 \cdot \nabla \rho_1 - \rho_1 \nabla \cdot \mathbf{u}_0 - \rho_0 \nabla \cdot \mathbf{u}_1 \\ \rho_0 \frac{\partial \mathbf{u}_1}{\partial t} &= -\rho_1 \mathbf{u}_0 \cdot \nabla \mathbf{u}_0 - \rho_0 \mathbf{u}_1 \cdot \nabla \mathbf{u}_0 - \rho_0 \mathbf{u}_0 \cdot \nabla \mathbf{u}_1 \\ &\quad - \nabla p_1 + \frac{1}{\mu_0} (\nabla \times \mathbf{B}_1) \times \mathbf{B}_0 + \frac{1}{\mu_0} (\nabla \times \mathbf{B}_0) \times \mathbf{B}_1 - \rho_1 \mathbf{g} \\ \frac{\partial \mathbf{B}_1}{\partial t} &= \nabla \times (\mathbf{u}_1 \times \mathbf{B}_0) + \nabla \times (\mathbf{u}_0 \times \mathbf{B}_1) \\ \frac{\partial p_1}{\partial t} &= -\mathbf{u}_1 \cdot \nabla p_0 - \mathbf{u}_0 \cdot \nabla p_1 - \gamma p_1 \nabla \cdot \mathbf{u}_0 - \gamma p_0 \nabla \cdot \mathbf{u}_1 \end{aligned} \quad (\text{A.4})$$

Now add in the substitutions for the plane wave analysis, which simplifies to the following:

$$\begin{aligned} qp_1 &= -u_{1z} \partial_z \rho_0 - ik u_{0x} \rho_1 \\ \rho_0 q \mathbf{u}_1 &= -\rho u_{1z} \partial_z u_x \hat{\mathbf{x}} - ik \rho_0 u_{0x} \mathbf{u}_1 - \nabla p_1 + \frac{1}{\mu_1} (\nabla \times \mathbf{B}_1) \times \mathbf{B}_0 - \rho_1 g \hat{\mathbf{z}} \\ q \mathbf{B}_1 &= \nabla \times (\mathbf{u}_1 \times \mathbf{B}_0) + \nabla \times (\mathbf{u}_0 \times \mathbf{B}_1) \\ qp_1 &= -u_{1z} \partial_z p_0 - ik u_{0x} p_1 \end{aligned} \quad (\text{A.5})$$

Expanding the $\mathbf{J} \times \mathbf{B}$ term for each component we get:

$$\begin{aligned}
[(\nabla \times \mathbf{B}_1) \times \mathbf{B}_0]_x &= (\partial_z B_{1x} - \partial_x B_{1z}) B_{0z} - (\partial_x B_{1y} - \partial_y B_{1x}) B_{0y} \\
&= (\partial_z B_{1x} - ik B_{1z}) B_{0z} - ik B_{1y} B_{0y} \\
[(\nabla \times \mathbf{B}_1) \times \mathbf{B}_0]_y &= (\partial_x B_{1y} - \partial_y B_{1x}) B_{0x} - (\partial_y B_{1z} - \partial_z B_{1y}) B_{0z} \\
&= ik B_{1y} B_{0x} + \partial_z B_{1y} B_{0z} \\
[(\nabla \times \mathbf{B}_1) \times \mathbf{B}_0]_z &= \partial_z B_{1y} B_{0y} - (\partial_z B_{1x} - ik B_{1z}) B_{0x}
\end{aligned} \tag{A.6}$$

The components of $q\mathbf{B}_1$ from the induction equation are

$$\begin{aligned}
qB_{1x} &= -\partial_z (u_{1z} B_{0x} - u_{1x} B_{0z} - u_{0x} B_{1z}) \\
qB_{1y} &= -\partial_z (u_{1y} B_{0z} - u_{1z} B_{0y}) - ik (u_{1x} B_{0y} - u_{1y} B_{0x} + u_{0x} B_{1y}) \\
qB_{1z} &= ik (u_{1z} B_{0x} - u_{1x} B_{0z} - u_{0x} B_{1z}).
\end{aligned} \tag{A.7}$$

From incompressibility and $\nabla \cdot \mathbf{B}_1 = 0$ we have

$$\begin{aligned}
iku_{1x} + \partial_z u_{1z} &= 0 \\
ikB_{1x} + \partial_z B_{1z} &= 0
\end{aligned} \tag{A.8}$$

Now we go back to our assumption that $B_z = 0$ and expand the $\rho_0 q\mathbf{u}_1$ and $q\mathbf{B}_1$ terms.

$$\begin{aligned}
\rho_0 q u_{1x} &= -\rho_0 u_{1z} \partial_z u_{0x} - ik \rho_0 u_{0x} u_{1x} - ik p_1 - \frac{1}{\mu_0} ik B_{0y} B_{1y} \\
\rho_0 q u_{1y} &= -ik \rho_0 u_{0x} u_{1y} + \frac{1}{\mu_0} ik B_{0x} B_{1y} \\
\rho_0 q u_{1z} &= -ik \rho_0 u_{0x} u_{1z} - \partial_z p_1 \\
&\quad + \frac{1}{\mu_0} [B_{0y} \partial_z B_{1y} - B_{0x} (\partial_z B_{1x} - ik B_{1z})] - \rho_1 g \\
qB_{1x} &= -\partial_z (u_{1z} B_{0x} - u_{0x} B_{1z}) \\
qB_{1y} &= -ik (-u_{1y} B_{0x} + u_{0x} B_{1y} \\
qB_{1z} &= ik (u_{1z} B_{0x} - u_{0x} B_{1z})
\end{aligned} \tag{A.9}$$

Putting the y components of u_{1y} and B_{1y} together we get two equations

$$\begin{aligned}\rho_0 (q + ik u_{0x}) u_{1y} &= \frac{1}{\mu_0} ik B_{0x} B_{1y} \\ (q + ik u_{0x}) B_{1y} &= ik u_{1y} B_{0x}\end{aligned}\tag{A.10}$$

which, when solving for q , yields

$$q = -ik u_{0x} \pm \left(\frac{B_{0x}^2}{\mu_0 \rho_0} \right)^{\frac{1}{2}}.\tag{A.11}$$

The growth rate does not depend on perturbations of the y components. Continuing with the x and z components, eliminating all y dependencies:

$$\begin{aligned}\rho_0 q u_{1x} &= -\rho_0 u_{1z} \partial_z u_{0x} - ik \rho_0 u_{0x} u_{1x} - ik p_1 \\ \rho_0 u_{1z} &= -ik \rho_0 u_{0x} u_{1z} - \partial_z p_1 - \frac{1}{\mu_0} B_{0x} (\partial_z B_{1x} - ik B_{1z}) - \rho_1 g \\ q B_{1x} &= -\partial_z (u_{1z} B_{0x} - u_{0x} B_{1z}) \\ q B_{1z} &= ik (u_{1z} B_{0x} - u_{0x} B_{1z})\end{aligned}\tag{A.12}$$

We can add an additional simplification by assuming that there is no initial shear flow along x ($u_{0x} = 0$).

$$\begin{aligned}q \rho_1 &= -u_{1z} \partial_z \rho_0 \\ \rho_0 q u_{1x} &= -ik p_1 \\ \rho_0 q u_{1z} &= -\partial_z p_1 - \frac{1}{\mu_1} B_{0x} (\partial_z B_{1x} - ik B_{1z}) - \rho_1 g \\ q B_{1x} &= -B_{0x} \partial_z u_{1z} = B_{0x} ik u_{1x} \\ q B_{1z} &= B_{0x} ik u_{1z} \\ 0 &= ik u_{1x} + \partial_z u_{1z}\end{aligned}\tag{A.13}$$

We are interested in flows along z , so by making the various substitutions into the z component of the momentum equation we get:

$$\begin{aligned}
\rho_0 q u_{1z} &= -\partial_z \frac{\rho_0 q u_{1x}}{-ik} - \frac{B_{0x}}{\mu_0} \left(\partial_z \frac{B_{0x} i k u_{1x}}{q} - i k \frac{B_{0x} i k u_{1z}}{q} \right) + g \frac{u_{1z} \partial_z \rho_0}{q} \\
&= -\partial_z \frac{\rho_0 q \partial_z u_{1z}}{-(ik)^2} - \frac{B_{0x}}{\mu_0} \left(\partial_z \frac{B_{0x} \partial_z u_{1z}}{q} + i k \frac{B_{0x} i k u_{1z}}{q} \right) + g \frac{u_{1z} \partial_z \rho_0}{q} \\
k^2 \rho_0 u_{1z} &= \partial_z (\rho_0 \partial_z u_{1z}) + \frac{k^2 B_{0x}^2}{q^2 \mu_0} (\partial_z^2 u_{1z} - k^2 u_{1z}) + \frac{g k^2}{q^2} (\partial_z \rho_0) u_{1z}
\end{aligned} \tag{A.14}$$

From these we get the governing equation:

$$\partial_z (\rho_0 \partial_z u_{1z}) + \frac{k^2 B_{0x}^2}{q^2 \mu_0} (\partial_z^2 u_{1z} - k^2 u_{1z}) - k^2 \rho_0 u_{1z} = -\frac{g k^2}{q^2} (\partial_z \rho_0) u_{1z} \tag{A.15}$$

Now we solve for the growth rate by integrating this equation over the discontinuity in ρ , from $-\epsilon$ to $+\epsilon$.

$$\int_{-\epsilon}^{\epsilon} \partial_z (\rho_0 \partial_z u_{1z}) dz + \frac{k^2 B_{0y}^2}{q^2 \mu_0} \int_{-\epsilon}^{\epsilon} (\partial_z^2 u_{1z} - k^2 u_{1z}) dz - k^2 \int_{-\epsilon}^{\epsilon} \rho_0 u_{1z} dz = -\frac{g k^2}{q^2} \int_{-\epsilon}^{\epsilon} (\partial_z \rho_0) u_{1z} dz \tag{A.16}$$

Simplify each term individually using the surface wave approximation, $u_{1z} = a \exp(-k|z|)$.

For the first term we get:

$$\int_{-\epsilon}^{\epsilon} \partial_z (\rho_0 \partial_z u_{1z}) dz = [\rho_0 \partial_z u_{1z}]_{-\epsilon}^{\epsilon} = -\rho_{02} k a e^{-k\epsilon} - \rho_{01} k a e^{-k\epsilon} \tag{A.17}$$

Second term:

$$\begin{aligned}
\int_{-\epsilon}^{\epsilon} (\partial_z^2 u_{1z} - k^2 u_{1z}) dz &= \int_{-\epsilon}^{\epsilon} \partial_z^2 u_{1z} dz - k^2 \int_{-\epsilon}^{\epsilon} u_{1z} dz \\
&= [\partial_z u_{1z}]_{-\epsilon}^{\epsilon} - k^2 \left[\int_{-\epsilon}^0 u_{1z} dz + \int_0^{\epsilon} u_{1z} dz \right] \\
&= -2ak e^{-k\epsilon} - k^2 \left(\frac{2a}{k} - \frac{2a}{k} e^{-k\epsilon} \right) = -2ak
\end{aligned} \tag{A.18}$$

Third term:

$$\begin{aligned}
\int_{-\epsilon}^{\epsilon} \rho_0 u_{1z} dz &= \int_{-\epsilon}^0 \rho_0 u_{1z} dz + \int_0^{\epsilon} \rho_0 u_{1z} dz \\
&= \frac{\rho_{01} a}{k} (1 - e^{-k\epsilon}) - \frac{\rho_{02} a}{k} (e^{-k\epsilon} - 1) \\
&= \frac{\rho_{01} a}{k} + \frac{\rho_{02} a}{k} - \left(\frac{\rho_{01} a}{k} + \frac{\rho_{02} a}{k} \right) e^{-k\epsilon}
\end{aligned} \tag{A.19}$$

Right side term:

$$\begin{aligned}
\int_{-\epsilon}^{\epsilon} (\partial_z \rho_0) u_{1z} dz &= [u_{1z} \rho_0]_{-\epsilon}^{\epsilon} - \int_{-\epsilon}^{\epsilon} \rho_0 \partial_z u_{1z} dz \\
&= (\rho_{02} - \rho_{01}) a e^{-k\epsilon} - [\rho_{01} a (1 - e^{-k\epsilon}) + \rho_{02} a (e^{-k\epsilon} - 1)] \\
&= (\rho_{02} - \rho_{01}) a
\end{aligned} \tag{A.20}$$

Combining all the terms:

$$\begin{aligned}
&-ka(\rho_{01} + \rho_{02})e^{-k\epsilon} + \frac{k^2 B_{0y}^2}{q^2 \mu_0} (-2ka) \\
&-k^2 \left(\frac{\rho_{01} a}{k} + \frac{\rho_{02} a}{k} - \left(\frac{\rho_{01} a}{k} + \frac{\rho_{02} a}{k} \right) e^{-k\epsilon} \right) = -\frac{gk^2}{q^2} (\rho_{02} - \rho_{01}) a
\end{aligned} \tag{A.21}$$

Now let $\epsilon \rightarrow 0$:

$$-ka(\rho_{02} + \rho_{01}) + \frac{k^2 B_{0y}^2}{q^2 \mu_0} (-2ka) = -\frac{gk^2}{q^2} (\rho_{02} - \rho_{01}) a \tag{A.22}$$

and solve for q .

$$q^2 = gk \frac{\rho_2 - \rho_1}{\rho_2 + \rho_1} - \frac{2(k_y B_y)^2}{\mu_0 (\rho_1 + \rho_2)} \tag{A.23}$$

Growth rate is dependent on the wavenumber k as well as the the severity of the density gradient. Large k_{\perp} increase the growth rate of the instability, while parallel wavelengths suppress growth. The ratio $\frac{\rho_2 - \rho_1}{\rho_2 + \rho_1}$, known as the Atwood number, increases growth.

Appendix B: Derivation of the Dispersion Relationship for Alfvén Waves

To find the dispersion relationship for Alfvén waves in plasma conditions similar to those in the giant magnetospheres, we model the plasma as fluid waves with two species: electrons, and ions (subscript s will denote a single species). We start with continuity and momentum equations, and close with Maxwell's equations to get the following system:

$$\begin{aligned}
 \frac{\partial n_s}{\partial t} + \nabla \cdot (n \mathbf{u}_s) &= 0 \\
 m_s n \left(\frac{\partial \mathbf{u}_s}{\partial t} + \mathbf{u}_s \cdot \nabla \mathbf{u}_s \right) &= -\nabla p_s + q_s n (\mathbf{E} + \mathbf{u}_s \times \mathbf{B}) \\
 \nabla \times \mathbf{B} - \frac{1}{c^2} \frac{\partial \mathbf{E}}{\partial t} &= \mu_0 n e (\mathbf{u}_i - \mathbf{u}_e) \\
 \nabla \times \mathbf{E} + \frac{\partial \mathbf{B}}{\partial t} &= 0
 \end{aligned} \tag{B.1}$$

A very important aspect of dispersive Alfvén waves is parallel electric fields. We will introduce the parallel electric field as a combination of scalar and vector potentials:

$$\mathbf{E} = -\nabla \phi - \frac{\partial A_z}{\partial t} \hat{\mathbf{z}} \tag{B.2}$$

where the perpendicular magnetic perturbation is $\mathbf{B}_\perp = \nabla A_z(x, y) \times \hat{\mathbf{z}}$. We do not assume perturbations in the parallel component of B due to the low plasma- β assumption. We then separate the components of the electric field:

$$\begin{aligned}
 \mathbf{E}_\perp &= \nabla_\perp \phi \\
 E_\parallel &= -\frac{\partial \phi}{\partial z} - \frac{\partial A_z}{\partial t}
 \end{aligned} \tag{B.3}$$

From Maxwell's equations we derive an expression for the current in terms of the vector potential:

$$\begin{aligned}\mu_0 \mathbf{J}_\perp &= \nabla_\perp \frac{\partial A_z}{\partial z} \\ \mu_0 \mathbf{J}_\parallel &= -\nabla_\perp^2 A_z\end{aligned}\tag{B.4}$$

For very extremely low β plasmas (where $\beta \ll m_e/m_i$), electron inertial effects dominate. Electron acceleration along the field line is a response to the parallel electric field. We will assume that the parallel current is carried by the electrons, such that $J_\parallel = nq_e u_{e\parallel}$, and that the perpendicular current is carried by polarization drift ($\mathbf{J}_\perp = nq_s \mathbf{u}_i = \frac{nm_i}{B_0^2} \frac{d\mathbf{E}_\perp}{dt}$). We then obtain

$$\begin{aligned}\frac{m_e}{nq_e} \frac{\partial J_\parallel}{\partial t} &= -q_e \left(\frac{\partial \phi}{\partial z} + \frac{\partial A_z}{\partial t} \right) \\ -\frac{1}{\mu_0} \frac{m_e}{nq - e^2} \nabla_\perp^2 \frac{\partial A_z}{\partial t} &= -\frac{\partial \phi}{\partial z} - \frac{\partial A_z}{\partial t} \\ \left(1 - \frac{1}{\mu_0 \epsilon_0} \frac{\epsilon_0 m_e}{nq_e^2} \nabla_\perp^2 \right) \frac{\partial A_z}{\partial t} &= -\frac{\partial \phi}{\partial z} \\ \left(1 - \frac{c^2}{\omega_{pe}^2} \nabla_\perp^2 \right) \frac{\partial A_z}{\partial t} &= -\frac{\partial \phi}{\partial z} \\ (1 - \lambda_e^2 \nabla_\perp^2) \frac{\partial A_z}{\partial t} &= -\frac{\partial \phi}{\partial z}\end{aligned}\tag{B.5}$$

where λ_e is the electron skin depth. Now combine the earlier equations:

$$\begin{aligned}\mathbf{J}_\perp &= nq_s \mathbf{u}_i = \frac{nm_i}{B_0^2} \frac{d\mathbf{E}_\perp}{dt} \\ \mathbf{E}_\perp &= -\nabla_\perp \phi \\ \mu_0 \mathbf{J}_\perp &= \nabla_\perp \frac{\partial A_z}{\partial z}\end{aligned}\tag{B.6}$$

which leads to

$$\begin{aligned}\frac{1}{\mu_0} \frac{\partial A_z}{\partial z} &= - \frac{nm_i}{B_0^2} \nabla_{\perp} \frac{d\phi}{dt} \\ \nabla_{\perp} \frac{\partial A_z}{\partial z} &= - \frac{1}{v_A^2} \nabla_{\perp} \frac{d\phi}{dt}\end{aligned}\tag{B.7}$$

For the polarization drift, we can substitute the full derivative of ϕ with $\frac{d\phi}{dt} = \frac{\partial\phi}{\partial t} + \mathbf{u}_E \cdot \nabla\phi$.

$$\begin{aligned}\nabla_{\perp} \frac{\partial A_z}{\partial z} &= - \frac{1}{v_A^2} \nabla_{\perp} \left[\frac{\partial\phi}{\partial t} + (\mathbf{u}_E \cdot \nabla_{\perp}) \phi \right] \\ &= - \frac{1}{v_A^2} \nabla_{\perp} \left[\frac{\partial\phi}{\partial t} - \mathbf{u}_E \cdot \nabla \right] \phi \\ \frac{\partial A_z}{\partial z} &= - \frac{1}{v_A^2} \frac{\partial\phi}{\partial t}\end{aligned}\tag{B.8}$$

Taking a time derivative of Equation B.5 yields

$$\left(1 - \lambda_e \nabla_{\perp}^2\right) \frac{\partial^2 A_z}{\partial t^2} = - \frac{\partial\phi}{\partial z}\tag{B.9}$$

which is combined with Equation B.8 to get the equation for the inertial Alfvén wave:

$$\left(1 - \lambda_e^2 \nabla_{\perp}^2\right) \frac{\partial^2 A_z}{\partial t^2} = v_A^2 \frac{\partial^2 A_z}{\partial z^2}\tag{B.10}$$

If we then assume plane wave solutions, we can solve for the dispersion relation:

$$\omega^2 = \frac{k_{\parallel}^2 v_A^2}{1 + k_{\perp}^2 \lambda_e^2}\tag{B.11}$$

Dispersion from the main Alfvén wave ($\omega/k = v_A$), only occurs for low β plasmas ($\beta < m_e/m_i$) and where k_{\perp} is very large [Stix, 1992; Swanson, 1989]. These plasma conditions are not met in the magnetodisc or equatorial regions of the magnetospheres of the giant planets, so they have little influence in electron acceleration near where the waves are generated. Instead, they become relevant at high latitude, where the plasma is more rarefied, and

wavelengths are shortened due to the turbulent cascade and convergence of magnetic field lines.

To find the dispersion relationship for Alfvén waves in the magnetodisc, we consider the limiting case in a low β plasma, but β is still larger than the electron to ion mass ratio. We also assume that the Alfvén speed is much slower than the electron thermal speed, and that the effect of electron inertia is negligible. Any arising parallel electric fields are a result of electron pressure gradients. The parallel electric field is then

$$E_{\parallel} = -\frac{T_e}{en_0} \frac{\partial n_{e1}}{\partial z} = -e\mu_0\rho_s^2 v_A^2 \frac{\partial n_{e1}}{\partial z} \quad (\text{B.12})$$

where T_e is electron temperature, and ρ_s is the ion acoustic gyroradius ($\rho_s = c_s/\Omega_i$, and c_s is the sound speed $(T_e/m_i)^{1/2}$). We combine it with Equation B.3 to get

$$e\mu_0\rho_s^2 v_A^2 \frac{\partial n_{e1}}{\partial z} = \frac{\partial A_z}{\partial t} + \frac{\partial \phi}{\partial z} \quad (\text{B.13})$$

With the continuity equation ($\frac{\partial n_0}{\partial t} + \nabla \cdot (n_0 \mathbf{u}_e) = 0$) and the expression for parallel current above (Equation B.4), we obtain

$$\frac{\partial n_{e1}}{\partial t} + \frac{1}{e\mu_0} \frac{\partial}{\partial z} \nabla_{\perp}^2 A_z = 0. \quad (\text{B.14})$$

Combining the above two equations yields

$$\frac{\partial^2 A_z}{\partial t^2} - \frac{\partial}{\partial z} v_A^2 \frac{\partial A_z}{\partial z} + v_A^2 \rho_s^2 \nabla_{\perp}^2 \frac{\partial^2 A_z}{\partial z^2} = 0. \quad (\text{B.15})$$

We again assume plane wave solutions and get the following dispersion relationship:

$$\omega = k_{\parallel} v_A \left(1 + k_{\perp}^2 \rho_s^2\right)^{1/2} \quad (\text{B.16})$$

It is often more useful to consider the dispersion relationship in terms of electron and ion

temperature. *Hasegawa* [1976]; *Lysak and Lotko* [1996] derive the dispersion relationship from the dielectric tensor and get

$$\omega^2 = k_{\parallel}^2 v_A^2 \left[1 + k_{\perp}^2 \rho_i^2 \left(\frac{3}{4} + \frac{T_e}{T_i} \right) \right], \quad (\text{B.17})$$

which is relevant for when $\text{plasma-}\beta > m_e/m_i$. Kinetic Alfvén waves have a larger phase velocity with a greater electron temperature. Also, a larger k_{\perp} is responsible for dispersion from the non-dispersive Alfvén wave.

To find the dispersion relationship for a small ($\sim \lambda_i$) parallel propagating Alfvénic perturbation in a cold incompressible plasma, we need to add the Hall term to the magnetic induction equation (for the generalized Ohm's law, we use the following terms: $\mathbf{E} = -\mathbf{u} \times \mathbf{B} + \frac{1}{nq} \mathbf{J} \times \mathbf{B}$). We assume that $\mathbf{B} = B_0 \hat{\mathbf{z}}$ and $\mathbf{k} = k \hat{\mathbf{z}}$. First, linearize the MHD equations to obtain

$$\begin{aligned} \rho &= \rho_0 + \rho_1 \\ \mathbf{u} &= \mathbf{u}_1 \\ \mathbf{B} &= B_0 \hat{\mathbf{z}} + \mathbf{B}_1 \\ \rho_0 \frac{\partial \mathbf{u}_1}{\partial t} &= \frac{\nabla \times \mathbf{B}_1}{\mu_0} \times B_0 \hat{\mathbf{z}} \end{aligned} \quad (\text{B.18})$$

Assume plane wave solutions, and we obtain the following for the last equation:

$$-i\omega \tilde{\mathbf{u}}_1 = B_0 \frac{i\mathbf{k} \times \mathbf{B}_1}{\mu_0 \rho_0} \times \hat{\mathbf{z}} \quad (\text{B.19})$$

Then solve for $\tilde{\mathbf{u}}_1$:

$$\tilde{\mathbf{u}}_1 = - \left(\frac{k B_0}{\mu_0 \rho_0 \omega} \right) \tilde{B}_{1x} \hat{\mathbf{x}} - \left(\frac{k B_0}{\mu_0 \rho_0 \omega} \right) \tilde{B}_{1y} \hat{\mathbf{y}} \quad (\text{B.20})$$

Now take Faraday's law with the Hall term

$$\frac{\partial \mathbf{B}_1}{\partial t} = -\nabla \times \left[\left(\frac{\nabla \times \mathbf{B}_1}{\mu_0 nq} - \mathbf{u}_1 \right) \times B_0 \hat{\mathbf{z}} \right] \quad (\text{B.21})$$

and linearize it to obtain component solutions:

$$\begin{aligned}
-i\omega\tilde{\mathbf{B}}_1 &= -\left(\frac{ik^2B_0^2}{\mu_0\rho_0\omega}\tilde{B}_{1x} + \frac{k^2B_0}{\mu_0nq}\tilde{B}_{1y}\right)\hat{\mathbf{x}} + \left(\frac{k^2B_0}{\mu_0nq}\tilde{B}_{1x} - \frac{ik^2B_0^2}{\mu_0\rho_0\omega}\tilde{B}_{1y}\right)\hat{\mathbf{y}} \\
-i\omega\tilde{\mathbf{B}}_1 &= -\left(\frac{ik^2v_A^2}{\omega}\tilde{B}_{1x} + \frac{k^2\Omega_i c^2}{\omega_{pi}^2}\tilde{B}_{1y}\right)\hat{\mathbf{x}} + \left(\frac{k^2\Omega_i c^2}{\omega_{pi}^2}\tilde{B}_{1x} - \frac{ik^2v_A^2}{\omega}\tilde{B}_{1y}\right)\hat{\mathbf{y}}
\end{aligned} \tag{B.22}$$

where v_A is the Alfvén velocity, ω_{pi} is the plasma frequency, and Ω_i is the ion gyrofrequency.

We now introduce a parameter $\lambda_i = \frac{c}{\omega_{pi}}$, the ion inertial length, which is a characteristic length for ion kinetic scales. We can rewrite the above equation in matrix form to get

$$\begin{pmatrix} -i\omega + \frac{ik^2v_A^2}{\omega} & k^2\Omega_i\lambda_i^2 \\ -k^2\Omega_i\lambda_i^2 & -i\omega + \frac{ik^2v_A^2}{\omega} \end{pmatrix} \begin{pmatrix} \tilde{B}_{1x} \\ \tilde{B}_{1y} \end{pmatrix} = 0. \tag{B.23}$$

Solving the matrix ($\det \mathbf{M} = 0$), we find that

$$\begin{aligned}
\frac{\omega^4}{k^4} - 2v_A^2\frac{\omega^2}{k^2} + v_A^4 &= (\Omega_i\lambda_i^2)^2\omega^2 \\
\left[\left(\frac{\omega}{k}\right)^2 - v_A^2\right]^2 &= (\Omega_i\lambda_i^2)^2\omega^2 \\
\left(\frac{\omega}{k}\right)^2 &= v_A^2 \pm \Omega_i\lambda_i^2\omega
\end{aligned} \tag{B.24}$$

From this we see the dispersion from the main Alfvén wave, with (+) being associated with the faster whistler mode, and (-) with the slower ion whistler mode. The whistler mode is right hand circularly polarized and the ion whistler mode is left hand circularly polarized. The change in polarization happens at $\omega/k = v_A$, the Alfvén resonance [Stix, 1992].

Appendix C: Hybrid Code Algorithms

The electric fields in the hybrid code are determined from a simplification of Ohm's law (or electron momentum equation with no inertia), given by

$$\mathbf{E} = -\mathbf{u}_e \times \mathbf{B} - \nu (\mathbf{u}_e - \mathbf{u}_i) \quad (\text{C.1})$$

where ν is a resistive ion-electron collision term, r is the electron to ion mass ratio, and \mathbf{u}_e and \mathbf{u}_i are the electron and ion velocities respectively. Electron flow speed is calculated from Ampere's law:

$$\mathbf{u}_e = \mathbf{u}_i - \frac{\nabla \times \mathbf{B}_1}{wn} \quad (\text{C.2})$$

where w is the ion weighting parameter and n is the local density. Individual ion motion is determined by the Lorentz force law to get an equation of motion:

$$\frac{d\mathbf{v}_i}{dt} = \mathbf{E} + \mathbf{v} \times \mathbf{B}. \quad (\text{C.3})$$

The time stepping scheme is accomplished in two primary parts. Motion of the ions are updated in one time step, while all the fluid and field quantities are updated on a subcycle δt that is a tenth of a normal time step (dt). Figure C.1 is a flowchart that shows the update of the ions and fields.

Ion velocities are generally initialized with a Maxwellian distribution whose width depends on temperature, or thermal velocity of the ions. An easy model for a two-dimensional initial Maxwellian is given by

$$v_i = v_{th} \sqrt{-\ln(r_1) \cos(\pi r_2)} \quad (\text{C.4})$$

where v_i is a component of ion velocity, v_{th} is the thermal velocity of the ions, and r_1, r_2 are random numbers between 0 and 1. This equation is extended to the three-dimensional

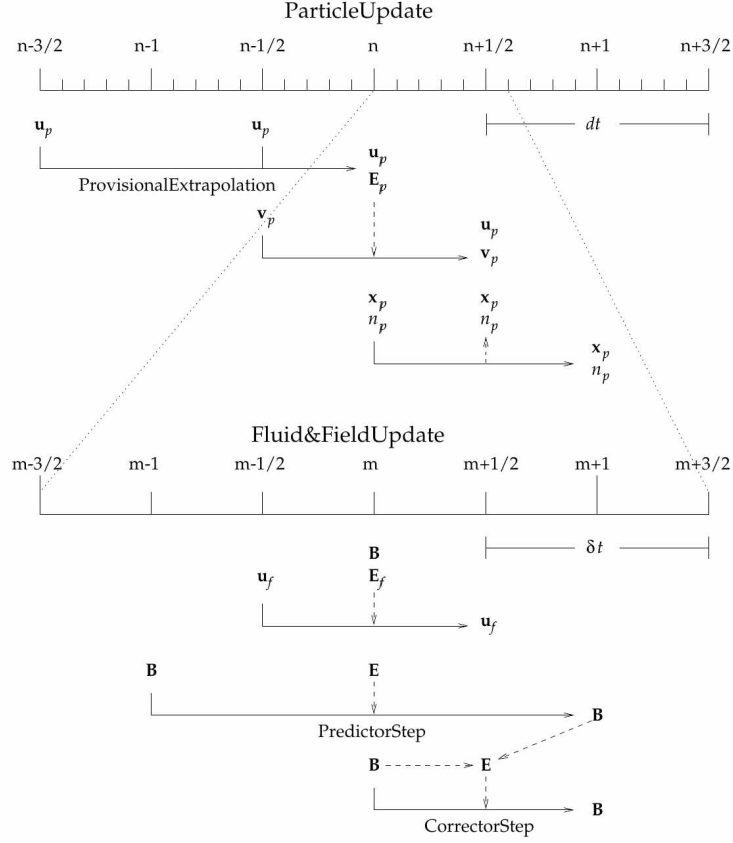


Figure C.1: The time stepping algorithm. A summary of the time stepping algorithm showing the temporal relationship between particle, fluid and field variables. The particle positions (densities) at the half time step, $n+1/2$, are used to update the fluid and field quantities (on the subcycle time step) from time level n to $n+1$. The subcycle time step, δt , is $dt/10$. From *Delamere* [1998].

case as well. The update to the ion motion must be made so that energy of the particle is conserved. A normal first-order approximation for ion motion using a routine such as the Euler method results in ion heating, as the gyroradius gradually increases. Second-order schemes reduce the error enough for the ion motion to be stable for a longer period, but still results in heating. Instead, we use an update algorithm proposed in *Boris* [1970] that calculates half time step velocity updates so that the guiding center of the ion gyromotion is followed, and the ions maintain their temperature indefinitely. We introduce new variables

$$\mathbf{v}^{\pm} = \mathbf{v}^{n \pm \frac{1}{2}} \mp \frac{\Delta t}{2} \mathbf{E}^n \quad (\text{C.5})$$

where

$$\mathbf{v}^n = \frac{1}{2}(\mathbf{v}^+ + \mathbf{v}^-).$$

Substitute this into the discretized form of the Lorentz force equation to get

$$\frac{\mathbf{v}^{n+1/2} - \mathbf{v}^{n-1/2}}{\Delta t} = \mathbf{E}^n + \mathbf{v}^n \times \mathbf{B}^n. \quad (\text{C.6})$$

where the factor q/m is included in the electric and magnetic field: $\mathbf{E} \rightarrow \frac{q}{m} \mathbf{E}$. This leads to

$$(\mathbf{v}^+ + \frac{\Delta t}{2} \mathbf{E}^n) - (\mathbf{v}^- - \frac{\Delta t}{2} \mathbf{E}^n) = \Delta t \mathbf{E}^n + \Delta t (\mathbf{v}^n \times \mathbf{B}^n) \quad (\text{C.7})$$

$$\mathbf{v}^+ = \mathbf{v}^- + \frac{\Delta t}{2} (\mathbf{v}^+ + \mathbf{v}^-) \times \mathbf{B}^n \quad (\text{C.8})$$

We need to get an explicit expression for \mathbf{v}^+ , that is not dependent on \mathbf{E} . Manipulating the equation, we get a value for \mathbf{v}^+ :

$$\left[1 + \frac{(B^2)^n \Delta t^2}{4}\right] \mathbf{v}^+ = \left[1 - \frac{(B^2)^n \Delta t^2}{4}\right] \mathbf{v}^- + \Delta t (\mathbf{v}^- \times \mathbf{B}) + \frac{\Delta t^2}{2} (\mathbf{v}^- \cdot \mathbf{B}) \mathbf{B} \quad (\text{C.9})$$

Using \mathbf{v}^+ , we can now solve for the advanced time step:

$$\mathbf{v}^{n+1/2} = \mathbf{v}^+ + \frac{\Delta t}{2} \mathbf{E}^n \quad (\text{C.10})$$

Defining \mathbf{v}^\pm eliminates the electric field, so that the ion motion is done in the rest frame of the plasma. Ion motion is just a rotation in that frame. This allows resolution of the ion gyromotion and avoids heating the ions from propagating numerical errors [*Birdsall and Langdon*, 1985].

The technique for performing vector operations on a field grid is described in *Yee* [1966] and *Swift* [1996], and shown in Figure C.2. The main difficulty is enforcing the non-divergence of the magnetic field ($\nabla \cdot \mathbf{B} = 0$) on the grid. To overcome this, two cells are modeled: the main cell and the dual cell. The main cell is at the grid point (i, j, k) and the center of the dual cell is at the main cell corner $(i + \frac{1}{2}, j + \frac{1}{2}, k + \frac{1}{2})$. The electric field components are defined on the main cell faces, and the magnetic field components are defined on the main cell edges (or dual cell faces). All other vector quantities are defined on the main cell faces. We can then advance the magnetic field update by applying Stoke's theorem to Faraday's law

$$\int \frac{\partial \mathbf{B}}{\partial t} \cdot d\mathbf{A} = \oint \mathbf{E} \cdot d\mathbf{l}. \quad (\text{C.11})$$

Field equations must be interpolated to the dual cell grid points and then the appropriate curl operations can be performed to maintain closure of the field equations. This only works if the magnetic field is initialized such that there is no divergence.

Finally, the particle-in-cell algorithm must interpolate the values of field quantities from the grid points to the ions. In reverse, ion motion must be aggregated and integrated to determine their macroscale statistical properties onto the grid [*Potter*, 1977]. Figure C.3 illustrates the interpolation of grid properties to an ion at point P . The eight nearest grid points are used for the interpolation. The weighting of each grid point is just the ratio of the subvolume of the opposite corner of the cell to the whole volume of the cell.

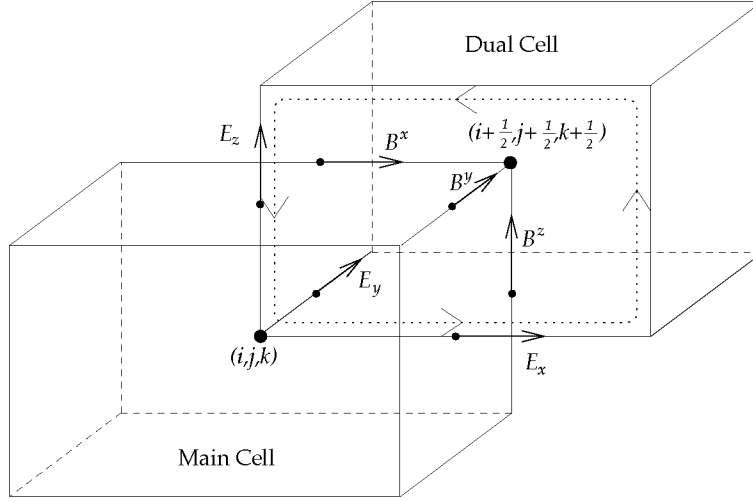


Figure C.2: The coordinate dual cell. The coordinate cell showing the relationship between the main and dual cells, and the components of the electric and magnetic fields. The dotted line illustrates the line integral used for the advancement of B_y [Yee, 1966]. Figure by *Delamere* [1998].

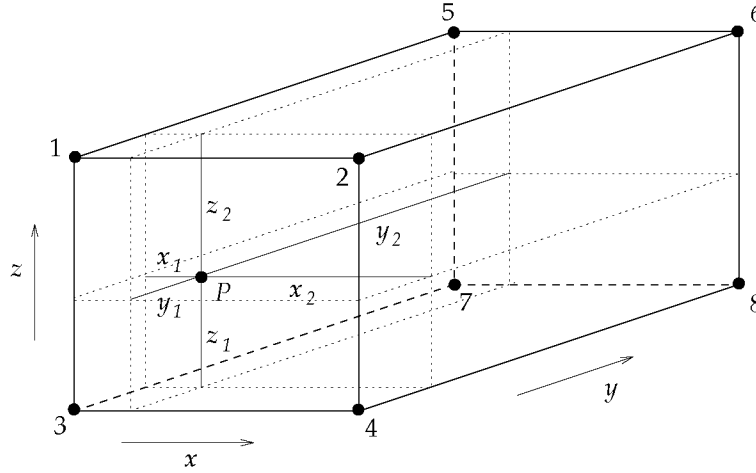


Figure C.3: Particle-in-cell weighting. An illustration of the particle-in-cell weighting algorithm for interpolating fluid and field quantities to the particle positions and particle densities of the grid positions. The normalized weight for each grid point is the subvolume of the opposite corner of the cell divided by the cell volume [Delamere, 1998].

Appendix D: Updates to the Hybrid Code

Following are a number of major improvements made from an inherited version of the hybrid code. Creation of the hybrid code was based off of a template from the SWAP version of the code, designed to model the response of New Horizon’s SWAP instrument in Pluto’s environment. The following segments of code that contain parts of subroutines omit the specification section for brevity.

The first major adjustment is the complete rewriting of the code syntax from Fortran70 to Fortran90. The main reason for doing so is an update to bring the code into alignment with current programming best practices. Some examples include proper looping and branching (elimination of the *goto* command, implementing blocking of code, and optimizing for parallel processing), eliminating global variables in favor of improving the scope of variable arrays, and rigorous specification sections to prevent memory loss. The greatest advantage gained here is modularization of the code, making modification of the code for specific applications easier. For example, all particle initialization routines are now contained within one module. Any new scenario can be loaded by specifying a new routine within the module, and passing it to the main program. Boundary conditions are also modularized, allowing users to easily choose between a few different options from the input file, instead of having to block out many sections of code across many files to have the same effect. Adding new boundary conditions would require major revisions to one file only. One major remaining weakness that we would like to see improved is the the ability to easily change the parallelization scheme. Currently the code only supports parallelization of particle updates. Domain decomposition of the grid is a useful feature that is not available in this version. Any domain decomposition has to rely on an earlier and less stable version of the code.

Particle initialization through random number generation is an important component to obtain good particle statistics. The PGI Fortran compiler on the Pacman cluster did not use separate seeds for each processor, essentially negating parallelization. The following code

was added to use two levels of seeding to ensure that each processor is generating separate sequences of numbers.

```

subroutine seed_mpi(my_rank)
  call random_seed(size=n)
  allocate(seed(n))
  ! First check to see if OS provides a random number
  open(newunit=un, file="/dev/urandom", access="stream", &
    form="unformatted", action="read", status="old", iostat)
  if(istat == 0) then
    read(un) seed
    close(un)
  else ! Fallback to using time and rank.
    call system_clock(t)
    if(t == 0) then
      call date_and_time(values=dt)
      t = dt(1) * 365_int64 * 24 * 60 * 60 * 1000 &
        + dt(2) * 31_int64 * 24 * 60 * 60 * 1000 &
        + dt(3) * 24_int64 * 60 * 60 * 1000 &
        + dt(5) * 60 * 60 * 1000 &
        + dt(6) * 60 * 1000 + dt(7) * 1000 &
        + dt(8)
    end if
  ! Use rank for low bits and time for high bits
  if(bit_size(my_rank) <= bit_size(t)) then
    t = my_rank + ishft(t, bit_size(my_rank))
  else
    t = ieor(t, int(my_rank, kind(t)))
  end if
  ! Here we're using a bad RNG to seed the better one.
  do i=1,n
    seed(i) = lcg(t)
  end do
end if
call random_seed(put=seed)

```

The parameter *beta_p* was added to particle initialization, which represents individual particle weights. Before, all ions had the same weighting. Individual particle weights permit variation in density without having to introduce additional ions. Each subroutine call that requires aggregation of ions to calculate momenta and density on the grid require this parameter. Shown is a part of the ion initialization from the 3D RT simulation.

```

! From part_init.f90
beta_p(1) = real(Ni_tot*ratio*procnum)/vol/ &
  (np_bottom*((1.0-tanh((xp(1,3)-qz(nz/2))/Lo))/2.0) )

```

This subroutine calculates an electron gradient pressure on the grid dependent on a temperature difference between ions and electrons. It adds another term to the electric field update, and allows the modeling of superthermal electrons.

```

subroutine get_gradP
  etemp = etemp0*11604.505  !eV to Kelvin
  do i=2,nx-1
    do j=2,ny-1
      do k=2,nz-1
        np1 = 0.5*(np(i+1,j,k)+np(i,j,k))
        gdnP = (np(i+1,j,k)-np(i,j,k))/dx_grid(i)
        a0 = kboltz*etemp/(mion*np1)
        gnpf(i,j,k,1) = a0*gdnP

        np1 = 0.5*(np(i,j+1,k)+np(i,j,k))
        gdnP = (np(i,j+1,k)-np(i,j,k))/dy_grid(j)
        a0 = kboltz*etemp/(mion*np1)
        gnpf(i,j,k,2) = a0*gdnP

        np1 = 0.5*(np(i,j,k+1)+np(i,j,k))
        gdnP = (np(i,j,k+1)-np(i,j,k))/dz_grid(k)
        a0 = kboltz*etemp/(mion*np1)
        gnpf(i,j,k,3) = a0*gdnP
      enddo
    enddo
  enddo
end subroutine get_gradP

! From subroutine get_E
gradPmf(1) = 0.5*(gradP(i,j,k,1) + gradP(i+1,j,k,1))
gradPmf(2) = 0.5*(gradP(i,j,k,2) + gradP(i,j+1,k,2))
gradPmf(3) = 0.5*(gradP(i,j,k,3) + gradP(i,j,k+1,3))
do m =1,2
  E(i,j,k,m) = c(i,j,k,m) - gradPmf(m)
enddo

```

Boundary conditions are no longer limited to being periodic. These few routines keep the x and y field boundaries periodic, but change the condition on z . Ions that leave the z

domain are reinitialized randomly in x and y , but remain near the z boundary. v_z is also reversed.

```

! From subroutine periodic_xy
do i=1,nx
  do k=1,nz
    do m=1,3
      b(i,1,k,m) = b(i,ny-1,k,m)
      b(i,ny,k,m) = b(i,2,k,m)
    enddo
  enddo
enddo

! Z direction is not periodic
do i=1,nx
  do j=1,ny
    do m=1,3
      b(i,j,nz,m) = b(i,j,nz-1,m)
      b(i,j,1,m) = b(i,j,2,m)
    enddo
  enddo
enddo

! From subroutine particle_boundary
! Particles that exceed z-domain are reinserted
do l=1,Ni_tot
  if (xp(l,3) .le. qz(1)) then
    vp(l,3) = -vp(l,3)
    xp(l,1) = qx(1)+(1.0-pad_ranf())*(qx(nx-1)-qx(1))
    xp(l,2) = qy(1)+(1.0-pad_ranf())*(qy(ny-1)-qy(1))
    xp(l,3) = qz(1)+(qz(1) - xp(l,3))
  else if (xp(l,3) .ge. qz(nz)) then
    vp(l,3) = -vp(l,3)
    xp(l,1) = qx(1)+(1.0-pad_ranf())*(qx(nx-1)-qx(1))
    xp(l,2) = qy(1)+(1.0-pad_ranf())*(qy(ny-1)-qy(1))
    xp(l,3) = qz(nz)-(xp(l,3) - qz(nz))
  endif
enddo

```

An array representing a gravitational field has been added to the particle initialization. More accurately, it can be used to model any external force that does not have time dependence. The *grav* array is initialized in units of acceleration (km s^{-2}), and added as a

component of the electric field update.

```
! From particle initialization routine.
do i=1,nx
  do j=1,ny
    grav(i,j,:)=-grav0*(tanh((qz(:)-qz(nz/2) &
      - 120*delz)/(30*delz)) - &
      tanh((qz(:)-qz(nz/2)+120*delz)/(30*delz)))
  enddo
enddo
! from get_E
E(i,j,k,3) = c(i,j,k,3) + gravc(i,j,k)
```

Each time step it is necessary to sort each ion into its respective grid cell so that the fields can be updated. The most computationally intensive subroutines are *get_E* and *get_Ep*, which rely on this sorting. The subroutine was improved by replacing the linear search algorithm with a binary search algorithm. The time spent on the search routine is improved from $O(n)$ to $O(\log n)$. Only the algorithm for the search in the x domain is shown.

```
! From subroutine get_pindex
i=1
hi = nx
do
  mid = (i+hi)/2
  if (xp(1,1) .lt. qx(mid)) then
    hi=mid
  else
    i=mid
  endif
  if (i+1 .ge. hi) exit
enddo
ijkp(1,1)=i
```

The following routine adds mass loading to the chemical interactions module. It directly adds additional components to the xp , vp , and weighting arrays each time step which adds additional ions to the domain. The bottom loop calculates the momentum and energy added by each particle so that the simulation can keep track of the total energy and momentum in the domain. After that, the density and bulk velocity on the grid are recalculated.

```
subroutine Mass_load_Io(m_tstep)
```

```

! Mass load Io with ions
m_pu1=m1
! Mass loading scaled in time
if ((m_tstep .gt. 20) .and. (m_tstep .lt. 6000)) then
  scal = exp(-real(m_tstep-4000)**2/2000.0**2)
  ! Rate dependent on interaction cross section
  mdot = scal*sqrt(mion*nf_init*amp/mu0/1e9)* &
    b0_init*dx*dy*1e6
  dNi = 2
  if (my_rank .eq. 0) then
    write(*,*) 'mdot_(kg/s),_dNi...',mdot,dNi
  endif
  calculate weighting parameter beta_p
  beta_pu_over_m = procnum*real(dNi)*amu/(mdot*dt)
  if (Ni_max - Ni_tot .gt. dNi) then
    l1 = Ni_tot + 1
    do l= l1, l1+ dNi-1
      beta_p(l) = beta_pu_over_m*m_pu1
      m_arr(l) = m_pu1*amu
      mrat(l) = ion_amu/m_pu1
      theta2 = pad_ranf()*2*PI
      ! Initialize a ring beam distribution
      vp(1,1) = vsw*cos(theta2)
      vp(1,2) = vsw*sin(theta2)
      vp(1,3) = 0.0
      ! Initialize ion position
      xp(1,1) = qx(1)+(1.0-pad_ranf()*(qx(nx-1)-qx(1)))
      xp(1,2) = qy(1)+(1.0-pad_ranf()*(qy(ny-1)-qy(1)))
      flg=0
      do while (flg .eq. 0)
        xp(1,3) = qz(nz/2-100) + (1.0-pad_ranf()) &
          *(qz(nz/2+100)-qz(nz/2-100))
        rand1=pad_ranf()
        if (exp(-(xp(1,3)-qz(nz/2))**2/ &
          (10*dz_grid(nz/2)**2)) .gt. rand1) then
          flg = 1
        endif
      enddo
      flg=0
      ! find ion grid cell
      call get_pindex(i,j,k,l)
      ! Add ion energy and momentum to global counter
      do m=1,3
        vp1(1,m) = vp(1,m)
        input_E = input_E + 0.5*m_arr(l)* &

```

```

        (vp(1,m)*km_to_m)**2/(beta*beta_p(1))
input_p(m) = input_p(m) + m_arr(1)*vp(1,m)/ &
        (beta*beta_p(1))
    enddo
enddo
call MPI_BARRIER(MPI_COMM_WORLD,ierr)
Ni_tot = Ni_tot + dNi
call get_interp_weights()
call update_np()
call update_up(vp)
endif
endif
end subroutine Mass_load_Io

```

This routine keeps track of the number of particles in each cell across all processors. It is a good diagnostic to see if the initialized density profile is unstable, or parts of the grid are under-resolved. It is only useful when the number of particles per cell is non-uniform, and as such is normally disabled except for test runs.

```

subroutine count_ppc()
! Count the number of particles in each cell
count = nx*ny*nz
ppcpp_count(:,:,:) = 0.0
do l=1, Ni_tot
    i=ijkp(l,1)
    j=ijkp(l,2)
    k=ijkp(l,3)
    ppcpp_count(i,j,k) = ppcpp_count(i,j,k) + 1.0
enddo
! Add up all of the particles across processing units
call MPI_BARRIER(MPI_COMM_WORLD,ierr)
call MPI_ALLREDUCE(ppcpp_count(:,:,:),recvbuf,count, &
    MPI_REAL,MPI_SUM,MPI_COMM_WORLD,ierr)
ppcpp_count(:,:,:) = reshape(recvbuf,(/nx,ny,nz/))
! Write data
if (my_rank .eq. 0) then
    open(411,file=trim(out_dir)//'c.ppc.dat', &
        status='unknown',form='unformatted')
    write(411) j
    write(411) ppcpp_count
    close(411)
endif
end subroutine

```

```
end subroutine count_ppc
```

The supercomputing clusters have a walltime limit of 48 hours. If we need to run something longer than that, it is useful to have something that saves the progress of the simulation before it closes so that it can be restarted. This is also useful if we are not sure how long to run the simulation. These lines add restart ability by writing all the variables and arrays to disk. It also removes the restriction on the max default of 16 processing units. Now up to one hundred processing units can be used.

```
write(filenum, '(I2)') my_rank
! Check for restart flag
if (my_rank .eq. 0) write(*,*) 'restart_status...', restart
if ((restart) .and. (mstart_n .gt. 0)) then
write(*,*) 'opening_restart_vars....'
open(210,file=trim(out_dir)//'restart.vars',status='unknown', &
    form='unformatted')
write(*,*) 'reading_restart_vars.....'
read(210) b1,b12,b1p2,bt,btmf,btc,np,np3, &
    up,aj,nu,E,temp_p,mnp,beta,Evp,Euf, &
    EB1,EB1x,EB1y,EB1z,EE,EeP, &
    input_EeP,input_Eb,prev_Etot,bndry_Eflux,grav, &
    input_chex,input_bill
write(*,*) 'restarting_hybrid....'
open(211,file=trim(out_dir)//'restart.part'//trim(filenum), &
    status='unknown',form='unformatted')
read(211) vp,vp1,vplus,vminus,xp,Ep,input_E,Ni_tot,ijkp, &
    input_p,mrat,m_arr,beta_p
close(210)
close(211)
```

Variables are only outputted in an interval specified by the input file. For high resolution data for a Fourier transform, we need field data every time step. These few lines bypass the normal loop that outputs data and instead performs the output every time-step for the field at a specified grid point.

```
open(401, file = trim(out_dir)//'fft.dat',status='unknown', &
    form='unformatted')

write(401) dt,nt,omega_p
write(401) b1(2,2,loc,1), b1(2,2,loc,2), b1(2,2,loc,3)
```


Though we can output output velocity and particle distributions for everything in the grid, saving that data is hazardous to disk storage if we want to see the evolution of the distributions in time. This subroutine keeps the velocity distribution calculation in-house by outputting the reduced data to disk. The following subroutine specifically limits its search to velocities $< \pm 80 \text{ km s}^{-1}$. We separate them into two ion populations: the initial ions and the mass loaded ions.

```

subroutine get_v_dist()
  ! Set bounds for velocity (km/s)
  vxb=-80
  vxe=80
  vyb=-80
  vye=80
  vzb=-80
  vze=80
  count = (-vxb+vxe+1)*(-vyb+vye+1)
  allocate(recvbuf(count))
  vdist_init(:, :) = 0
  vdist_add(:, :) = 0
  vpp_init(:, :) = 0
  vpp_add(:, :) = 0
  ! Sort ions into velocity bins
  do l=1, Ni_init
    i=floor(vp(l,1))
    j=floor(vp(l,2))
    if ( (i .lt. vxb) .or. (i .gt. vxe) ) then
      cycle
    endif
    if ( (j .lt. vyb) .or. (j .gt. vye) ) then
      cycle
    endif
    vdist_init(i,j) = vdist_init(i,j) + 1
  enddo
  do l= Ni_init+1, Ni_tot
    i=floor(vp(l,1))
    j=floor(vp(l,2))
    if ( (i .lt. vxb) .or. (i .gt. vxe) ) then
      cycle
    endif
    if ( (j .lt. vyb) .or. (j .gt. vye) ) then
      cycle
    endif
  enddo

```

```

        endif
        vdist_add(i,j) = vdist_add(i,j) + 1
    enddo
do l= 1, Ni_init
    m=floor(sqrt((vp(1,1))**2+vp(1,2)**2))
    k=floor(vp(1,3))
    if ( (m .lt. vxb) .or. (i .gt. vxe) ) then
        cycle
    endif
    if ( (k .lt. vyb) .or. (j .gt. vye) ) then
        cycle
    endif
    vpp_init(m,k) = vpp_init(m,k) + 1
enddo
do l= Ni_init+1, Ni_tot
    m=floor(sqrt((vp(1,1))**2+vp(1,2)**2))
    k=floor(vp(1,3))
    if ( (m .lt. vxb) .or. (i .gt. vxe) ) then
        cycle
    endif
    if ( (k .lt. vyb) .or. (j .gt. vye) ) then
        cycle
    endif
    vpp_add(m,k) = vpp_add(m,k) + 1
enddo

! Add up the counts from all of the processing units
call MPI_BARRIER(MPI_COMM_WORLD,ierr)
call MPI_ALLREDUCE(vdist_init(:,:),recvbuf,count, &
    MPI_INTEGER,MPI_SUM,MPI_COMM_WORLD,ierr)
vdist_init(:,:) = reshape(recvbuf,(/(-vxb+vxe+1), &
    (-vyb+vye+1)/))

call MPI_BARRIER(MPI_COMM_WORLD,ierr)
call MPI_ALLREDUCE(vdist_add(:,:),recvbuf,count, &
    MPI_INTEGER,MPI_SUM,MPI_COMM_WORLD,ierr)
vdist_add(:,:) = reshape(recvbuf,(/(-vxb+vxe+1), &
    (-vyb+vye+1)/))

call MPI_BARRIER(MPI_COMM_WORLD,ierr)
call MPI_ALLREDUCE(vpp_init(:,:),recvbuf,count, &
    MPI_INTEGER,MPI_SUM,MPI_COMM_WORLD,ierr)
vpp_init(:,:) = reshape(recvbuf,(/(-vxb+vxe+1), &
    (-vyb+vye+1)/))

```

```

call MPI_BARRIER(MPI_COMM_WORLD,ierr)
call MPI_ALLREDUCE(vpp_add(:,:),recvbuf,count, &
  MPI_INTEGER,MPI_SUM,MPI_COMM_WORLD,ierr)
vpp_add(:,:) = reshape(recvbuf,((-vxb+vxe+1), &
  (-vyb+vye+1)))
deallocate(recvbuf)
end subroutine get_v_dist

```

This subroutine is added to the grid initialization to allow grid stretching. It maintains the grid spacing at λ_i assuming that the density profile is Gaussian.

```

subroutine grid_gaussian()
  rk = nz/2
  rj = ny/2
  ri = nx/2
! Unstretched grids
  do j=1,ny
    qy(j) = j*dy
    dy_grid(j) = dy
  enddo
  do i = 1,nx
    qx(i) = i*dx
    dx_grid(i) = dx
  enddo
! Stretch z
  qz(nz/2) = 0
  do k=rk+1, nz
    ! grid cell is sized by the current Lambda_i
    qz(k) = qz(k-1) + zsf*3e8/1e3*sqrt(8.85e-12*mion/(q*q* &
      (nf_init/1e9+nf_init/1e9*(amp-1.0)* &
      exp(-(qz(k-1)/(grad*delz)**2))))
  enddo
  do k = 1 , rk-1
    ind = rk - k
    qz(ind) = -qz(rk+k)
  enddo
  zplus = qz(nz-1)
  do k=1,nz
    qz(k) = qz(k) + zplus
  enddo
  do k=1, nz-1
    dz_grid(k) = qz(k+1)-qz(k)
  enddo
  dz_grid(nz) = dz_grid(nz-1)

```



```

dz_cell(1) = dz_grid(1)
dz_cell(nz) = dz_grid(nz)
zrat(1) = 0.5
zrat(nz) = 0.5
do k=2, nz-1
    dz_cell(k) = ((qz(k+1) + qz(k))/2.0) - &
        ((qz(k) + qz(k-1))/2.0)
    zplus = (qz(k+1) + qz(k))/2.0
    zminus = (qz(k) + qz(k-1))/2.0
    zrat(k) = (qz(k) - zminus)/(zplus - zminus)
enddo
dx_cell(1) = dx_grid(1)
dx_cell(nx) = dx_grid(nx)
xrat(1) = 0.5
xrat(nx) = 0.5
do i=2, nx-1
    dx_cell(i) = ((qx(i+1) + qx(i))/2.0) - &
        ((qx(i) + qx(i-1))/2.0)
    xplus = (qx(i+1) + qx(i))/2.0
    xminus = (qx(i) + qx(i-1))/2.0
    xrat(i) = (qx(i) - xminus)/(xplus - xminus)
enddo
dy_cell(1) = dy_grid(1)
dy_cell(ny) = dy_grid(ny)
yrat(1) = 0.5
yrat(ny) = 0.5
do j=2, ny-1
    dy_cell(j) = ((qy(j+1) + qy(j))/2.0) - &
        ((qy(j) + qy(j-1))/2.0)
    yplus = (qy(j+1) + qy(j))/2.0
    yminus = (qy(j) + qy(j-1))/2.0
    yrat(j) = (qy(j) - yminus)/(yplus - yminus)
enddo
end subroutine grid_gaussian

```

References

- Achilleos, N. A., C. S. Arridge, P. Guio, N. M. Pilkington, A. Masters, N. Sergis, A. J. Coates, and M. K. Dougherty (2014), Modelling the Compressibility of Saturn's Magnetosphere, *AGU Fall Meeting Abstracts*, SM51E-4296.
- Axford, W. I., and C. O. Hines (1961), A unifying theory of high-latitude geophysical phenomena and geomagnetic storms, *Canadian Journal of Physics*, *39*, 1433, doi:10.1139/p61-172.
- Bagenal, F. (2007), The magnetosphere of Jupiter: Coupling the equator to the poles, *Journal of Atmospheric and Solar-Terrestrial Physics*, *69*, 387–402, doi:10.1016/j.jastp.2006.08.012.
- Bagenal, F., and S. Bartlett (2015), Magnetospheres of the outer planets graphics resources, <http://lasp.colorado.edu/home/mop/resources/graphics/graphics>.
- Bagenal, F., and P. A. Delamere (2011), Flow of mass and energy in the magnetospheres of Jupiter and Saturn, *Journal of Geophysical Research (Space Physics)*, *116*, A05209, doi:10.1029/2010JA016294.
- Birdsall, A., and C. Langdon (1985), *Plasma Physics Via Computer Simulation*, McGraw-Hill Book Company, New York.
- Blanco-Cano, X., C. T. Russell, and R. J. Strangeway (2001), The Io mass-loading disk: Wave dispersion analysis, *Journal of Geophysical Research*, *106*, 26,261–26,276, doi:10.1029/2001JA900090.
- Bonfond, B., D. Grodent, J.-C. Gérard, A. Radioti, J. Saur, and S. Jacobsen (2008), UV Io footprint leading spot: A key feature for understanding the UV Io footprint multiplicity?, *Geophysical Research Letters*, *35*, L05107, doi:10.1029/2007GL032418.

- Boris, J. (1970), *Relativistic plasma simulation-optimization of a hybrid code*, pp. 3–67, Washington, DC.
- Brice, N. M., and G. A. Ioannidis (1970), The Magnetospheres of Jupiter and Earth, *Icarus*, *13*, 173–183, doi:10.1016/0019-1035(70)90048-5.
- Burkholder, B., P. A. Delamere, X. Ma, M. F. Thomsen, R. J. Wilson, and F. Bagenal (2017), Local time asymmetry of Saturn’s magnetosheath flows, *Geophysical Research Letters*, *44*, 5877–5883, doi:10.1002/2017GL073031.
- Caudal, G. (1986), A self-consistent model of Jupiter’s magnetodisc including the effects of centrifugal force and pressure, *Journal of Geophysical Research*, *91*, 4201–4221, doi:10.1029/JA091iA04p04201.
- Chandrasekhar, S. (1961), *Hydrodynamic and hydromagnetic stability*.
- Chané, E., J. Saur, and S. Poedts (2011), The MI-coupling in global simulations of the Jovian and Kronian magnetospheres, *AGU Fall Meeting Abstracts*, SM11A-2013.
- Cheng, C. Z., and J. R. Johnson (1999), A kinetic-fluid model, *Journal of Geophysical Research*, *104*, 413–428, doi:10.1029/1998JA900065.
- Chust, T., A. Roux, W. S. Kurth, D. A. Gurnett, M. G. Kivelson, and K. K. Khurana (2005), Are Io’s Alfvén wings filamented? Galileo observations, *Planetary and Space Science*, *53*, 395–412, doi:10.1016/j.pss.2004.09.021.
- Connerney, J. E. P., T. Satoh, and J. T. Clarke (2001), Io’s Flux Tube Footprint, in *Planetary Radio Emissions V*, edited by H. O. Rucker, M. L. Kaiser, and Y. Leblanc, p. 49.
- Cowee, M. M., D. Winske, and S. P. Gary (2009), Two-dimensional hybrid simulations of superdiffusion at the magnetopause driven by Kelvin-Helmholtz instability, *Journal of Geophysical Research (Space Physics)*, *114*, A10209, doi:10.1029/2009JA014222.

- Cowley, S. W. H., and E. J. Bunce (2001), Origin of the main auroral oval in Jupiter's coupled magnetosphere-ionosphere system, *Planetary Space Science*, *49*, 1067–1088, doi:10.1016/S0032-0633(00)00167-7.
- Cowley, S. W. H., S. V. Badman, E. J. Bunce, J. T. Clarke, J.-C. Gérard, D. Grodent, C. M. Jackman, S. E. Milan, and T. K. Yeoman (2005), Reconnection in a rotation-dominated magnetosphere and its relation to Saturn's auroral dynamics, *Journal of Geophysical Research (Space Physics)*, *110*, A02201, doi:10.1029/2004JA010796.
- Crary, F. J., and F. Bagenal (2000), Ion cyclotron waves, pickup ions, and Io's neutral exosphere, *Journal of Geophysical Research*, *105*, 25,379–27,066, doi:10.1029/2000JA000055.
- Damiano, P., A. Wright, R. Sydora, and J. Samson (2007), Energy dissipation via electron energization in standing shear Alfvén waves, *Phys. Plasmas*, *14*, 062904.
- Damiano, P. A., J. R. Johnson, and C. C. Chaston (2015), Ion temperature effects on magnetotail Alfvén wave propagation and electron energization, *Journal of Geophysical Research (Space Physics)*, *120*, 5623–5632, doi:10.1002/2015JA021074.
- Delamere, P. (1998), Analysis of optical observations and three-dimensional hybrid code simulation of the crres plasma injection experiments in space, Ph.D. thesis, University of Alaska Fairbanks.
- Delamere, P. A., and F. Bagenal (2010), Solar wind interaction with Jupiter's magnetosphere, *Journal of Geophysical Research (Space Physics)*, *115*, A10201, doi:10.1029/2010JA015347.
- Delamere, P. A., and F. Bagenal (2013), Magnetotail structure of the giant magnetospheres: Implications of the viscous interaction with the solar wind, *Journal of Geophysical Research (Space Physics)*, *118*, 7045–7053, doi:10.1002/2013JA019179.

- Delamere, P. A., D. W. Swift, and H. C. Stenbaek-Nielsen (1999), A three-dimensional hybrid code simulation of the December 1984 solar wind AMPTE release, *Geophysical Research Letters*, *26*, 2837–2840, doi:10.1029/1999GL900602.
- Delamere, P. A., F. Bagenal, R. Ergun, and Y.-J. Su (2003), Momentum transfer between the Io plasma wake and Jupiter’s ionosphere, *Journal of Geophysical Research (Space Physics)*, *108*, 1241, doi:10.1029/2002JA009530.
- Delamere, P. A., A. Otto, X. Ma, F. Bagenal, and R. J. Wilson (2015), Magnetic flux circulation in the rotationally driven giant magnetospheres, *Journal of Geophysical Research (Space Physics)*, *120*, 4229–4245, doi:10.1002/2015JA021036.
- Dols, V., P. A. Delamere, and F. Bagenal (2008), A multispecies chemistry model of Io’s local interaction with the Plasma Torus, *Journal of Geophysical Research (Space Physics)*, *113*, A09208, doi:10.1029/2007JA012805.
- Dungey, J. W. (1961), Interplanetary Magnetic Field and the Auroral Zones, *Physical Review Letters*, *6*, 47–48, doi:10.1103/PhysRevLett.6.47.
- Fleshman, B. L., P. A. Delamere, F. Bagenal, and T. Cassidy (2013), A 1-D model of physical chemistry in Saturn’s inner magnetosphere, *Journal of Geophysical Research (Planets)*, *118*, 1567–1581, doi:10.1002/jgre.20106.
- Frank, L. A., and W. R. Paterson (2000), Observations of plasmas in the Io torus with the Galileo spacecraft, *Journal of Geophysical Research*, *105*, 16,017–16,034, doi:10.1029/1999JA000250.
- G  rard, J.-C., A. Saglam, D. Grodent, and J. T. Clarke (2006), Morphology of the ultraviolet Io footprint emission and its control by Io’s location, *Journal of Geophysical Research (Space Physics)*, *111*, A04202, doi:10.1029/2005JA011327.

- Grodent, D., A. Radioti, B. Bonfond, and J.-C. Gérard (2010), On the origin of Saturn's outer auroral emission, *Journal of Geophysical Research (Space Physics)*, *115*, A08219, doi:10.1029/2009JA014901.
- Hasegawa, A. (1976), Particle acceleration by MHD surface wave and formation of aurora, *Journal of Geophysical Research*, *81*, 5083–5090, doi:10.1029/JA081i028p05083.
- Hess, S., F. Mottez, and P. Zarka (2007), Jovian S burst generation by Alfvén waves, *Journal of Geophysical Research (Space Physics)*, *112*, A11212, doi:10.1029/2006JA012191.
- Hess, S. L. G., P. Delamere, V. Dols, B. Bonfond, and D. Swift (2010), Power transmission and particle acceleration along the Io flux tube, *Journal of Geophysical Research (Space Physics)*, *115*, A06205, doi:10.1029/2009JA014928.
- Hill, T. W., M. F. Thomsen, M. G. Henderson, R. L. Tokar, A. J. Coates, H. J. McAndrews, G. R. Lewis, D. G. Mitchell, C. M. Jackman, C. T. Russell, M. K. Dougherty, F. J. Crary, and D. T. Young (2008), Plasmoids in Saturn's magnetotail, *Journal of Geophysical Research (Space Physics)*, *113*, A01214, doi:10.1029/2007JA012626.
- Huba, J. D. (1996), The Kelvin-Helmholtz instability: Finite Larmor radius magnetohydrodynamics, *Geophysical Research Letters*, *23*, 2907–2910, doi:10.1029/96GL02767.
- Huba, J. D., and D. Winske (1998), Rayleigh-Taylor instability: Comparison of hybrid and nonideal magnetohydrodynamic simulations, *Physics of Plasmas*, *5*, 2305–2316, doi:10.1063/1.872904.
- Huddleston, D. E., R. J. Strangeway, J. Warnecke, C. T. Russell, M. G. Kivelson, and F. Bagenal (1997), Ion cyclotron waves in the Io torus during the Galileo encounter: Warm plasma dispersion analysis, *Geophysical Research Letters*, *24*, 2143, doi:10.1029/97GL01203.

- Jackman, C. M., J. A. Slavin, and S. W. H. Cowley (2011), Cassini observations of plasmoid structure and dynamics: Implications for the role of magnetic reconnection in magnetospheric circulation at Saturn, *Journal of Geophysical Research (Space Physics)*, *116*, A10212, doi:10.1029/2011JA016682.
- Jacobsen, S., J. Saur, F. M. Neubauer, B. Bonfond, J.-C. Gérard, and D. Grodent (2010), Location and spatial shape of electron beams in Io’s wake, *Journal of Geophysical Research (Space Physics)*, *115*, A04205, doi:10.1029/2009JA014753.
- Johnson, J. R., and C. Z. Cheng (2001), Stochastic ion heating at the magnetopause due to kinetic Alfvén waves, *Geophysical Review Letters*, *28*, 4421–4424, doi:10.1029/2001GL013509.
- Kaminker, V., P. A. Delamere, C. S. Ng, T. Dennis, A. Otto, and X. Ma (2017), Local time dependence of turbulent magnetic fields in Saturn’s magnetodisc, *Journal of Geophysical Research (Space Physics)*, *122*, 3972–3984, doi:10.1002/2016JA023834.
- Khurana, K. K., and M. G. Kivelson (1989), Ultralow frequency MHD waves in Jupiter’s middle magnetosphere, *Journal of Geophysical Research*, *94*, 5241–5254, doi:10.1029/JA094iA05p05241.
- Kidder, A., R. M. Winglee, and E. M. Harnett (2009), Regulation of the centrifugal interchange cycle in Saturn’s inner magnetosphere, *Journal of Geophysical Research (Space Physics)*, *114*, A02205, doi:10.1029/2008JA013100.
- Kivelson, M. G., and D. J. Southwood (2005), Dynamical consequences of two modes of centrifugal instability in Jupiter’s outer magnetosphere, *Journal of Geophysical Research (Space Physics)*, *110*, A12209, doi:10.1029/2005JA011176.
- Krall, N. A., and A. W. Trivelpiece (1973), *Principles of plasma physics*.

- Lee, L. C., R. K. Albano, and J. R. Kan (1981), Kelvin-Helmholtz instability in the magnetopause-boundary layer region, *Journal of Geophysical Research*, *86*, 54–58, doi:10.1029/JA086iA01p00054.
- Lin, Y., J. R. Johnson, and X. Wang (2010), Hybrid Simulation of Mode Conversion at the Magnetopause, *Journal of Geophysical Research*, doi:10.1029/2009JA014524.
- Liu, X., and T. W. Hill (2012), Effects of finite plasma pressure on centrifugally driven convection in Saturn’s inner magnetosphere, *Journal of Geophysical Research (Space Physics)*, *117*, A07216, doi:10.1029/2012JA017827.
- Lysak, R. L., and W. Lotko (1996), On the kinetic dispersion relation for shear Alfvén waves, *Journal of Geophysical Research*, *101*, 5085–5094, doi:10.1029/95JA03712.
- Ma, X. (2018), Plasma entropy in Saturn’s magnetosphere, in preparation.
- Ma, X., P. A. Delamere, and A. Otto (2016), Plasma transport driven by the Rayleigh-Taylor instability, *Journal of Geophysical Research (Space Physics)*, *121*, 5260–5271, doi:10.1002/2015JA022122.
- Mauk, B. H., D. K. Haggerty, C. Paranicas, G. Clark, P. Kollmann, A. M. Rymer, S. J. Bolton, S. M. Levin, A. Adriani, F. Allegrini, F. Bagenal, B. Bonfond, J. E. P. Connerney, G. R. Gladstone, W. S. Kurth, D. J. McComas, and P. Valek (2017), Discrete and broadband electron acceleration in Jupiter’s powerful aurora, *Nature*, *549*, 66–69, doi:10.1038/nature23648.
- Mozer, F. S., and A. Hull (2010), Scaling the energy conversion rate from magnetic field reconnection to different bodies, *Physics of Plasmas*, *17*(10), 102,906–102,906, doi:10.1063/1.3504224.
- Neubauer, F. M. (1980), Nonlinear standing Alfvén wave current system at Io - Theory, *Journal of Geophysical Research*, *85*, 1171–1178, doi:10.1029/JA085iA03p01171.

- Neupane, B. R., P. A. Delamere, and X. Ma (2017), Plasma transport and magnetic flux circulation in Saturn’s magnetosphere, *AGU Fall Meeting Abstracts*, SM51E-2537.
- Nykyri, K., and A. Otto (2001), Plasma transport at the magnetospheric boundary due to reconnection in Kelvin-Helmholtz vortices, *Geophysical Research Letters*, *28*, 3565–3568, doi:10.1029/2001GL013239.
- Nykyri, K., and A. Otto (2004), Influence of the Hall term on KH instability and reconnection inside KH vortices, *Annales Geophysicae*, *22*, 935–949, doi:10.5194/angeo-22-935-2004.
- Otto, A., and D. H. Fairfield (2000), Kelvin-Helmholtz instability at the magnetotail boundary: MHD simulation and comparison with Geotail observations, *Journal of Geophysical Research*, *105*, 21, doi:10.1029/1999JA000312.
- Potter, D. (1977), *Computational Physics*, John Wiley and Sons Ltd.
- Queinnec, J., and P. Zarka (1998), Io-controlled decameter arcs and Io-Jupiter interaction, *Journal of Geophysical Research*, *103*, 26,649–26,666, doi:10.1029/98JA02435.
- Roberts, K. V., and J. B. Taylor (1962), Magnetohydrodynamic Equations for Finite Larmor Radius, *Physical Review Letters*, *8*, 197–198, doi:10.1103/PhysRevLett.8.197.
- Russell, C. T., D. e. Huddleston, K. K. Khurana, and M. G. Kivelson (1999), Structure of the Jovian magnetodisk current sheet: initial Galileo observations, *Planetary and Space Science*, *47*, 1101–1109, doi:10.1016/S0032-0633(99)00026-4.
- Saur, J., F. M. Neubauer, J. E. P. Connerney, P. Zarka, and M. G. Kivelson (2004), *Plasma interaction of Io with its plasma torus*, pp. 537–560.
- Stallard, T., S. Miller, H. Melin, M. Lystrup, S. W. H. Cowley, E. J. Bunce, N. Achilleos, and M. Dougherty (2008), Jovian-like aurorae on Saturn, *Nature*, *453*, 1083–1085, doi:10.1038/nature07077.

- Stix, T. H. (1992), *Waves in Plasmas*, American Institute of Physics.
- Su, Y.-J., R. E. Ergun, F. Bagenal, and P. A. Delamere (2003), Io-related Jovian auroral arcs: Modeling parallel electric fields, *Journal of Geophysical Research (Space Physics)*, *108*, 1094, doi:10.1029/2002JA009247.
- Su, Y.-J., S. T. Jones, R. E. Ergun, F. Bagenal, S. E. Parker, P. A. Delamere, and R. L. Lysak (2006), Io-Jupiter interaction: Alfvén wave propagation and ionospheric Alfvén resonator, *Journal of Geophysical Research (Space Physics)*, *111*, A06211, doi:10.1029/2005JA011252.
- Swanson, D. (1989), *Plasma Waves*, Academic Press, Inc.
- Swift, D. W. (1996), Use of a Hybrid Code for Global-Scale Plasma Simulation, *Journal of Computational Physics*, *126*, 109–121, doi:10.1006/jcph.1996.0124.
- Thomas, N., F. Bagenal, T. W. Hill, and J. K. Wilson (2004), *The Io neutral clouds and plasma torus*, pp. 561–591.
- Thomsen, M. F., D. B. Reisenfeld, D. M. Delapp, R. L. Tokar, D. T. Young, F. J. Crary, E. C. Sittler, M. A. McGraw, and J. D. Williams (2010), Survey of ion plasma parameters in Saturn’s magnetosphere, *Journal of Geophysical Research (Space Physics)*, *115*, A10220, doi:10.1029/2010JA015267.
- Vasyliunas, V. M. (1983), *Plasma distribution and flow*, pp. 395–453.
- Vogt, M. F., M. G. Kivelson, K. K. Khurana, S. P. Joy, and R. J. Walker (2010), Reconnection and flows in the Jovian magnetotail as inferred from magnetometer observations, *Journal of Geophysical Research (Space Physics)*, *115*, A06219, doi:10.1029/2009JA015098.
- von Papen, M., and J. Saur (2016), Longitudinal and local time asymmetries of magnetospheric turbulence in Saturn’s plasma sheet, *Journal of Geophysical Research (Space Physics)*, *121*, 4119–4134, doi:10.1002/2016JA022427.

- von Papen, M., J. Saur, and O. Alexandrova (2014), Turbulent magnetic field fluctuations in Saturn’s magnetosphere, *Journal of Geophysical Research (Space Physics)*, *119*, 2797–2818, doi:10.1002/2013JA019542.
- Winglee, R. M., A. Kidder, E. Harnett, N. Ifland, C. Paty, and D. Snowden (2013), Generation of periodic signatures at Saturn through Titan’s interaction with the centrifugal interchange instability, *Journal of Geophysical Research (Space Physics)*, *118*, 4253–4269, doi:10.1002/jgra.50397.
- Wright, A. N. (1987), The interaction of Io’s Alfvén waves with the Jovian magnetosphere, *Journal of Geophysical Research*, *92*, 9963–9970, doi:10.1029/JA092iA09p09963.
- Wyatt, M. (2017), Xflow: A natural cfd code, <https://www.linkedin.com/pulse/xflow-natural-cfd-code-mark-wyatt>.
- Yee, K. (1966), Numerical solution of initial boundary value problems involving Maxwell’s equations in isotropic media, *IEEE Transactions on Antennas and Propagation*, *14*, 302–307, doi:10.1109/TAP.1966.1138693.